

AD-A067 306

SANTA BARBARA RESEARCH CENTER GOLETA CALIF

F/G 17/5

DEVELOPMENT OF LARGE AREA PV HgCdTe DETECTORS FOR 2.06 AND 3.85--ETC(U)

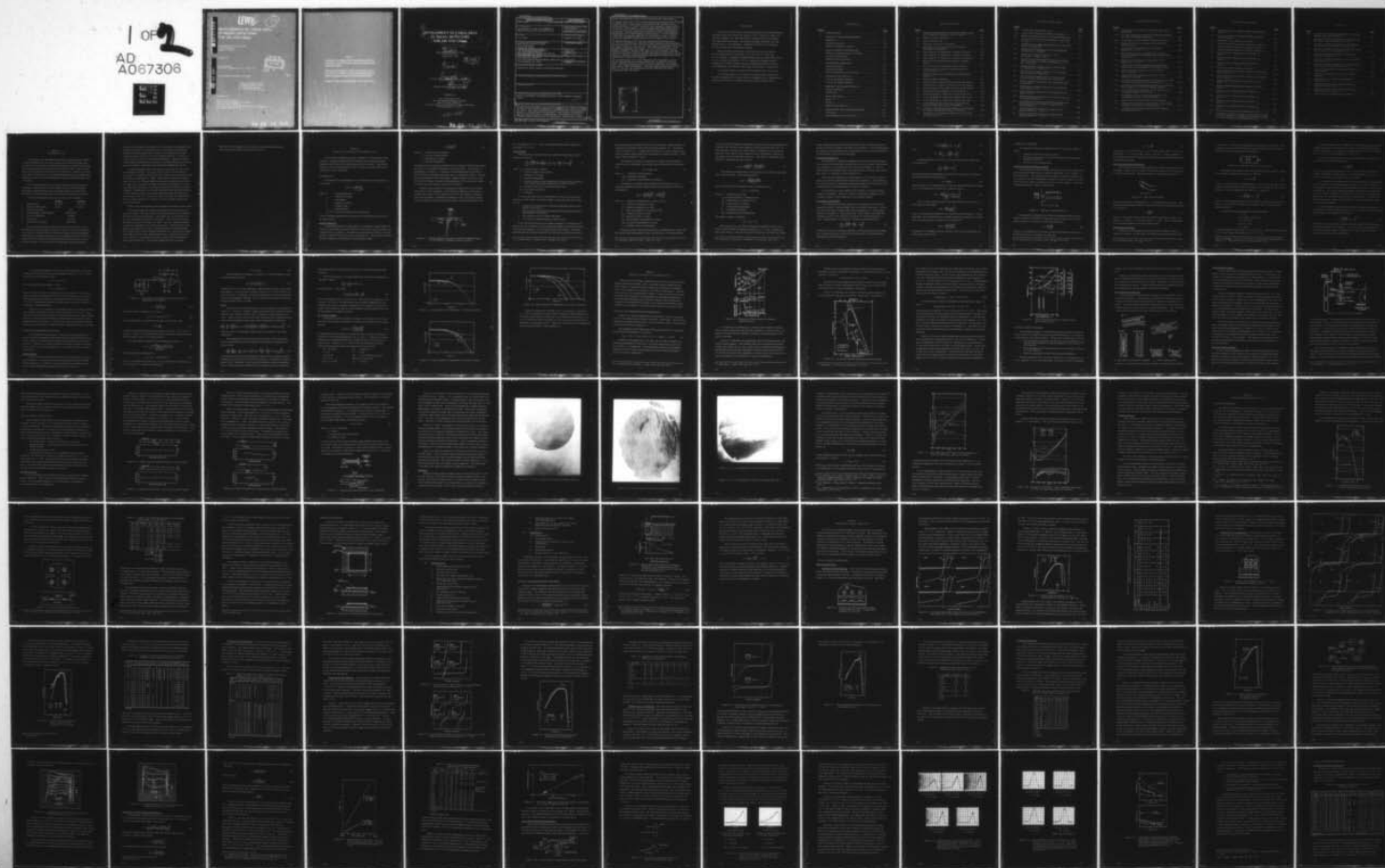
MAY 78 P R BRATT

DAAB07-76-C-0803

NL

UNCLASSIFIED

1 of 2
AD
A067306



DA067306

LEVEL

11
B.S.

DEVELOPMENT OF LARGE AREA
PV HgCdTe DETECTORS
FOR 2.06 AND 3.85 μ m

Santa Barbara Research Center
75 Coromar Drive
Goleta, CA 93017

31 May 1978

Interim Report
For Period 5 January 1976 to 15 June 1977

DDC
RECEIVED
APR 12 1979
C

Contract Number DAAB07-76-C-0803

APPROVED FOR PUBLIC RELEASE
DISTRIBUTION UNLIMITED

Prepared for

U.S. Army Electronics
Research and Development Command
Laser Division, DELNV-L
U.S. Army Night Vision and Electro-Optics Laboratory
Fort Monmouth, NJ 07703

DDC FILE COPY

79 04 12 012

NOTICES

THE FINDINGS IN THIS REPORT ARE NOT TO BE CONSTRUED AS AN OFFICIAL DEPARTMENT OF THE ARMY POSITION, UNLESS SO DESIGNATED BY OTHER AUTHORIZED DOCUMENTS.

THE CITATION OF TRADE NAMES AND NAMES OF MANUFACTURERS IN THIS REPORT IS NOT TO BE CONSTRUED AS OFFICIAL GOVERNMENT ENDORSEMENT OR APPROVAL OF COMMERCIAL PRODUCTS OR SERVICES REFERENCED HEREIN.

DESTROY THIS REPORT WHEN NO LONGER NEEDED. DO NOT RETURN TO SENDER.

⑥
**DEVELOPMENT OF LARGE AREA
PV HgCdTe DETECTORS
FOR 2.06 AND 3.85 ~~um~~ *micrometers*.**

⑩

P. R. Bratt

Santa Barbara Research Center
75 Coromar Drive
Goleta, CA 93017

⑫ 164 p.

⑪

31 May 1978

⑨

Interim Report.

For Period 5 Jan ~~1976~~ 1976 to 15 June 1977

⑮

Contract Number DAAB07-76-C-0803

Prepared for

U. S. Army Electronics
Research and Development Command
Laser Division, DELNV-L
U. S. Army Night Vision and Electro-Optics Laboratory
Fort Monmouth, NJ 07703

315 650

79 04 12 012

Unclassified

SECURITY CLASSIFICATION OF THIS PAGE (When Data Entered)

REPORT DOCUMENTATION PAGE		READ INSTRUCTIONS BEFORE COMPLETING FORM
1. REPORT NUMBER	2. GOVT ACCESSION NO.	3. RECIPIENT'S CATALOG NUMBER
4. TITLE (and Subtitle) Development of Large Area Photovoltaic HgCdTe Detectors for 2.06 and 3.85 μm		5. TYPE OF REPORT & PERIOD COVERED Interim Report 5 Jan 1976 - 15 Jun 1977
		6. PERFORMING ORG. REPORT NUMBER
7. AUTHOR(s) P. R. Bratt		8. CONTRACT OR GRANT NUMBER(s) DAAB07-76-C-0803
9. PERFORMING ORGANIZATION NAME AND ADDRESS Santa Barbara Research Center 75 Coromar Drive Goleta, CA 93017		10. PROGRAM ELEMENT, PROJECT, TASK AREA & WORK UNIT NUMBERS
11. CONTROLLING OFFICE NAME AND ADDRESS U. S. Army Electronics Research and Development Command Electronics Systems Procurement Branch Fort Monmouth, NJ 07703		12. REPORT DATE 31 May 1978
		13. NUMBER OF PAGES 159
14. MONITORING AGENCY NAME & ADDRESS (if different from Controlling Office) Laser Division, DELNV-L U. S. Army Night Vision and Electro Optics Lab Fort Monmouth, NJ 07703		15. SECURITY CLASS. (of this report) Unclassified
15a. DECLASSIFICATION/DOWNGRADING SCHEDULE		
16. DISTRIBUTION STATEMENT (of this Report) Approved for public release, distribution unlimited.		
17. DISTRIBUTION STATEMENT (of the abstract entered in Block 20, if different from Report)		
18. SUPPLEMENTARY NOTES		
19. KEY WORDS (Continue on reverse side if necessary and identify by block number) HgCdTe, photodiodes, photovoltaic detectors, laser detectors, quadrant arrays.		
20. ABSTRACT (Continue on reverse side if necessary and identify by block number) The purpose of this program was to develop large area PV HgCdTe detectors for laser receiver systems operating at 2.06 μm (Ho:YLF laser) and 3.85 μm (DF laser). The work accomplished included: Evaluation of three different methods of crystal growth, the preparation of low acceptor concentration p- type base material by means of gold diffusion, development of a junction formation method utilizing boron ion implantation, and evaluation of those		

DD FORM 1 JAN 73 1473

EDITION OF 1 NOV 65 IS OBSOLETE

Unclassified

SECURITY CLASSIFICATION OF THIS PAGE (When Data Entered)

Unclassified

SECURITY CLASSIFICATION OF THIS PAGE(When Data Entered)

detector characteristics which control operation in the 1 MHz region.

PV HgCdTe detectors for 3.85 μm were successfully fabricated up to $5 \times 5 \text{ mm}^2$ in sensitive area. Net acceptor concentrations in the vicinity of the p-n junction of about $3 \times 10^{14} \text{ cm}^{-3}$ gave zero bias capacitance values of about 150 pf/mm². These detectors achieved background limited detectivities of $3 \times 10^{11} \text{ cm Hz}^{1/2}/\text{w}$ at 77°K in the low frequency range with an optimized preamplifier. Quantum efficiencies measured 70 to 90%. High frequency detectivities for $5 \times 5 \text{ mm}^2$ detectors were typically $6 \times 10^{10} \text{ cm Hz}^{1/2}/\text{w}$ at 1 MHz with a preamplifier optimized for this frequency range. Typical detector-preamplifier response times were in the range 100 to 200 nsec.

PV HgCdTe detectors for 2.06 μm were successfully fabricated up to $2 \times 2 \text{ mm}^2$ in sensitive area. Because of higher acceptor concentrations in the base material ($\approx 2 \times 10^{16} \text{ cm}^{-3}$) zero bias junction capacitance values were also higher, being about 500 pf/mm². These detectors achieved 77°K low frequency detectivities in the range 2 to $8 \times 10^{11} \text{ cm Hz}^{1/2}/\text{w}$ and were not background limited. Because of the higher junction capacitance, the high frequency performance of these detectors was inferior to that of the 3.85 μm detectors. Means to reduce the junction capacitance are known and could be implemented on some future program.

Two quadrant arrays of $5 \times 5 \text{ mm}^2$ detectors were assembled in vacuum dewars equipped with Joule-Thomson expansion cryostats for cooling to 80°K. These were delivered to the U.S. Army along with a four-channel high speed (10 MHz) preamplifier. Additional single-element detectors for both 3.85 μm and 2.06 μm operation were also delivered along with a demountable metal LN₂ dewar.

ACCESSION for	
NTIS	White Section <input checked="" type="checkbox"/>
DOC	B-G Section <input type="checkbox"/>
UNANNOUNCED	<input type="checkbox"/>
JUSTIFICATION	
BY	
DISTRIBUTION/AVAIL	3
Dist.	IAL
A	

Unclassified

SECURITY CLASSIFICATION OF THIS PAGE(When Data Entered)

PREFACE

The work documented in this report was performed at the Santa Barbara Research Center over the period 5 January 1976 to 15 June 1977 under Contract No. DAAB07-76-C-0803 with the U. S. Army Electronics Command, Fort Monmouth, New Jersey. The program manager during the first eight months was Dr. J. M. Steininger. During the remainder of the program, Dr. P. R. Bratt served as program manager.

Major technical contributions to the detector work were made by A. H. B. Vanderwyck, W. H. Konkel, R. A. Cole, Dr. K. J. Riley and Dr. P. R. Bratt. Preamplifier design and fabrication was under the direction of J. S. Lee and S. P. Ryan III. Dr. C. L. Anderson at Hughes Research Laboratories provided valuable technical consultation and direction of the ion-implantation work which was performed at the Research Laboratories.

The program technical monitor at Fort Monmouth was C. E. Loscoe.

This interim report covers work done on optimization of large detectors for wavelengths of 2.06 and 3.85 μm . Subsequent work is being directed toward detectors for 10.6 μm and will be described in a future report.

CONTENTS

<u>Section</u>		<u>Page</u>
1	INTRODUCTION	1-1
2	THEORY OF DETECTOR OPERATION	2-1
	Detectivity	2-1
	Frequency Response	2-8
	Detector-Preamplifier Analysis	2-12
3	HgCdTe MATERIAL PREPARATION	3-1
	Physical and Thermodynamic Properties	3-1
	Crystal Growth Methods	3-5
	HgCdTe Material Evaluation	3-9
4	PHOTODIODE FABRICATION	4-1
	Junction Formation	4-1
	Fabrication Method	4-6
	Optical Considerations of the Design	4-8
5	DETECTOR TEST RESULTS	5-1
	3.85- μ m PV HgCdTe Detectors	5-1
	2.06- μ m PV HgCdTe Detectors	5-34
6	ASSEMBLY OF QUADRANT ARRAYS	6-1
	Detector Assembly	6-1
	Preamplifier	6-3
7	FINAL TEST DATA	7-1
	QD No. 1	7-1
	QD No. 2	7-11
	Single Element Detectors	7-22
8	CONCLUSIONS AND RECOMMENDATIONS	8-1
	Conclusions	8-1
	Recommendations for Future Work	8-4

ILLUSTRATIONS

<u>Figure</u>		<u>Page</u>
2-1	Diagram Showing Absorption of Radiation (Shaded Region) in a PV Detector in Relation to the p-n Junction	2-2
2-2	Diffusion Limited Photodiode	2-8
2-3	Drift Type Photodiode	2-9
2-4	Equivalent Circuit for a Photodiode	2-10
2-5	Equivalent Circuit Diagram for the PV Detector-Preamplifier Combination	2-13
2-6	High Frequency D^* Dependence on Junction Resistance	2-16
2-7	High Frequency D^* Dependence on Series Resistance	2-16
2-8	High Frequency D^* Dependence on Junction Capacitance	2-17
3-1	Physical and Thermodynamic Properties of HgCdTe Alloys	3-2
3-2	Hg-Cd-Te Pressure-Temperature Phase Diagram	3-3
3-3	Thermodynamic Properties of HgCdTe Alloys for 2.06 and 3.85 μm	3-5
3-4	HgCdTe Crystal Growth Techniques in Sealed Quartz Ampoule	3-6
3-5	Pressure Reflux Technique	3-8
3-6	Density Profile of Ingot RC4 Grown by the SSR Method	3-10
3-7	Density Profile of Ingot 2-132 Grown by the ZM Method	3-10
3-8	Density Profiles of Two Ingots Grown by the PR Method	3-11
3-9	Berg-Barrett Back Reflection X-ray Topography	3-12
3-10	X-ray Topograph of a Wafer from HgCdTe Ingot RC4	3-14
3-11	X-ray Topograph of a Wafer from HgCdTe Ingot 2-132	3-15
3-12	X-ray Topograph of a Wafer from HgCdTe Ingot WK-9	3-16
3-13	Hall Coefficient versus Reciprocal Temperature for Three Au-Doped $\text{Hg}_{0.69}\text{Cd}_{0.31}\text{Te}$ Samples	3-18
3-14	Resistivity and Mobility versus Reciprocal Temperature for Three Au-Doped $\text{Hg}_{0.69}\text{Cd}_{0.31}\text{Te}$ Samples	3-19
4-1	Calculated Ion Concentration Profile for an Al^+ Implant into $\text{Hg}_{0.7}\text{Cd}_{0.3}\text{Te}$	4-1

ILLUSTRATIONS (Cont)

Figure		Page
4-2	Van der Pauw Hall Sample Layout.....	4-3
4-3	Large Area PV HgCdTe Photodiode Construction.....	4-6
4-4	Optical Absorption Model for Ion Implanted Photodiodes....	4-9
5-1	Layout of Four Mesa-Type Photodiodes on Half-Wafer No. WK4	5-1
5-2	Current versus Voltage Characteristics for Four Photo- diodes from Wafer WK4	5-2
5-3	Relative Spectral Response at Three Temperatures for Detector No. WK4-B20	5-3
5-4	Layout of Six-Element Array of $1 \times 1 \text{ mm}^2$ Photodiodes on Wafer 2-124-80	5-5
5-5	Current versus Voltage Characteristics for Six Photo- diodes from Wafer 2-124-80 at Temperatures of 77° , 145° , and 192°K	5-6
5-6	Relative Spectral Response at Three Temperatures for Detector No. 2-124-80-B2	5-7
5-7	Current versus Voltage Curves for a Four-Element Mesa Array from Crystal WK9.....	5-11
5-8	Current versus Voltage Curves for Four Nominal $2 \times 2 \text{ mm}^2$ Planar Photodiodes from Crystal WK9.....	5-11
5-9	Relative Spectral Response for Two Photodiodes from Crystal WK9	5-12
5-10	Current versus Voltage Curves for Two Photodiodes from Wafer 2-132-10	5-14
5-11	Relative Spectral Response for Two Photodiodes from Wafer 2-132-10	5-15
5-12	Relative Spectral Response for Two Typical Large Area PV HgCdTe Detectors.....	5-19
5-13	Block Diagram of Fine Spot Contouring Apparatus Used to Measure Sensitivity Profiles of Large Area PV HgCdTe Detectors	5-20
5-14	Fine Spot Sensitivity Profiles for Large Area PV HgCdTe Detector No. 2-132-21	5-21
5-15	Fine Spot Sensitivity Profiles for Large Area PV HgCdTe Detector No. 2-132-19	5-22

ILLUSTRATIONS (Cont)

<u>Figure</u>		<u>Page</u>
5-16	Representative $1/C^2$ versus V Curves for $Hg_{1-x}Cd_xTe$ Photodiodes	5-24
5-17	Zero Bias Capacitance versus Base Doping Concentration for 3.85- μm PV HgCdTe Detectors	5-26
5-18	Circuit Used for τ Measurements with Reverse Bias	5-26
5-19	Illustration of Method of Analysis of Detector Pulse Response Data	5-27
5-20	Pulse Response Measurements of PV HgCdTe Detector No. 2-132-15	5-28
5-21	Pulse Response Curves on Detector No. 2-132-15 Showing the Decrease in Response Time with Increasing Reverse Bias	5-30
5-22	Pulse Response Curves for a Nominal $2 \times 2 \text{ mm}^2$ Detector, No. 2-132-10	5-31
5-23	Comparison of Measured Detector Response Times (Data Points) with Calculated RC Times (Solid Lines).	5-32
5-24	Relative Spectral Response at 77°K for Detector No. 2-138-3B-2	5-38
5-25	Relative Spectral Response at 192°K and 77°K for Detector No. RC4-2B	5-39
5-26	Current versus Voltage Curves for Two Nominal $2 \times 2 \text{ mm}^2$ PV HgCdTe Detectors for 2.06- μm Operation	5-40
5-27	Measured and Calculated Response Times versus Reverse Bias Voltage for a 2.06- μm PV HgCdTe Detector	5-41
5-28	Fine Spot Sensitivity Profiles for a $2 \times 2 \text{ mm}^2$ 2.06- μm PV HgCdTe Detector (No. RC4-2B).	5-42
6-1	Photograph of 3.85- μm Large Area Quadrant Array Assembled from Four $5 \times 5 \text{ mm}^2$ Elements	6-1
6-2	Large Area PV HgCdTe Detector Dewar Assembly	6-2
6-3	Exploded View Showing the Various Parts of the Detector Assembly for the 3.85- μm Quadrant Array	6-4
6-4	Assembled View of Large Area PV HgCdTe Detector Assembly for 3.85 μm	6-4

ILLUSTRATIONS (Cont)

<u>Figure</u>		<u>Page</u>
6-5	Block Diagram of PV HgCdTe Detector-Preamplifier Circuit.....	6-5
6-6	View of Large Area PV HgCdTe Detector Assembly and Preamplifier	6-5
7-1	Detectivity versus Frequency for QD No. 1	7-4
7-2	Responsivity and Noise versus Frequency for QD No. 1 ...	7-5
7-3	Relative Spectral Response for Channel 3 of QD No. 1	7-6
7-4	Relative Spectral Response for Channel 4 of QD No. 1	7-7
7-5	Current versus Voltage Curves for Channel 1 of QD No. 1	7-8
7-6	Current versus Voltage Curves for Channel 3 of QD No. 1	7-9
7-7	Current versus Voltage Curves for Channel 4 of QD No. 1	7-10
7-8	Detectivity versus Frequency for QD No. 2	7-12
7-9	Responsivity and Noise versus Frequency for Channels 1 and 2 of QD No. 2	7-13
7-10	Responsivity and Noise versus Frequency for Channels 3 and 4 of QD No. 2	7-14
7-11	Relative Spectral Response for Channels 1 and 2 of QD No. 2	7-15
7-12	Relative Spectral Response for Channels 3 and 4 of QD No. 2	7-16
7-13	Current versus Voltage Curves for Channel 1 of QD No. 2	7-17
7-14	Current versus Voltage Curves for Channel 2 of QD No. 2	7-18
7-15	Current versus Voltage Curves for Channel 3 of QD No. 2	7-19
7-16	Current versus Voltage Curves for Channel 4 of QD No. 2	7-20
7-17	Spot Scan Profiles for the Completed Array QD No. 2	7-21
8-1	Illustration of Method of Cutting an HgCdTe Ingot into Slabs to Provide Material for Simultaneous Fabrication of Three $5 \times 5 \text{ mm}^2$ or Eight $2 \times 2 \text{ mm}^2$ Quadrant Arrays	8-9

TABLES

<u>Table</u>		<u>Page</u>
4-1	Comparison of Calculated and Measured Ion Implant Doping in $\text{Hg}_{0.7}\text{Cd}_{0.3}\text{Te}$ Wafers	4-4
5-1	Summary of Detector Properties of a Four-Element PV HgCdTe Array Made from Wafer WK4	5-4
5-2	Summary of Detector Properties of a Six-Element PV HgCdTe Array Made from Wafer 2-124-80	5-8
5-3	Summary of Detector Properties of Photodiode Arrays Made on Wafers 5-20-108 and 5-20-131	5-9
5-4	Summary of Detector Properties of Photodiodes Made from Crystal WK9	5-13
5-5	Summary of Detector Properties of Two Photodiodes from Wafer 2-132-10	5-16
5-6	Summary of Detector Properties for Fourteen Large Area Photodiodes Made from Ingot 2-132	5-17
5-7	Data on 18 $\text{Hg}_{1-x}\text{Cd}_x\text{Te}$ Photodiodes Analyzed by C-V Measurements	5-25
5-8	Summary of Properties of 2.06- μm PV HgCdTe Detectors	5-34
6-1	Specifications for PV HgCdTe Preamplifier, Model A231-4	6-5
7-1	Measured Test Data on PV HgCdTe Large Area Quadrant Array No. QD-1	7-2
7-2	Measured Test Data on PV HgCdTe Large Area Quadrant Array No. QD-2	7-11
7-3	Serial Numbers of Single Element Detectors	7-22

Section 1 INTRODUCTION

This program was undertaken to help satisfy a need for laser tracking systems operating in the "eye safe" regions of the infrared (IR) spectrum. The specific objective was to develop the technology for producing large area, fast response photovoltaic (PV) HgCdTe detectors for laser receivers operating at 2.06 μm (Ho:YLF laser) and 3.85 μm (DF laser). HgCdTe is an ideal semiconductor material to use for these photodiodes because its bandgap may be adjusted to fit the desired wavelength by variation of the HgTe/CdTe ratio in the alloy.

The technical approach was to optimize HgCdTe material preparation technology so that large size, uniform single crystals could be obtained. Additionally, photodiode fabrication technology needed to be optimized to provide the low junction capacitance necessary for high speed performance.

The initial design goals chosen for this work were as follows:

	<u>Array A</u>	<u>Array B</u>
1. Spectral peak	$\approx 2.06 \mu\text{m}$	$\approx 3.85 \mu\text{m}$
2. Operating temperature	$\geq 245^\circ\text{K}$	$\geq 195^\circ\text{K}$
3. Quantum efficiency		60%
4. Dark (leakage) current density		$< 500 \mu\text{a}/\text{cm}^2$
5. Electrical bandwidth		20 MHz
6. Active area		$5 \times 5 \text{ mm}^2$
7. Uniformity of response		Within 10%

The operating temperatures selected were based on the desire to utilize thermoelectric (TE) means for detector cooling. As the work progressed, it soon became evident that detector sensitivity would be seriously degraded at these higher operating temperatures. This degradation was due to the high saturation current caused by thermal generation of minority carriers in the p-n junction region. For laser detectors operating as optical heterodyne

receivers, this problem can sometimes be overcome by increasing the local oscillator (LO) power so that minority carrier generation by LO photons dominates the thermal generation. However, the intended use for these large area detectors did not involve heterodyning operation. The only recourse then was to reduce the operating temperature. Operation at liquid nitrogen (LN_2) temperature was, therefore, selected because this can easily be achieved using a conventional Joule-Thomson expanding gas cryostat.

Another design goal which was found to be unrealistic was the electrical bandwidth of 20 MHz. The fastest response times observed with the large area ($5 \times 5 \text{ mm}^2$) detectors was 70 nsec under reverse biased operation. This implies a bandwidth of 2.3 MHz. Some detectors exhibited response times in the 100- to 200-nsec range which implies a bandwidth on the order of 1 MHz. Since these detectors were made using the optimized, low junction capacitance procedure, it was quite clear that the 20-MHz goal was unattainable. Subsequently, the electrical bandwidth requirement was reduced to that of detecting a laser pulse having a Gaussian shape and width (half-power points) of 100 nsec. This can be done with an electrical bandwidth in the 2- to 5-MHz range and is, therefore, a more reasonable requirement for these detectors.

All the other design goals for this program were found to be achievable.

The program plan was to begin with the HgCdTe material growth optimization studies. The initial material produced would be used to optimize the detector fabrication techniques. At the same time, this would provide the necessary characterization of the material. The first detectors made had sensitive areas in the range 1 to 4 mm^2 . Later on, when good HgCdTe crystals were identified, work on the large area ($5 \times 5 \text{ mm}^2$) detectors was begun. In parallel with this work, design and fabrication of the preamplifiers and the detector dewar package was carried out. This report is organized along these same lines starting with Section 3. However, previous to this, in Section 2, is presented a discussion of the theory of operation of large area PV detectors. This lays the foundations for the technical

approach that was adopted and is the basis for discussion of the detector performance measurements presented in Section 5.

Section 2

THEORY OF DETECTOR OPERATION

In this section the physical theory of operation of a PV detector is described. The design features that are important for obtaining good high-frequency performance from large area detectors are noted. A parametric analysis of $D^*(\lambda_p)$ versus frequency which includes the preamplifier noise contribution is also presented.

DETECTIVITY

The detectivity at wavelength λ for a PV detector can be expressed by the equation

$$D^*(\lambda) = \frac{\eta e \lambda \sqrt{A}}{h c i_n / (\Delta f)^{\frac{1}{2}}} \quad (1)$$

where η = quantum efficiency
 e = electronic charge
 λ = wavelength
 h = Planck's constant
 c = speed of light
 A = sensitive area
 $i_n / (\Delta f)^{\frac{1}{2}}$ = rms noise current per unit bandwidth

The two important quantities in this equation are the quantum efficiency and the noise current.

Quantum Efficiency

The quantum efficiency of the detector is controlled by optical reflection loss at the front surface and by the efficiency with which minority carriers are collected at the p-n junction. By applying an antireflection coating to the front surface, reflection loss can be limited to less than 5%. The minority collection efficiency depends on the minority carrier diffusion length

$$L = \left(\frac{\mu \tau k T}{e} \right)^{\frac{1}{2}} \quad (2)$$

where μ = minority carrier mobility

τ = minority carrier lifetime

k = Boltzmann's constant

T = absolute temperature

Only those minority carriers generated within a diffusion length of the junction are likely to be collected and measured as a photosignal. The situation is diagrammed in Figure 2-1. Radiation incident through the front surface of the PV detector is absorbed and decays away in exponential fashion. Minority electrons generated on the p side within a diffusion length L_n of the p-n junction will be collected. Minority holes generated on the n side within a diffusion length L_p of the junction will also be collected.

Location of the junction at an appropriate depth below the top surface of the device is also important. Since 90% of the radiation is absorbed in a distance $2/\alpha$, and α is on the order of $5 \times 10^3 \text{ cm}^{-1}$ for HgCdTe, the region over which absorption is essentially complete is $4 \mu\text{m}$. By proper location of the p-n junction within this absorption region, collection efficiencies can

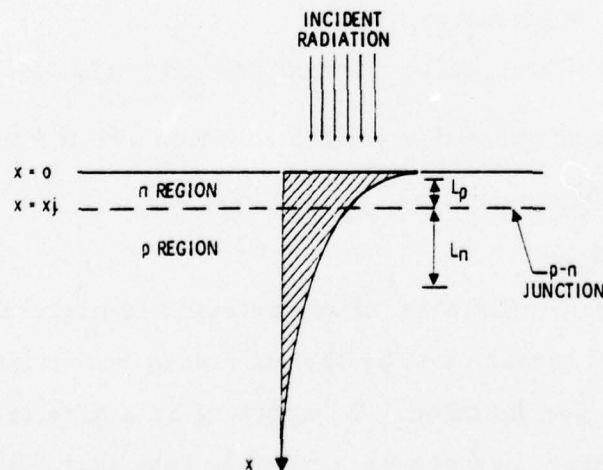


Figure 2-1. Diagram Showing Absorption of Radiation (Shaded Region) in a PV Detector in Relation to the p-n Junction

be in the range 0.5 to 0.9. Thus overall quantum efficiencies should be in the range of 0.5 to 0.8.

Noise Current

The total rms noise current per unit bandwidth originating in the PV detector is given by¹

$$\frac{i_n}{(\Delta f)^{\frac{1}{2}}} = \left\{ \frac{2eI_s}{\beta} \left[\exp\left(\frac{eV}{\beta kT}\right) + 1 \right] + 2eI_p + \frac{4kT}{R_s} + \frac{1}{f} \text{ term} \right\}^{\frac{1}{2}} \quad (3)$$

where I_s = diode saturation current

V = applied voltage across junction

k = Boltzmann's constant

T = absolute temperature

β = a factor between 1 and 2 depending on the generation-recombination current in the space charge layer of the p-n junction

I_p = dc photocurrent due to background photon flux

R_s = diode shunt resistance

f = frequency

It is seen that there are four contributions to the total noise current. These are, in the order in which they appear on the right hand side of equation (3):

1. The shot noise current from thermally generated carriers which diffuse to the junction
2. The shot noise current from background photogenerated carriers which diffuse to the junction
3. The Johnson noise of the shunt resistance
4. $1/f$ noise due to surface states or other sources

One of the main objectives of the detector engineer is to design the PV detector so as to minimize its noise current and thereby maximize detectivity. From the noise equation, it can be seen how this may be done. Thermally generated shot noise can be minimized by reducing the saturation current I_s .

¹G. R. Pruet and R. L. Petritz, Proc. IRE 47, 1524 (1959).

Background photon generated shot noise is minimized by operating under reduced background photon flux conditions where possible (i. e., cold filters, cold FOV shields, etc.). Surface shunt resistance is made as large as possible by suitable surface passivation treatments and these also may, in some cases, serve to reduce 1/f noise.

The saturation current is controlled by a number of semiconductor properties and is composed of two terms, here expressed as current densities,

$$J_s = J_{diff} + J_{gr} \quad (4)$$

where J_s = saturation current density

J_{diff} = diffusion component

J_{gr} = generation-recombination component.

The diffusion component of the saturation current density is due to thermally generated minority carriers which cross the junction and can be expressed by²

$$J_{diff} = e \left\{ p \left(\frac{\mu_p k T}{\tau_p e} \right)^{\frac{1}{2}} + n \left(\frac{\mu_n k T}{\tau_n e} \right)^{\frac{1}{2}} \right\} \quad (5)$$

where n = electron concentration on p-side $\approx n_i^2 / N_A$

μ_n = mobility of electron on p-side

τ_n = lifetime of electron on p-side

p = hole concentration on n-side $\approx n_i^2 / N_D$

μ_p = mobility of hole on n-side

τ_p = lifetime of hole on n-side

N_A = net acceptor concentration on p-side

N_D = net donor concentration on n-side

n_i = intrinsic carrier concentration

By heavily doping one side of the junction, for example the n-side, then the minority hole concentration on this side (given by $p = n_i^2 / N_D$) becomes

²W. Shockley, Bell Syst. Tech. J. 28, 435 (1949).

very small and the diffusion current from this side can be made negligible with respect to the minority electron diffusion current from the other side. We then have what is called a one-sided junction, designated an n^+-p junction. Since this is the type of junction that was used in the present investigation, the analysis will be restricted to this case. The diffusion component of the saturation current density then becomes

$$J_{\text{diff}} \approx e n \left(\frac{\mu_p k T}{\tau_n e} \right)^{\frac{1}{2}} = e \frac{n_i^2}{N_A} \left(\frac{\mu_n k T}{\tau_n e} \right)^{\frac{1}{2}} \quad (6)$$

The generation-recombination current density has a thermal component which, near zero bias, can be represented by³

$$J_{\text{gr}, t} = \frac{e n_i W}{\sqrt{\tau_{no} \tau_{po}}} \left(\frac{2kT}{e\phi_b} \right), \quad (7)$$

and a background photon (generation only) component given by

$$J_b = (1 - r) e \alpha W Q_B \quad (8)$$

where W = depletion layer width

τ_{no} = electron lifetime in depletion layer

τ_{po} = hole lifetime in depletion layer

ϕ_b = junction built-in voltage

r = front surface reflectance

α = absorption coefficient

Q_B = background photon flux density.

The total g-r current is therefore

$$J_{\text{gr}} = J_{\text{gr}, t} + J_b \quad (9)$$

Both J_{diff} and $J_{\text{gr}, t}$ are highly temperature dependent because the intrinsic carrier density n_i depends exponentially on T . Thus, J_{diff} goes as $\exp(-E_g/kT)$ and $J_{\text{gr}, t}$ goes as $\exp(-E_g/2kT)$ where E_g is the band gap energy.

³C. T. Sah, R. N. Noyce and W. Shockley, Proc. IRE 45, 1228 (1957).

Higher operating temperatures produce higher values of these current components and result in higher noise levels in the detector. At low temperatures, the saturation current density will be determined by J_b , provided that surface or bulk leakage current does not dominate.

Reverse Bias Operation

If the detector is operated at temperatures where thermally generated shot noise makes the dominant contribution to the noise current, then according to equation (3), the application of a reverse bias voltage $-V \gg \beta kT/e$ should make the exponential term much less than unity and this could conceivably result in a decrease in noise current by $\sqrt{2}$.

However, past experience has shown that the $1/f$ noise due to surface states may increase rapidly under reverse bias conditions. This depends on the surface passivation treatment used and the density and distribution of fast interface states at the semiconductor-insulator interface.

The possibility of noise reduction with reverse bias should be experimentally investigated. However, it cannot be counted on happening so the theoretical analysis of this section will not include this effect.

Resistance-Area Product

The resistance-area ($R_o A$) product of a PV detector is an important parameter because it sets the upper limit on achievable detectivity. To see how this comes about, consider again the noise equation (3). Photovoltaic detectors are usually operated at zero bias. This condition eliminates the exponential factor in the first term in equation (3) and minimizes the $1/f$ noise. Neglecting the $1/f$ noise term, the equation then simplifies to

$$\frac{i_n}{(\Delta f)^{\frac{1}{2}}} = \left\{ \frac{4eI_s}{\beta} + \frac{4kT}{R_s} + 2eI_p \right\}^{\frac{1}{2}} \quad (10)$$

The first two terms involving the saturation current and the shunt resistance can be related to the zero bias dynamic resistance R_o of the photodiode by differentiating the diode equation

$$I = I_s \left[\exp\left(\frac{eV}{\beta k T}\right) - 1 \right] - I_p + \frac{V}{R_s} \quad (11)$$

to get

$$R_o = \left. \frac{dV}{dI} \right|_{V=0} = \left[\frac{eI_s}{\beta k T} + \frac{1}{R_s} \right]^{-1} \quad (12)$$

Combining equation (12) with (10) we can write the noise current per unit bandwidth as

$$\frac{i_n}{(\Delta f)^{\frac{1}{2}}} = \left[\frac{4kT}{R_o} + 2eI_p \right]^{\frac{1}{2}} \quad (13)$$

The background photon generated current from the base region is related to background photon flux density Q_B by

$$I_p = \eta e Q_B A \quad (14)$$

When equation (14) is substituted into (13) and the result substituted into equation (1), an expression for detectivity is obtained which is

$$D^*(\lambda) = \frac{\eta e \lambda}{hc} \left[\frac{A}{\frac{4kT}{R_o} + 2\eta e^2 Q_B A} \right]^{\frac{1}{2}} \quad (15)$$

Thus, at high background photon flux levels where the second term in the denominator dominates,

$$D^*(\lambda) = \frac{\eta \lambda}{hc} \left[\frac{1}{2\eta Q_B} \right]^{\frac{1}{2}} \quad (16)$$

which is the well-known expression for a BLIP photovoltaic detector. On the other hand, at low backgrounds or at higher operating temperatures, the first term in the denominator of equation (15) dominates and

$$D^*(\lambda) = \frac{\eta e \lambda}{hc} \left[\frac{R_o A}{4kT} \right]^{\frac{1}{2}} \quad (17)$$

Therefore, $D^*(\lambda)$ depends on the $R_o A$ product to the $\frac{1}{2}$ power and higher $R_o A$ values permit higher $D^*(\lambda)$.

FREQUENCY RESPONSE

The frequency response of a photodiode will in general be limited by either:

1. Diffusion of carriers to the p-n junction
2. Drift across the junction or junction transit time (important for graded p-n junctions)
3. The diode junction capacitance

Diffusion Limited Frequency Response

Photogenerated minority carriers are generated near the surface of the device and must diffuse to the p-n junction before they can be "counted" in the photocurrent. This diffusion process requires a certain amount of time. The situation is shown schematically in Figure 2-2 for the case of an n-on-p junction with the junction located quite close to the top surface. In this case the diffusing minority carriers are electrons.

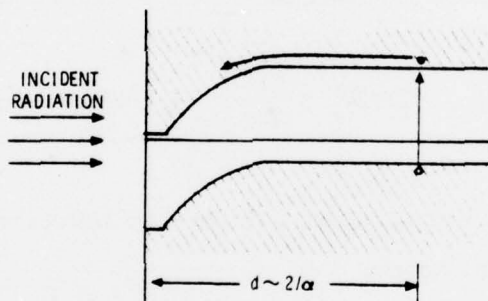


Figure 2-2. Diffusion Limited Photodiode

The frequency response for the diffusion limited photodiode has been treated by Sawyer and Rediker.⁴ They found that the upper limit to the frequency response (0.707 point) is given approximately by

$$f_c = \frac{2.4 D_n}{2\pi d^2} \quad (18)$$

where d is the distance from the point of origin of the minority carriers to the junction; and D_n is the diffusion coefficient,

⁴D. E. Sawyer and R. H. Rediker, Proc. IRE 46, 1122 (1958).

$$D_n = \mu_n \frac{kT}{e} \quad (19)$$

Assuming $d = 2/\alpha = 4 \times 10^{-4}$ cm, $\mu_n = 2 \times 10^4$ cm²/volt sec and $T = 100^\circ\text{K}$, we find that $D_n = 1.73 \times 10^2$ cm²/sec, and $f_c = 413$ MHz. It seems clear from this calculation that the frequency response of the large area photodiodes will not be diffusion limited.

Drift Limited Frequency Response

This situation occurs when photogenerated carriers are produced within the depletion region of a p-n junction and are then swept out by the large electric field existing there. This type of junction is illustrated in Figure 2-3.

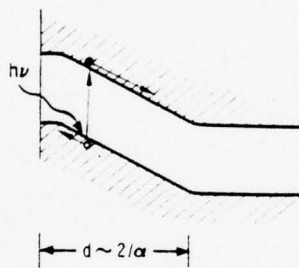


Figure 2-3. Drift Type Photodiode

Such a structure may be realized in p-i-n, or graded junction devices. This case has been analyzed by Gärtner,⁵ who shows that the upper frequency limit (0.707 point) is

$$f_c = \frac{2.8v}{2\pi W} \quad (20)$$

where v is the carrier velocity and W the width of the depletion region. Assuming $W = 2/\alpha$ and $v = 10^7$ cm/sec, then $f_c = 11$ GHz. Thus, the photodiode for the present application will not be drift limited.

Capacitance Limitations

In addition to the frequency response limitation imposed by drift or diffusion of carriers, we must also be concerned with the capacitance of the

⁵W. W. Gärtner, Phys. Rev. 116, 84 (1959).

p-n junction. As shown in the equivalent circuit diagram of Figure 2-4, this capacitance acts as a shunt in parallel with the photodiode and will cause attenuation of the photocurrent at high frequencies.

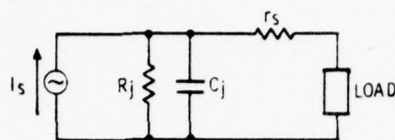


Figure 2-4. Equivalent Circuit for a Photodiode

The capacitance depends on the junction depletion layer width W , dielectric constant κ_s , and junction area A_j , as follows:

$$C_j = \kappa_s \epsilon_0 \frac{A_j}{W} \quad (21)$$

where ϵ_0 is the permittivity of empty space. To get a rough idea of the magnitude of capacitance that would be encountered, we consider the step junction situation in which the depletion layer width, W , is given by⁶

$$W = \left[\frac{2 \kappa_s \epsilon_0}{eN} (\phi_b + V) \right]^{\frac{1}{2}} \quad (22)$$

where e is the electronic charge, N is the impurity concentration in the base region, ϕ_b is the built-in potential of the junction, and V is the externally applied potential.

Using the following representative values for HgCdTe

$$\kappa_s = 16$$

$$\epsilon_0 = 8.85 \times 10^{-14} \text{ fd/cm}$$

$$N = 10^{15} / \text{cm}^3$$

$$\phi_b = 0.15 \text{ volt}$$

$$V = 0 \text{ volt}$$

we obtain a depletion layer width $W = 0.52 \times 10^{-4} \text{ cm}$. The junction capacitance for a $5 \times 5 \text{ mm}^2$ diode would then be $C_j = 6.8 \times 10^{-9} \text{ fd}$.

⁶See, for example, A. S. Grove, "Physics and Technology of Semiconductor Devices," J. Wiley and Sons, New York, Chapter 6 (1967).

According to equation (22), application of an external reverse bias will increase the depletion width of the p-n junction and therefore decrease the junction capacitance. For example, a reverse bias of 0.5 volt will increase W to 1.1×10^{-4} cm and decrease C_j to 3.2×10^{-9} fd.

For this capacitance limited case, the high-frequency response limit (0.707 point) is given approximately by

$$f_c = \frac{1}{2\pi C_j R_{||}} \quad (23)$$

where C_j is the junction capacitance and $R_{||}$ is the parallel combination resistance of detector and load resistor. If we assume that $R_j \gg R_L$, $C_j = 3.2 \times 10^{-9}$ fd, and $R_L = 50$ ohms, then $f_c = 1.0$ MHz.

It is clear from this example that the junction capacitance presents the major limitation to the high-frequency response of large area photodiodes. The frequency response can be improved somewhat by using a current-mode preamplifier. This type of amplifier presents an effective input impedance less than 50 ohms; therefore, the frequency response limit calculated from equation (23) will be greater than the value obtained above. A detailed discussion of detector operation when coupled to a current-mode preamplifier will be given subsequently.

It is theoretically possible to further reduce junction capacitance by constructing a linearly graded junction or a p-i-n structure. For the linearly graded junction, the depletion layer width is

$$W = \left[\frac{12\kappa_s \epsilon_0}{e\gamma} (\phi_b + V) \right]^{1/3} \quad (24)$$

where all symbols have been previously defined, except γ which represents the impurity gradient at the junction. It is clear from this equation that, if γ can be kept small enough, the depletion layer width will be increased, thereby decreasing junction capacitance.

To increase the frequency response to much greater than 1 MHz, the capacitance of the junction must be considerably less than 10^{-9} fd. The depletion layer width required is then

$$W > 3.1 \times 10^{-4} \text{ cm}$$

This would require the gradient, γ , to be

$$\gamma \sim 1 \times 10^{18} \text{ cm}^{-4}$$

Such a gradient could only be achieved in very pure material. It implies a change in doping concentration of $10^{14}/\text{cm}^3/\mu\text{m}$ of distance into the crystal. The base doping of the crystal would therefore have to be much less than $10^{14}/\text{cm}^3$. Although such material has been seen, it occurs only rarely in fortuitously compensated ingots.

Likewise, a p-i-n structure would require some way to obtain material with impurity concentration in the i region much less than $10^{14}/\text{cm}^3$. Since there seemed to be small likelihood of obtaining such material in large enough quantity to make the large area detectors required for this program, these approaches were not pursued. A step junction approach was selected and the base doping was minimized to keep the junction capacitance as low as possible.

DETECTOR-PREAMPLIFIER ANALYSIS

For high frequency applications, a current-mode preamplifier is desired to reduce the capacitive loading due to the high junction capacitance of the PV detector. Preamplifier noise may be the limiting noise at high frequencies. Therefore, an analysis of detector frequency response and sensitivity must also include the preamplifier. In this section, such an analysis is performed.

Signal Response

Figure 2-5 shows the equivalent circuit for the PV detector-preamplifier combination. Consider first the signal current produced by the ideal current generator i_s . If detector series resistance is not negligible, the signal current reaching the preamplifier input will be given by

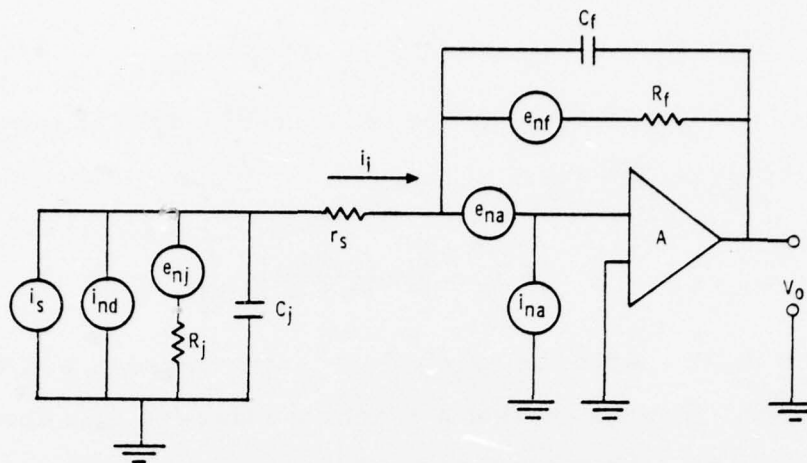


Figure 2-5. Equivalent Circuit Diagram for the PV Detector-Preamplifier Combination

$$i_i = i_s \left(\frac{Z_j}{Z_j + r_s} \right) \quad (25)$$

where the junction impedance Z_j is given by

$$Z_j = R_j (1 + \omega^2 R_j^2 C_j^2)^{-\frac{1}{2}} \quad (26)$$

At high frequencies, the capacitive reactance may dominate, thus

$$Z_j \approx \frac{1}{\omega C_j} \quad (27)$$

Consider a case where the junction capacitance is 4000 pf. Then, at a frequency of 1 MHz, $Z_j = 40$ ohms and the series resistance must be much less than this value to avoid loss of signal current.

The output signal voltage from the preamplifier is given by

$$V_{os} = \frac{-AZ_f i_s}{A + 1 + \left(\frac{Z_f}{Z_j + r_s} \right)} \left(\frac{Z_j}{Z_j + r_s} \right) \quad (28)$$

where the feedback impedance Z_f is

$$Z_f = R_f (1 + \omega^2 R_f^2 C_f^2)^{-\frac{1}{2}} \quad (29)$$

and A is the amplifier open loop gain. For low frequencies, where $Z_f \approx Z_j$, $r_s \ll Z_j$ and $A \gg 1$, equation (28) reduces to

$$V_{os} \approx -R_f i_s \quad (30)$$

The high frequency response is reduced to 1/2 the low frequency value at some frequency given by

$$f_h \approx \left[2\pi \left(\frac{R_f}{1+A} \right) C_j \right]^{-1} \quad (31)$$

The factor $R_f/(1+A)$ is the "equivalent" input impedance of the current-mode preamplifier. It turns out that a practical value for A is about 50 and for R_f about 1000 ohms. Therefore, the junction capacitance C_j must be minimized to allow high frequency response. If $C_j = 4000$ pf, and the above values for A and R_f are used, then $f_h = 2$ MHz.

Noise

The major noise sources are shown in the equivalent circuit diagram of Figure 2-5. They are: amplifier voltage and current noise, feedback resistor Johnson noise, detector Johnson noise, and detector photon generated shot noise. These combine to give a total noise voltage per unit of frequency bandwidth at the preamplifier output which can be expressed by the equation

$$\frac{V_{on}}{\sqrt{\Delta f}} = \left[\left(1 + \frac{Z_f}{Z_j} \right)^2 \left(e_{na}^2 + i_{na}^2 Z_f^2 \right) + \left(\frac{4kT_f}{R_f} \right) Z_f^2 + \left(\frac{4kT_j}{R_j} \right) Z_f^2 + 2e^2 \eta Q_B A_d Z_f^2 \right]^{\frac{1}{2}} \quad (32)$$

The four terms in this equation represent the noise sources in the order listed above.

The preamplifier current noise can be neglected at high frequencies. With this approximation and some algebraic manipulations of equation (32), one can obtain

$$\frac{V_{on}}{\sqrt{\Delta f}} = \left\{ \left| \left(\frac{1}{R_f} + \frac{1}{R_j} \right) + j\omega(C_f + C_j) \right|^2 e_{na}^2 + \frac{4kT_f}{R_f} + \frac{4kT_j}{R_j} + 2e^2 \eta Q_B A_d \right\}^{\frac{1}{2}} Z_f \quad (33)$$

This equation shows that the preamplifier voltage noise is boosted at higher frequencies while the other noise terms remain flat. The degree of high frequency boost is dependent on the magnitude of detector junction capacitance. Thus a minimized junction capacitance is necessary not only for extending

the signal response to high frequency but also for minimizing noise at high frequency.

The corner frequency at which preamplifier noise boost commences is obtained by setting

$$\left(\frac{1}{R_f} + \frac{1}{R_j} \right) = 2\pi f(C_f + C_j)$$

and solving for f . This yields

$$f = \frac{1}{2\pi(C_f + C_j)} \left(\frac{1}{R_f} + \frac{1}{R_j} \right) \quad (34)$$

For a case where $R_f = R_j = 1000$ ohms, $C_j = 4000$ pf and C_f is negligible, one obtains $f = 8 \times 10^4$ Hz. The noise boost cannot continue indefinitely but will ultimately be rolled off at higher frequencies due to frequency limitations inherent in the transistors used or to high frequency rolloff purposely built into the preamplifier for stability reasons.

D* versus Frequency

Using equation (28) to calculate responsivity and equation (33) to calculate noise, D^* may then be obtained as a function of frequency from the usual equation

$$D^*(\lambda_p, f) = \frac{R_v(\lambda_p, f) \sqrt{A_d}}{V_{on(f)} \sqrt{\Delta f}} \quad (35)$$

A parametric study was made to ascertain the effect on $D^*(\lambda_p, f)$ produced by variations in the detector parameters, R_j , C_j , and r_s . Values for D^* versus frequency were calculated holding two parameters fixed, and allowing the third to vary. Figures 2-6, 2-7, and 2-8 show the results of this study.

Other fixed parameters used in the calculations were as follows.

$R_f = 1000$ ohms	$A_d = 0.284$ cm ²
$A = 50$	$\eta = 0.84$
$T_f = 295^\circ\text{K}$	$Q_B = 2 \times 10^{15}$ photons/sec/cm ²
$T_d = 77^\circ\text{K}$	$I_s(\lambda_p) = 2.5$ amps/watt
$e_{na} = 0.7$ nv/Hz ^{$\frac{1}{2}$}	$\lambda_p = 3.85$ μm

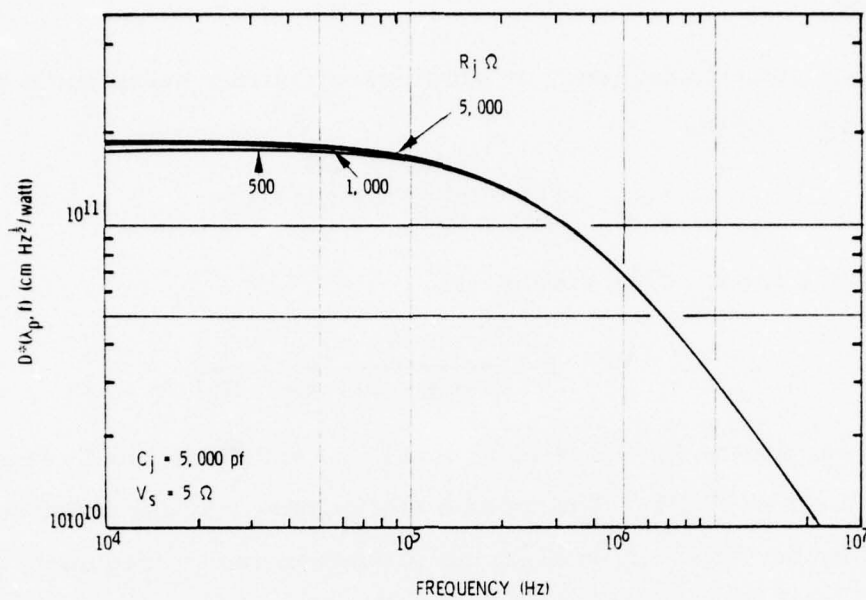


Figure 2-6. High Frequency D^* Dependence on Junction Resistance

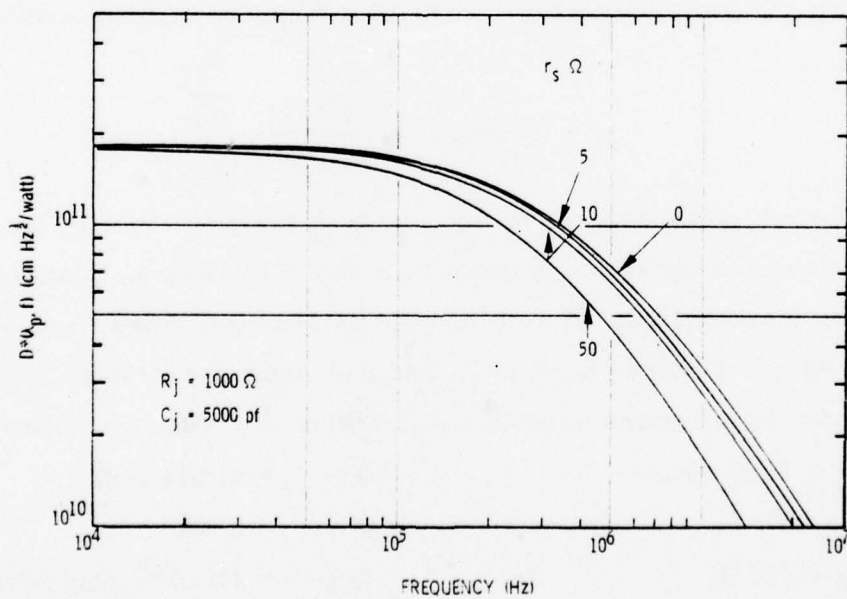


Figure 2-7. High Frequency D^* Dependence on Series Resistance

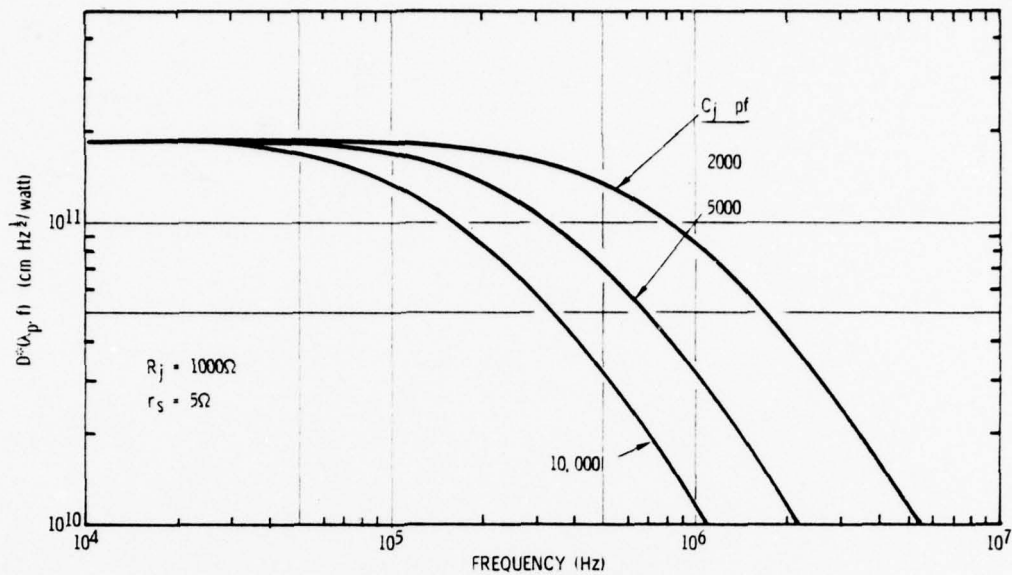


Figure 2-8. High Frequency D^* Dependence on Junction Capacitance

Figure 2-6 shows that little effect on D^* is produced by variations in R_j . This is as expected since the junction impedance at high frequencies is controlled by the capacitive reactance, not by the junction resistance. Figure 2-7 shows that series resistance up to 10 ohms does not cause serious degradation of high frequency D^* . Figure 2-8 shows that junction capacitance has the strongest effect on high frequency D^* .

Section 3

HgCdTe MATERIAL PREPARATION

Because of its versatility, HgCdTe is one of the most popular infrared detector materials presently in use. Of all the variable bandgap ternary alloy systems, it alone provides the widest span of detection wavelengths, from 0.9 μm (pure CdTe) to beyond 30 μm (16% CdTe/84% HgTe). However, it is also one of the most difficult to prepare in single-crystal form because of the high vapor pressure of Hg encountered at the melting temperature. In this section are presented some of the basic physical and thermodynamic properties of the HgCdTe alloy system, the crystal growth methods adopted by SBRC for this program, and typical results of the crystal growing study.

PHYSICAL AND THERMODYNAMIC PROPERTIES

HgCdTe is a variable bandgap alloy semiconductor made by combining CdTe (a wide-bandgap semiconductor) and HgTe (a semimetal). HgCdTe photo-detectors have been made over the 1- to 30- μm spectral region by varying the composition of the alloy (Figure 3-1).

The dependence of the energy gap of $\text{Hg}_{1-x}\text{Cd}_x\text{Te}$ alloys on composition x and absolute temperature T is given by⁷

$$E_g = -0.25 + 1.59x + 5.233 \times 10^{-4} (1 - 2.08x) T + 0.327x^3 \quad (36)$$

Solution of this equation for 2.06- and 3.85- μm peak wavelengths and operating temperatures of 245°K and 195°K gives approximate values for x of 0.48 and 0.31, respectively. This calculation assumes energy bandgap values of 0.55 and 0.29 eV corresponding to detector cutoff wavelengths of 2.27 and 4.24 μm , respectively.

⁷J. L. Schmit and E. L. Stelzer, J. Appl. Phys. 40, 4865 (1969).

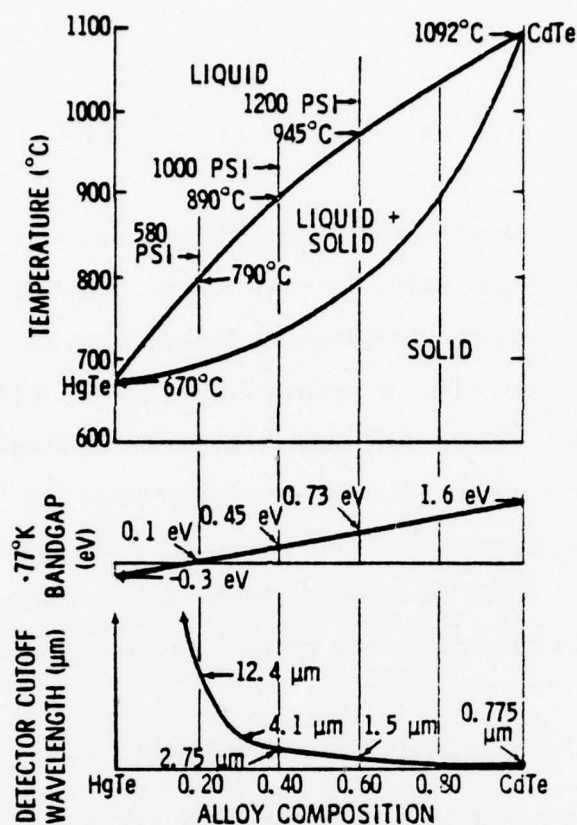


Figure 3-1. Physical and Thermodynamic Properties of HgCdTe Alloys

To understand the difficulties of crystal growth of HgCdTe material, and the specific techniques that have been developed to overcome them, it is useful to consider the thermodynamic properties and phase diagram of the Hg-Cd-Te system.

Figure 3-1 illustrates the pseudobinary HgTe-CdTe temperature-composition phase diagram. This diagram shows the wide separation between liquidus and solidus curves, which results from the significant difference in the melting points of the end compounds, and their large heats of fusion.⁸ This leads to the well-known segregation of the alloy upon freezing from the melt, and therefore to nonuniformity of material composition.

⁸J. Steininger, J. Appl. Phys. 41, 2713 (1970).

Another less-known segregation effect results from the difference in the density of alloys of different compositions. The alloy density ρ for a composition x is given by

$$\rho \text{ (gm/cm}^3\text{)} = 8.076 - 2.226x \quad (37)$$

The CdTe-rich solid material which freezes out first is much lighter than the HgTe-rich melt, and therefore tends to float to the surface of the melt giving rise to vertical segregation in the ingot.

Figure 3-2 illustrates the pressure-temperature phase diagram for various sections of the Hg-Cd-Te system. Shown here is recent data⁹ on

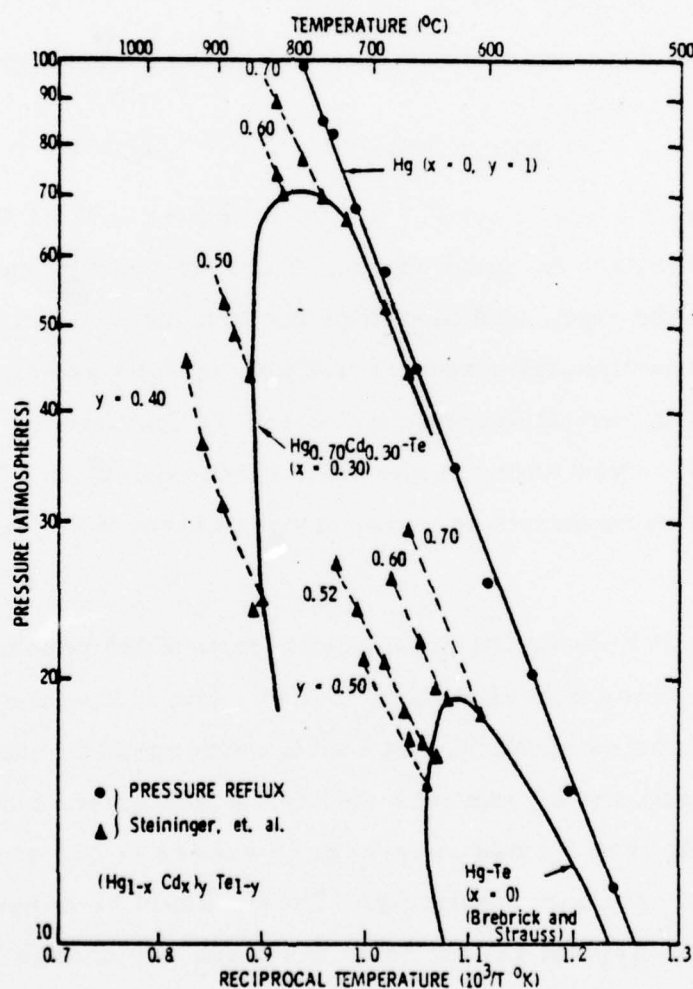


Figure 3-2. Hg-Cd-Te Pressure-Temperature Phase Diagram

⁹J. Steininger, J. Electronic Materials 5, 299 (1976).

the variation of Hg vapor pressure over liquid melts of pure Hg, binary Hg-Te and ternary $\text{Hg}_{0.70}\text{Cd}_{0.30}\text{Te}$. The alloy compositions are represented by the formula $(\text{Hg}_{1-x}\text{Cd}_x)_y\text{Te}_{1-y}$, where x is the usual pseudobinary alloy composition, and y represents the deviations from pseudobinary stoichiometry ($y = 0.50$); i. e., excess metal ($y > 0.50$) or excess Te ($y < 0.50$). The significant feature of these data, from the point of view of crystal growth, is the rapid variation of the Hg vapor pressure over the melt with composition, and particularly near the stoichiometric compositions. The variation of vapor pressure of pure Hg, P_{Hg} , is given by

$$\ln P_{\text{Hg}}(\text{atm}) = 11.238 - 7,100/T (^{\circ}\text{K}) \quad (38)$$

For stoichiometric melts, the variation of vapor pressure, P_{HCT} , is given by

$$\ln P_{\text{HCT}}(\text{atm}) = 10.162 - 7,100/T (^{\circ}\text{K}) \quad (39)$$

This expression is valid for $0 \leq x \leq 0.60$ and for $670 \leq t \leq 965^{\circ}\text{C}$. This points out the requirement for good control of the Hg overpressure to maintain stoichiometry in the melt, and therefore uniform solidification. If the Hg vapor pressure is too high, this results in Hg inclusions and blowholes. If it is too low, it leads to partial decomposition and Te inclusions. In both cases, this will also lead to variations in the alloy composition, x . This effect is a significant but often overlooked cause of nonuniformity in HgCdTe material and detectors.

Figure 3-3 shows the actual temperature and pressure parameters for alloy compositions corresponding to 2.06- and 3.85- μm detectors. The liquidus temperatures of 920°C and 845°C correspond to vapor pressures of 67 atm (980 psi) and 45 atm (655 psi) for stoichiometric melts. At the same temperatures, free Hg has pressures in excess of 200 atm (3,000 psi) and 140 atm (2,100 psi), respectively. These should be considered minimum values since in crystal growth from the melt, the charge has to be superheated by 20°C to 25°C to ensure complete dissolution and homogenization.

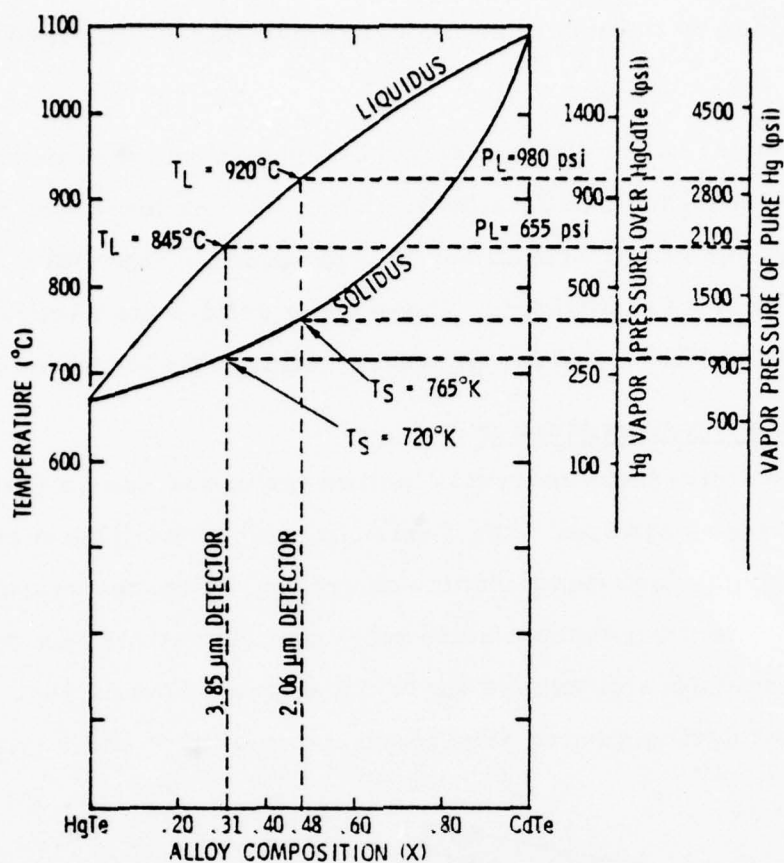


Figure 3-3. Thermodynamic Properties of HgCdTe Alloys for 2.06 and 3.85 μm

CRYSTAL GROWTH METHODS

The preceding discussion of the thermodynamic properties of HgCdTe alloys points up the significant factors and main difficulties to be considered in the growth of high quality material. These can be summarized as follows:

1. The high Hg vapor pressure over the melt makes it difficult to contain the charge (explosion of quartz ampoules), and to control its stoichiometry.
2. Alloy segregation upon freezing can lead to severe lack of uniformity in the material.
3. Additional segregation results from density differentials.

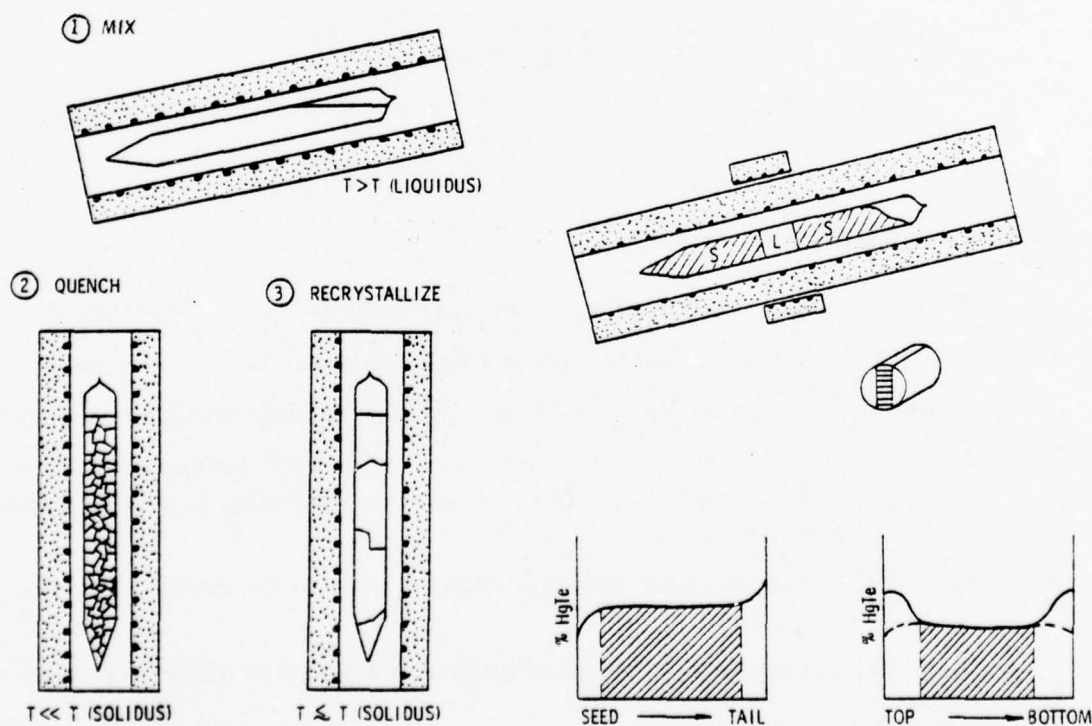
All these problems which are already severe for long-wavelength 8- to 14- μm material ($x = 0.20$) are significantly increased for shorter wavelength

material due to the much higher vapor pressures that have to be contended with.

Because of the limited amount of published work on the preparation of short-wavelength HgCdTe alloys, it was not certain which would be the best way to prepare the material for this program. Therefore, a number of alternate methods were utilized. These were solid-state recrystallization (SSR), zone melting (ZM), and the pressure reflux (PR) techniques.

Solid-State Recrystallization

The solid-state recrystallization technique uses a fast quench to minimize alloy segregation. The dendritic, polycrystalline material is then recrystallized by high-temperature annealing. Figure 3-4a illustrates this method. The macroscopic uniformity may sometimes be poorer because of trapped inclusions of excess Hg or Te at grain boundaries. Also, impurities in the melt during quench are frozen into the ingot and remain there.



(a) Solid State Recrystallization Method

(b) Zone Melting Method

Figure 3-4. HgCdTe Crystal Growth Techniques in Sealed Quartz Ampoules

Zone Melting Technique

A more sophisticated technique previously developed at SBRC on IR&D funding is zone melting in a closed tube (Figure 3-4b). In this process, the charge is first reacted and quenched in a rocking furnace. It is then placed in a zone melting furnace for crystal growth. This is achieved by passing a molten zone through the charge at a slow rate to assure crystal perfection. A pointed tip is made at one end of the quartz ampoule to promote single-crystal growth.

Normal segregation produces compositional nonuniformity at the seed and tail ends of the ingot. There may also be a radial composition variation as shown in the diagram in Figure 3-4b. This is dependent on zone size, the shape of the liquid-solid interface, and the furnace temperature gradients. By empirical methods, it has been possible to minimize the radial nonuniformity to the extent shown by the dashed lines in the figure. This provides an adequate supply of uniform material in the central core of the ingot. An additional advantage to the ZM method is the reduction in impurity content by the zone refining action provided as the molten zone is moved down the ingot.

Another advantage of the zone melting technique for the preparation of short-wavelength material arises because crystal growth takes place at the much lower solidus temperature T_s (Figure 3-3). For 2.06- and 3.85- μm material, this corresponds to temperatures of 765°C and 720°C, respectively. Consequently, the pressure during crystal growth remains below 30 atm (450 psi) if the melt is stoichiometric. The critical step, however, is compounding and quenching of the charge, which still requires temperatures above the liquidus.

Pressure Reflux Technique

A more recent development at SBRC is the open ampoule pressure reflux (PR) technique in which high-purity inert gas and a steep temperature gradient are used to contain the Hg vapor by refluxing (Figure 3-5). This greatly minimizes the dangers of explosions during reaction since the inert gas acts as a flexible membrane and the reflux tube forms a cold reservoir

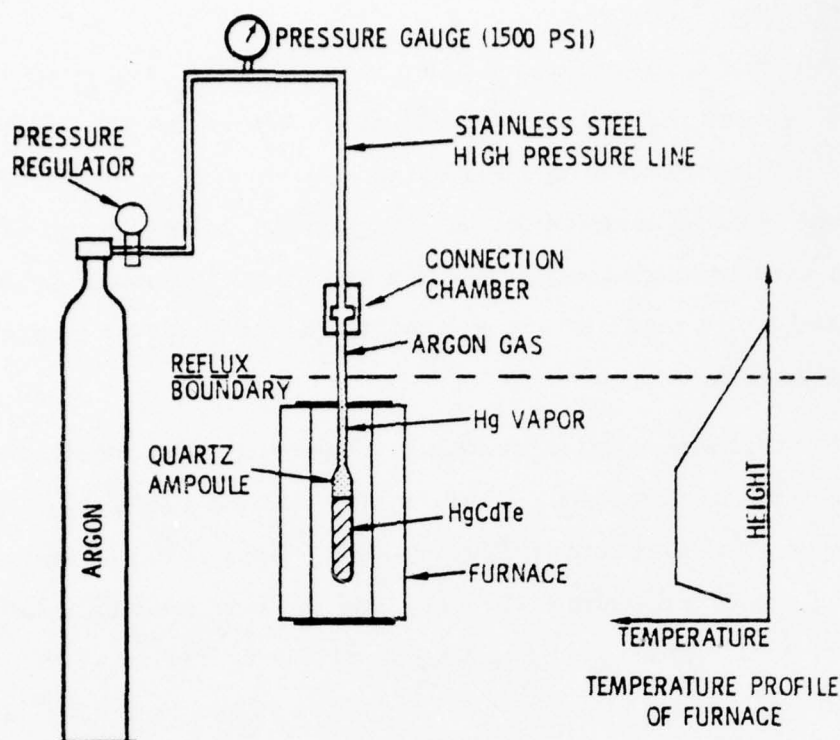


Figure 3-5. Pressure Reflux Technique

for excess Hg vapor. At temperatures above the liquidus during melting, the total pressure of the system remains precisely controlled by the pressure of the inert gas. This eliminates the dangers of explosions due to overheating of Hg vapor. It also provides a means for controlling the stoichiometry of the charge. Pretesting of the quartz ampoules and elimination of stresses due to quartz seal-off result in a system that can operate safely at significantly higher pressures than in sealed quartz ampoules. The SBRC system has been fully tested at pressures in excess of 1,000 psi and therefore satisfies the requirements for 2.06- and 3.85- μ m material.

One of the advantages of the SBRC pressure reflux technique over the previously developed process for growth of HgCdTe in a high-pressure furnace¹⁰ is due to the fact that more uniform temperature profiles can be easily obtained. In the high-pressure furnace, the high-density inert gas surrounding

¹⁰J. Steininger, J. Crystal Growth 37, 107 (1977).

the growth ampoule generates large thermal losses by convection. As a result, good uniformity and reproducibility are difficult to obtain, even with the use of internal heat pipes.

While the problem of pressure containment is not a critical issue in the pressure reflux furnace, material uniformity still remains one of the key factors to the success of this approach.

HgCdTe MATERIAL EVALUATION

Approximately 18 $\text{Hg}_{1-x}\text{Cd}_x\text{Te}$ crystals were grown in support of this program, six with nominal $x = 0.31$ composition and twelve with a nominal $x = 0.48$ composition. All three crystal growth methods were tried with each of these alloy compositions. Because of the limited previous experience at SBRC with these particular alloy compositions, several failures occurred and many of these ingots did not yield a significant amount of useful material. The types of failures encountered were as follows:

1. Off stoichiometry - excess Te (inclusions) or Hg (holes)
2. Excessive strain - crystal severely cracked after removal from quartz ampoule
3. Crystal grain size too small
4. Compositional variations due to segregation during freezing.

In general, the yield of good material was much better for the $x = 0.31$ composition than for $x = 0.48$. Crystals grown later in the program exhibited a much better yield of good material than those grown at the start of the program. More than 50% of the crystals produced did yield some useful material and these were subjected to further evaluation.

Crystal Evaluation

The first evaluation was concerned with alloy uniformity and crystallographic perfection. Alloy uniformity was determined by density measurements. Crystallographic perfection was investigated by metallurgical microscopy and by X-ray topography.

Figures 3-6 through 3-8 show density profiles obtained on some of the HgCdTe ingots. Figure 3-6 is the profile for a $\text{Hg}_{0.52}\text{Cd}_{0.48}\text{Te}$ ingot produced by the SSR method. This ingot was 0.5 inch in diameter and about 8 inches long. The data show this ingot to be very uniform; this is expected from the SSR process. The measured density values confirm a crystal composition $x = 0.48$ within experimental error. The estimated error in the density value is $\pm 0.01 \text{ gm/cm}^3$ and this is represented by the diameter of the data point circles on the figure. According to equation (37), a variation in density of 0.02 gm/cm^3 implies a variation in x -value of 0.01. Thus the density measurement does not give a high precision determination of the x -value. Furthermore, a density measurement on a given wafer determines the average density of that wafer and says nothing about variations within the wafer. More precise determinations of variations in alloy composition are indicated by detector cutoff wavelength.

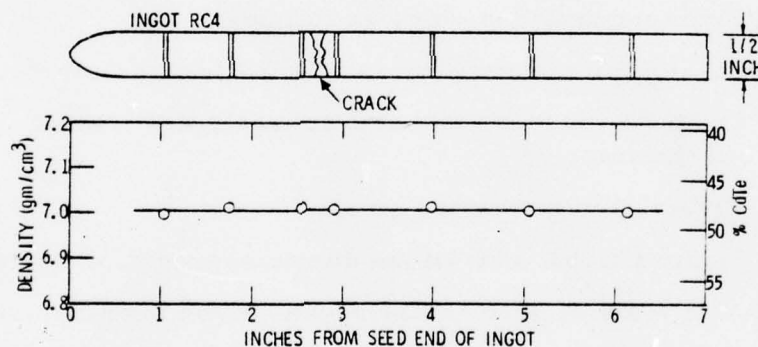


Figure 3-6. Density Profile of Ingot RC4 Grown by the SSR Method

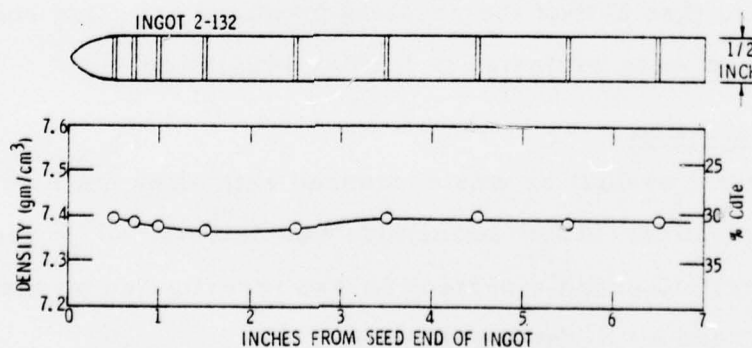


Figure 3-7. Density Profile of Ingot 2-132 Grown by the ZM Method

Figure 3-7 shows the density profile of an ingot produced by the zone melting method. Some density fluctuations are observed near the seed end where continuous adjustments in the zone heater are necessary to stabilize the zone size. The remainder of the ingot appears to be quite uniform. The composition indicated by these density data is $x = 0.31$.

Figure 3-8 shows density profiles on two ingots produced by the pressure reflux technique. One of these ingots (No. 5-16) was 0.75 inch in diameter and about 7 inches long. This ingot was compounded at $x = 0.31$. The other ingot (No. 5-28) was 1.0 inch in diameter and about 5 inches long. This ingot was compounded at $x = 0.48$. The density profile on ingot No. 5-16 shows a gradual decrease in density (increase in x -value) toward the top of the ingot indicating some gravitational segregation during freezing. The profile on No. 5-28 is flat over a portion of the ingot. The upper part dropped off to lower densities due to some porosity. A few wafers also exhibited low density values. Close inspection of these wafers showed this to be due to holes

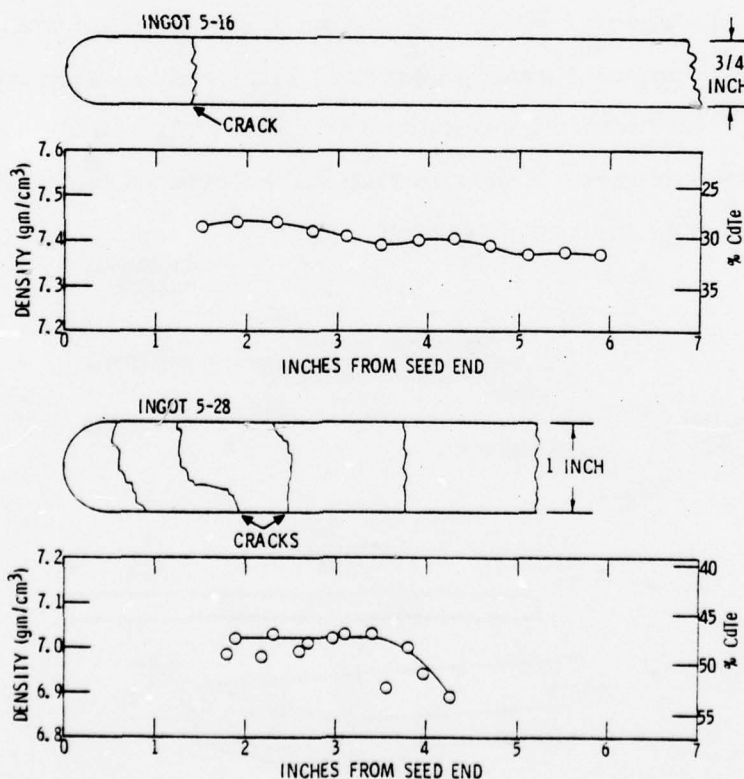


Figure 3-8. Density Profiles of Two Ingots Grown by the PR Method

in these wafers. Therefore, the true density profile is thought to be indicated by the solid line joining higher density points. This indicates an x-value between 0.47 and 0.48.

The crystallographic perfection of a number of wafers was studied by X-ray topography using the Berg-Barrett back reflection method. This method is illustrated by Figure 3-9. A collimated X-ray beam is made incident on the face of a polished and etched wafer. In close proximity to the wafer is a photographic film plate. X-rays are diffracted from the crystal planes at various angles determined by the Bragg condition

$$n\lambda = 2d \sin \theta \quad (40)$$

where λ = X-ray wavelength

n = integer

d = distance between lattice planes

θ = diffraction angle

A region in the crystal where the lattice angle changes with respect to the X-ray beam (such as a grain boundary) will produce a shifted image on the film plate. The method is sensitive to lattice tilt boundaries down to a small fraction of one degree. Other lattice imperfections such as pits, inclusions, or scratches may also be observed.

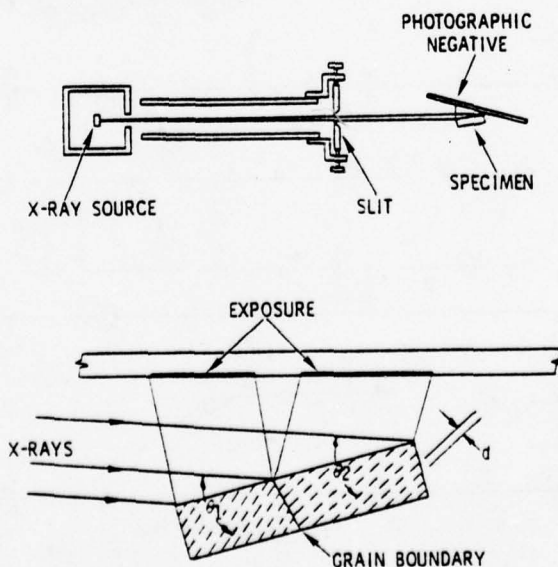


Figure 3-9. Berg-Barrett Back Reflection X-ray Topography

Figures 3-10 through 3-12 show examples of X-ray topographs obtained on various crystals. Figure 3-10 is a topograph taken on a wafer from crystal RC4 grown by the SSR method. A double image is seen because the X-ray beam actually consists of two wavelengths, the Cu $K\alpha_1$ and $K\alpha_2$ lines at 1.5374 and 1.5412 Å, respectively. Since each wavelength has a slightly different Bragg angle, two images on the film plate result. Some parts of the wafer did not even register an image; this is because they are grains of different orientation which diffract the X-ray beam toward some angle well off the film plate. Also seen in the topograph are one large hole and several smaller holes. These are a result of excess Hg in this particular part of the ingot.

Figure 3-11 shows a topograph of a wafer from crystal 2-132 grown by the zone melting method. The striking thing about this picture is the extensive network of low-angle tilt boundaries throughout this wafer. This result has been found to be typical of all HgCdTe material grown by the ZM method. Chemical etching studies have shown a high concentration of edge dislocation etch pits running along these tilt boundaries. This is sometimes referred to as lineage. It has not yet been determined whether or not this type of lattice imperfection has a deleterious effect on the large area PV HgCdTe detectors.

Figure 3-12 shows a topograph of a wafer from crystal WK-9 grown by the SSR method. This wafer again shows relatively good lattice perfection. The striations are due to lack of surface flatness due to chemical etching after the optical polish. They are not a function of lattice perfection. A few small pits may be seen in the wafer on close inspection. The large marks on the edge of the wafer are chips from handling with tweezers.

Annealing

HgCdTe crystals as grown usually contain on the order of 10^{17} to $10^{18}/\text{cm}^3$ Hg vacancies. Since these vacancies produce acceptor centers in the crystal, the material is highly p-type. To obtain the low acceptor concentration material necessary for low-capacitance p-n junctions, the number of vacancies must be reduced. This is easily accomplished by heating the



Figure 3-10. X-ray Topograph of a Wafer from HgCdTe Ingot RC4

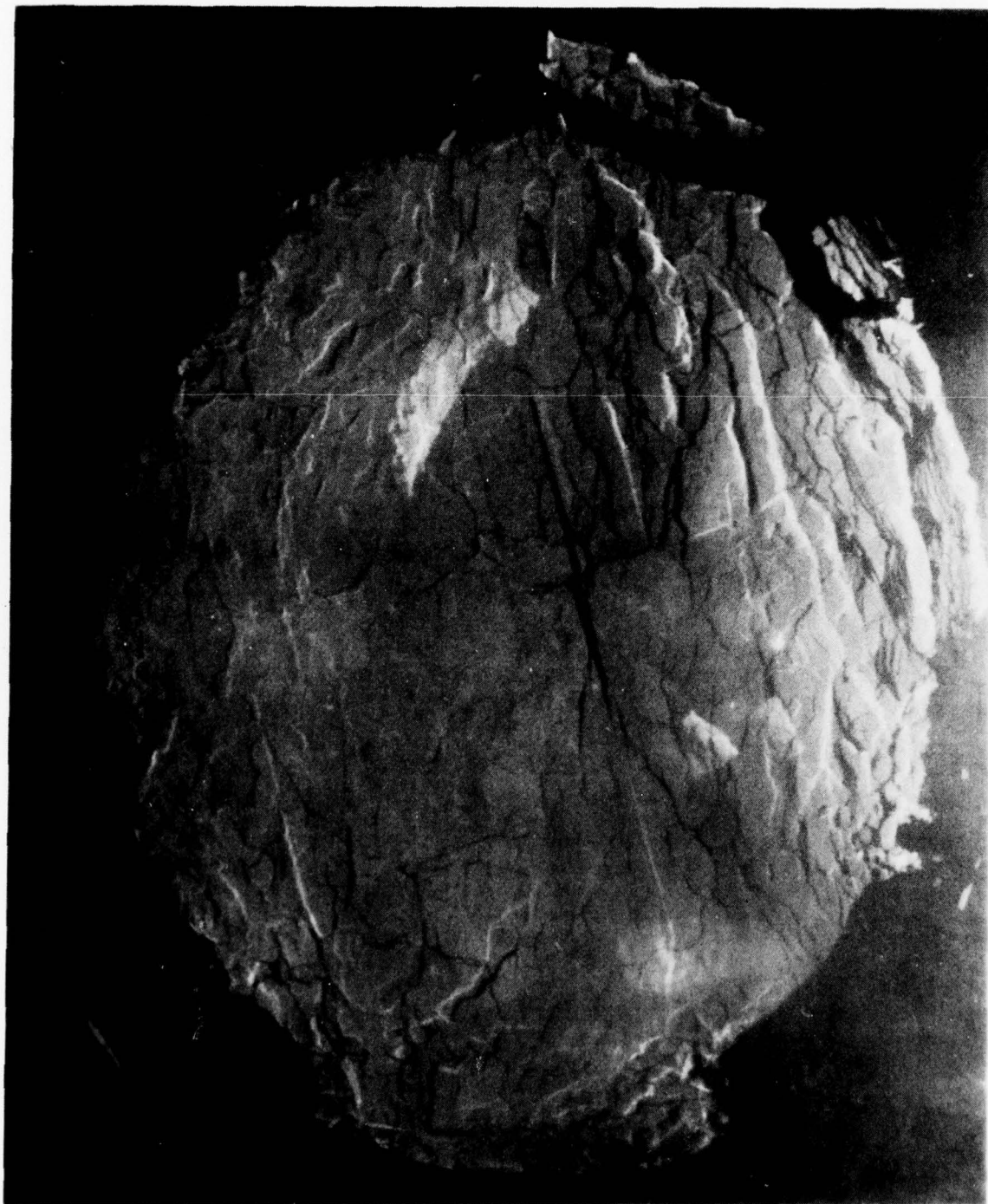


Figure 3-11. X-ray Topograph of a Wafer from HgCdTe Ingot 2-132



Figure 3-12. X-ray Topograph of a Wafer from HgCdTe Ingot WK-9

Figure 3-12. X-ray Topograph of a Wafer from HgCdTe Ingot WK-9

material to temperatures on the order of 300°C in the presence of Hg vapor.^{11,12} A sufficient time must be allotted so that Hg atoms from the vapor phase can diffuse into the HgCdTe and fill the vacancies. A judicious choice of annealing temperature and Hg vapor pressure can leave the material with the desired density of Hg vacancies, and therefore provide p-type material with the desired low acceptor concentration.

On the other hand, it is also possible to dope the crystals with certain impurity atoms which produce acceptor centers. In previous work, SBRC has utilized Au atoms for acceptor doping of HgCdTe. Au has a high enough diffusion coefficient so that it can be introduced into the HgCdTe by solid-state diffusion.¹³ Alternatively, it can be introduced from the melt during crystal growth. Most of the p-type material produced for this program was Au-doped; vacancy doping was only used in a few instances. Acceptor doping concentrations were determined by Hall effect measurements. Figure 3-13 shows Hall coefficient versus reciprocal temperature data acquired on three Au-doped samples of $\text{Hg}_{0.69}\text{Cd}_{0.31}\text{Te}$. In the extrinsic temperature range (i. e., below 200°K), the Hall coefficient R_H is related to free hole concentration p by the expression

$$R_H = \frac{1}{ep} \quad (41)$$

At high temperatures (about 200°K) all Au acceptors are ionized and the hole concentration is given by

$$p = N_{\text{Au}} - N_D \quad (42)$$

where N_{Au} is the Au atom concentration and N_D is the residual donor impurity concentration. For N_D small compared to N_{Au} , then $p \approx N_{\text{Au}}$ and the Au

¹¹R. A. Reynolds, M. J. Brau, H. Kraus, and R. T. Bate, "Proc. of Conf. on Narrow Gap Semiconductors," Dallas (1970), Ed. by Carter and Bate, Pergamon Press, New York (1971), p. 511.

¹²B. E. Bartlett, J. Deans and P. C. Ellen, J. Materials Science 4, 266 (1969).

¹³A. I. Andrievskii, A. S. Teodorovich, and A. D. Schneider, Sov. Phys., Semicond. 7, 1112 (1974).

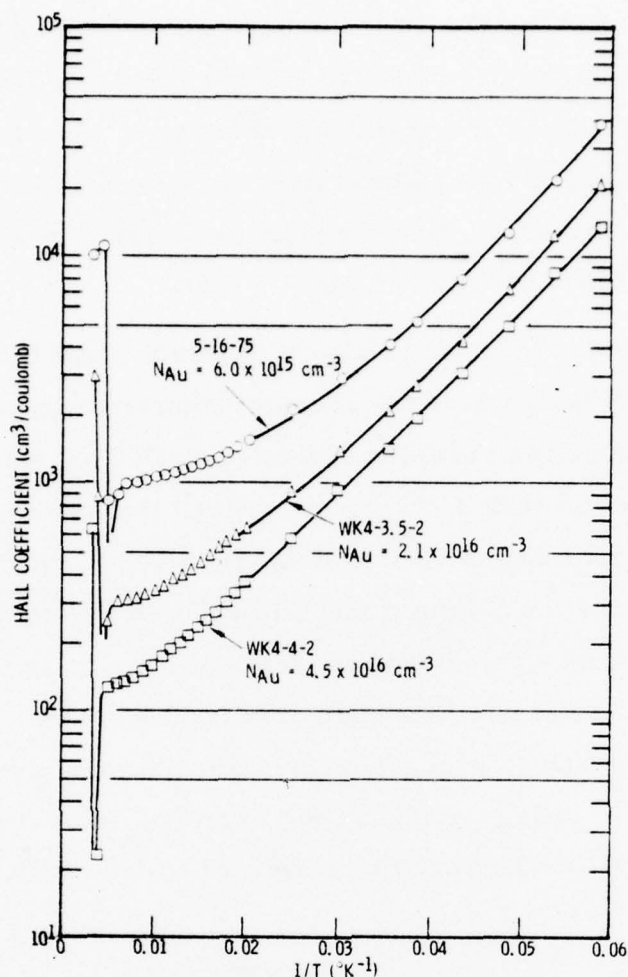


Figure 3-13. Hall Coefficient versus Reciprocal Temperature for Three Au-Doped $\text{Hg}_{0.69}\text{Cd}_{0.31}\text{Te}$ Samples

concentration can be obtained from the measured Hall coefficient. Au concentrations calculated in this way are indicated in Figure 3-13 for the three samples.

At low temperatures, holes "freeze out" on the Au acceptor atoms and the equilibrium free-hole concentration decreases, thereby causing the measured Hall coefficient to increase. At temperatures above 200°K , thermal generation of intrinsic electrons and holes becomes significant. The electrons, because of their much larger mobility, begin to dominate the Hall effect measurement and cause the sign of the Hall coefficient to change from positive to negative.

The electrical measurements on HgCdTe samples also included a measurement of resistivity. The ratio of Hall coefficient to resistivity gives an additional quantity of interest, the hole mobility. Figure 3-14 shows both resistivity and mobility data plotted versus reciprocal temperature for the same three Au-doped samples. Of particular interest in this figure is the decrease in hole mobility in the low-temperature range with increasing dopant concentration. This is attributed to ionized impurity scattering by the Au atoms.

Detailed Hall effect versus temperature measurements were not obtained on $x = 0.48$ material. This was because the annealed region on this

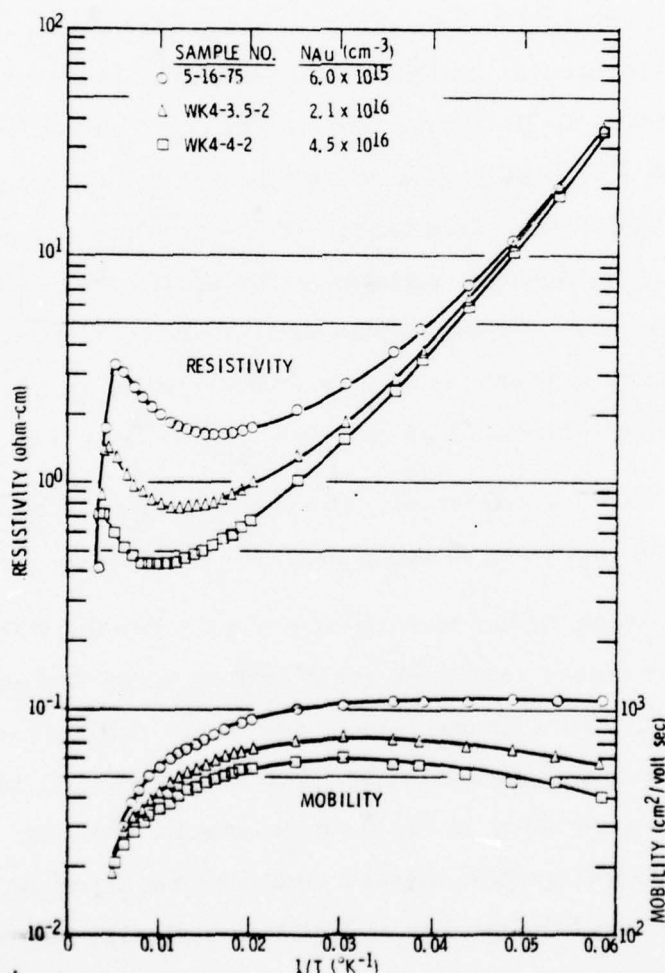


Figure 3-14. Resistivity and Mobility versus Reciprocal Temperature for Three Au-Doped $Hg_{0.69}Cd_{0.31}Te$ Samples

material is only about 20 to 30 μm deep. Such a thin Hall sample is not only difficult to fabricate but is subject to significant perturbations from surface oxide layers which in some cases create an n-type surface inversion layer on p-type material. Such layers cause anomalous Hall coefficient data which cannot be used to determine acceptor doping concentrations. Other techniques for measurement of acceptor doping concentration such as MIS C-V analysis could be used; however, this was not done during the present program.

Material Selection

After evaluation of selected wafers from the various ingots by the methods previously discussed, other wafers were selected for photodiode fabrication. These wafers were usually inspected visually to establish freedom from pits or inclusions and grain boundaries. The ultimate choice of acceptable material was based on the results of photodiode tests to be described in Section 5. It turned out that an ingot grown by the zone melt method (No. 2-132) was judged to be the best for fabrication of large area detectors for 3.85 μm . This ingot had large single-crystal regions, was free of pits and inclusions, and had a composition which gave a peak in the detector response curve which was very close to 3.85 μm . It also had a low residual impurity content (as do most zone melted ingots) so that low acceptor doping concentrations could be achieved (i. e., less than $1 \times 10^{15} \text{ cm}^{-3}$).

For the 2.06- μm detector, an ingot grown by the SSR method (No. RC4) turned out to be the most suitable of those evaluated.

The pressure reflux method of crystal growth, while able to produce large diameter ingots, suffered from rather large variations in composition within the ingot. This probably was due to the difficulties in thoroughly mixing and quenching so large a melt. Too slow a quench rate produces segregation of CdTe-rich alloy in the first-to-freeze regions. Further development of this crystal growth method would be required to bring it to a state where it could yield the quality of HgCdTe material necessary for large area quadrant arrays.

Section 4

PHOTODIODE FABRICATION

JUNCTION FORMATION

The method selected for junction formation in the large area PV HgCdTe detectors was ion implantation. The primary reason for selection of this method was its capability for producing uniform doping concentrations at a precisely controlled depth in the material. Other workers have reported p-n junction formation in HgCdTe using Al,¹⁴ Hg,¹⁵ In,¹⁶ and H¹⁷ ions. For this program, it was decided to use both Al and B ions.

Al and B ions were chosen for study for the following reasons. Previous work had shown that n-type layers could be formed on p-type HgCdTe by Al ion implantation.¹⁴ Al is a known n-type dopant in HgCdTe. Therefore, it was virtually certain that Al implants would be successful. B was not known to be an n-type dopant; however, it is in the same column of the periodic table as Al and could reasonably be expected to produce less damage to the HgCdTe lattice than Al for a given implant depth.

During preliminary junction formation studies on this program, the effect of both Al and B ion implants were investigated. Projected ranges for these ions were calculated using the theory of Linhard, et al,¹⁸ and data tables provided in the book by Gibbons, et al.¹⁹

¹⁴ J. Marine and C. Motte, Appl. Phys. Lett. 23, 450 (1973).

¹⁵ G. Fiorito, G. Gasparrini and F. Svelto, Appl. Phys. Lett. 23, 448 (1973).

¹⁶ Unpublished reports from Honeywell Radiation Center and Arthur D. Little Corp.

¹⁷ A. G. Foyt, T. C. Harman and J. P. Donnelly, Appl. Phys. Lett. 18, 321 (1971).

¹⁸ J. Linhard, M. Scharff, and H. E. Shiøtt, Kgl. Danske Vid. Selsk., Matt.-Fys. Medd. 33, No. 14 (1963).

¹⁹ J. F. Gibbons, W. S. Johnson, and S. W. Mylroie, "Projected Range Statistics", Published by Dowden, Hutchinson and Ross, Stroudsburg, Pa. (1975).

Figure 4-1 shows the calculated profile for the case of Al^+ ions implanted at 300 keV into $\text{Hg}_{0.7}\text{Cd}_{0.3}\text{Te}$. The calculated projected range R_p was $0.2423 \mu\text{m}$ and the standard deviation in range ΔR was $0.1273 \mu\text{m}$. This calculation was made for a total ion dose of $3.2 \times 10^{13}/\text{cm}^2$ which yields a maximum ion concentration of $1 \times 10^{18}/\text{cm}^3$ at R_p . If the acceptor doping concentration in the base material is $2 \times 10^{15}/\text{cm}^3$, then the p-n junction would be located $0.70 \mu\text{m}$ below the top surface. A very similar implanted ion profile would be produced by B^+ ions implanted at 110 keV.

The implants were made at room temperature and, in most cases, the samples received no annealing after implantation. The electrical properties

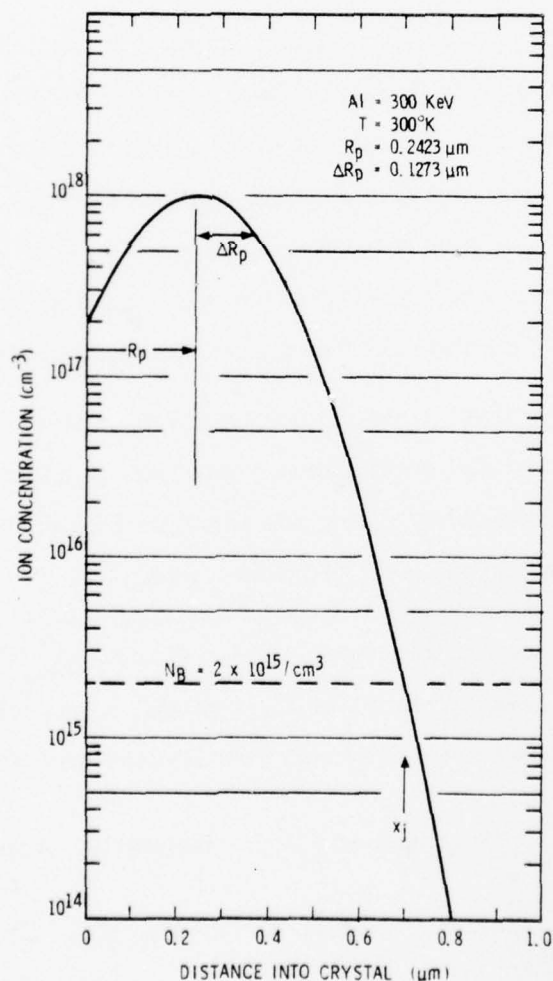


Figure 4-1. Calculated Ion Concentration Profile for an Al^+ Implant into $\text{Hg}_{0.7}\text{Cd}_{0.3}\text{Te}$.

of the implanted layers were investigated by means of Hall effect and resistivity measurements using the van der Pauw sample configuration shown in Figure 4-2.

A clover leaf pattern is photoetched into the top of the implanted area and four ohmic contacts are applied. Hall effect and resistivity measurements are then made in the manner described by van der Pauw.²⁰ If the junction isolation resistance is high enough, the measuring current will pass only through the top layer and the measured Hall voltage and resistivity will reflect only the properties of this layer.

Table 4-1 shows the data acquired on a number of wafers used for the ion-implantation study. The sixth and seventh columns of this table compare the calculated average doping concentration in the implanted layer with the values obtained from van der Pauw measurements. It is seen that, for the

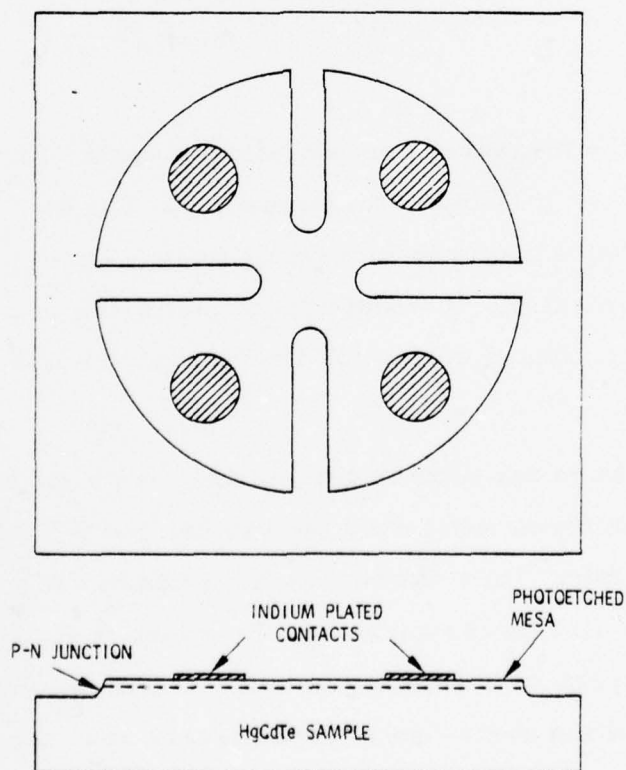


Figure 4-2. Van der Pauw Hall Sample Layout

²⁰ L. J. van der Pauw, Philips Research Reports 13, 1 (1958).

Table 4-1. Comparison of Calculated and Measured Ion Implant Doping in $\text{Hg}_{0.7}\text{Cd}_{0.3}\text{Te}$ Wafers

RUN NO.	WAFER NO.	IMPLANTED ION	DOSE (cm^{-2})	$N_{(\text{max})}$ (cm^{-3})	$N_{(\text{ave})}$ (cm^{-3})	$N_{(\text{meas})}$ (cm^{-3})	RESISTIVITY (Ωcm)
A11149	WK-4A	Al	3.2×10^{13}	1×10^{18}	4.6×10^{17}	2.3×10^{18}	8.4×10^{-4}
A11150	WK-4B	Al	3.2×10^{14}	1×10^{19}	4.6×10^{18}	1.3×10^{18}	2.0×10^{-3}
A11151	WK-4C	Al	3.2×10^{15}	1×10^{20}	4.6×10^{19}	0.8×10^{18}	2.2×10^{-3}
A11152	2-74-9I	Al	3.2×10^{13}	1×10^{18}	4.6×10^{17}	1.7×10^{18}	1.0×10^{-3}
A11153	2-74-9K	Al	3.2×10^{14}	1×10^{19}	4.6×10^{18}	1.0×10^{18}	1.4×10^{-3}
B2235	2-74-9A	B	3.7×10^{13}	1×10^{18}	5.3×10^{17}	-	-
B2236	2-74-9B	B	3.7×10^{14}	1×10^{19}	5.3×10^{18}	-	-
B2237	2-74-9C	B	3.7×10^{15}	1×10^{20}	5.3×10^{19}	2.2×10^{18}	7.9×10^{-4}
B2238	WK-4D	B	3.7×10^{13}	1×10^{18}	5.3×10^{17}	3.0×10^{18}	8.2×10^{-4}
B2239	WK-4E	B	3.7×10^{14}	1×10^{19}	5.3×10^{18}	-	-

$$N_{(\text{max})} = \frac{\text{DOSE}}{\sqrt{2\pi} \Delta R_p}; \quad N_{(\text{ave})} = \frac{\text{DOSE}}{X_j}$$

$$\text{FOR Al AT 300 keV: } \begin{aligned} R_p &= 0.2423 \mu\text{m} \\ \Delta R_p &= 0.1273 \mu\text{m} \\ X_j &= 0.7 \mu\text{m} \end{aligned}$$

$$\text{FOR B AT 110 keV: } \begin{aligned} R_p &= 0.2373 \mu\text{m} \\ \Delta R_p &= 0.1479 \mu\text{m} \\ X_j &= 0.7 \mu\text{m} \end{aligned}$$

lowest dose, the measured concentration is higher than expected and, for the higher doses, it is lower than expected. The measured doping concentration actually decreases with increasing dose. This is directly opposite from the expected behavior. It would appear that there is considerable lattice damage being produced during the implant and the damage centers are electrically active.

The question can also be raised that, since the implanted ion distribution is not uniform, what does the van der Pauw Hall measurement actually measure? Petritz²¹ has shown that for a number of colaminar conducting layers with no circulating currents, the effective Hall mobility is weighted in favor of the layers with a higher mobility. This would weight the measured data in favor of the more lightly doped layers and, therefore, produce values which are too low. While this effect might account for errors of a factor of

²¹ R. L. Petritz, Phys. Rev. 110, 1254 (1958)

2 or so, it seems unlikely that it could produce the factors of 20 or 60 seen with the highest implant doses.

We believe that the anomalous effects observed in this investigation are due primarily to the lattice damage produced by these highly energetic implants. The damage produced appears to be rather complex and there also may be an interaction between damage centers and dopant ions. As a side experiment, an implantation of Ne ions into p-type HgCdTe was made. No van der Pauw Hall effect data were taken; however, photodiodes were made and rectification curves similar to those obtained with B and Al were observed. Since Ne should be an inert dopant in HgCdTe, it was concluded from this experiment that damage centers in HgCdTe can have an n-type character. From this result, it would also appear that the photodiodes of Foyt, et al,²² made by proton bombardment of p-type HgCdTe were made by a damage doping mechanism.

The damage produced in HgCdTe by ion implantation appears to be relatively permanent. Some wafers were annealed at temperatures up to 200°C. Again, no van der Pauw data were taken; however, comparison of the I-V curves on photodiodes made in both annealed and unannealed material showed no significant difference. Foyt, et al also observed that their photodiodes made by proton bombardment were stable at temperatures up to 100°C.

This brief investigation of the physics of ion implantation into HgCdTe has revealed the complexity of the process. A detailed investigation of lattice damage and annealing thereof was considered to be beyond the scope of the present program. Having established an approximate doping level of about $1 \times 10^{18}/\text{cm}^3$ for an implant dose of about $3 \times 10^{13}/\text{cm}^2$, it was decided to use this as the baseline process for junction formation. The B ion was selected for use over Al because it was found to work just as well and probably introduces less lattice damage because it is implanted at a lower energy.

²² See Reference 17.

FABRICATION METHOD

A set of procedures was worked out for fabrication of large area photodiode detectors. The photodiodes were made as either mesa or planar photodiode devices as shown in Figure 4-3. A "picture frame" top contact made with evaporated indium was used in the initial design. The "nominal" sensitive area is defined as that area inside the picture frame contact. Photodiodes were made with nominal sensitive areas of $1 \times 1 \text{ mm}^2$, $2 \times 2 \text{ mm}^2$ and $5 \times 5 \text{ mm}^2$. Since there is also some sensitive area outside the picture frame contact, the true sensitive area is always somewhat larger than the

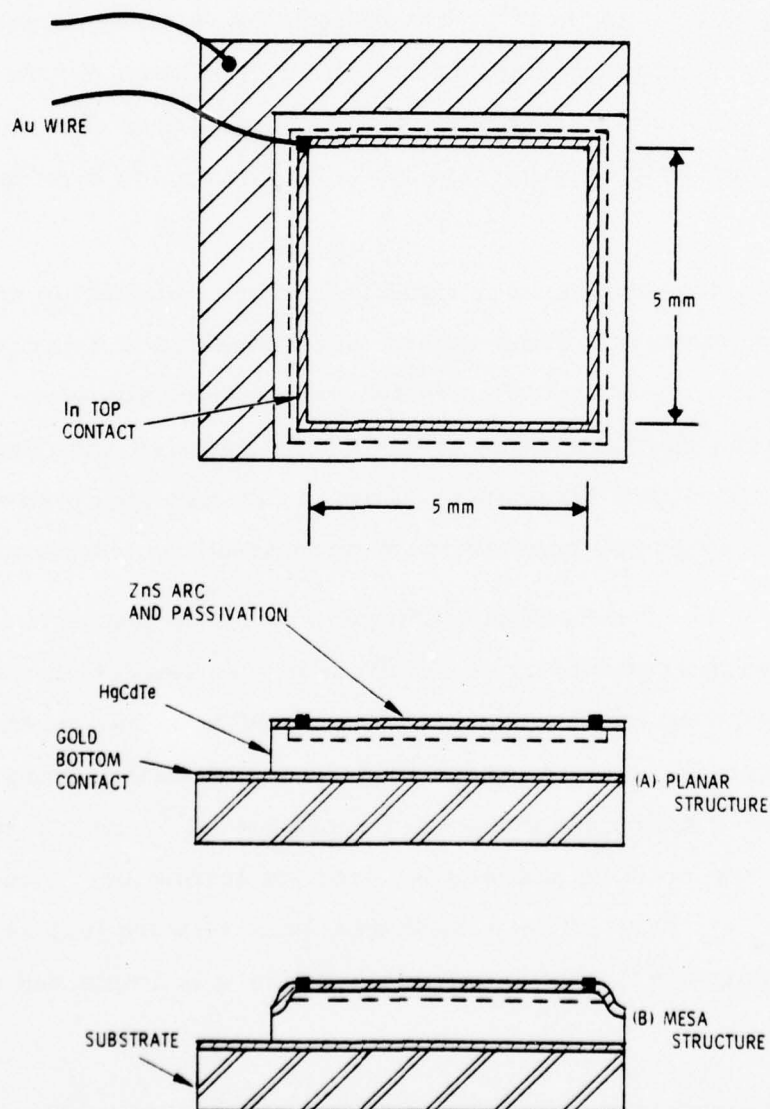


Figure 4-3. Large Area PV HgCdTe Photodiode Construction

nominal sensitive area. The true area was always used for D^* calculations. The total junction area is somewhat larger than the true sensitive area because it also includes the area under the picture frame contact.

The original purpose of the picture frame contact was to minimize the series resistance in the thin implanted top layer which might adversely affect the sensitivity contour of the detector. Because of the very low resistivity measured for a doping concentration of $10^{18}/\text{cm}^3$ (see Table 4-1), it was decided that half of the picture frame could be left off, leaving just an "L" shaped contact. Measurements showed that this did not significantly alter the sensitivity contour. This design change eliminated obscuration due to contacts in the central area of the quadrantal arrays which were later fabricated from large area single detectors (see Section 5 for further details).

The processing procedure worked out for the fabrication of these large area PV HgCdTe detectors was as follows:

(A) Planar Devices

1. Obtain annealed p-type HgCdTe wafer
2. Lap and etch back side
3. Plate backside with Au
4. Saw wafer into chips of appropriate size
5. Mount chip on Ti/Au metallized sapphire substrate with conducting epoxy
6. Polish and etch top side
7. Apply photoresist masking to define desired junction area
8. Ion implant to form p-n junction
9. Remove photoresist
10. Evaporate ZnS antireflection coating
11. Apply photoresist pattern to define area for top metal contact
12. Etch contact window in the ZnS
13. Evaporate In top metal
14. Remove photoresist and excess evaporated In

15. Attach Au lead wire to corner of In contact with conducting epoxy
16. Attach gold wire to base contact on the Ti/Au metallization of the sapphire substrate
17. Mount in dewar for test

(B) Mesa Devices

- 1-6. Same as above
7. Ion implant top side
8. Apply photoresist pattern to define desired junction area
9. Etch mesa
10. Remove photoresist
11. Perform steps 10-17 as listed above.

During the early part of this program, the photodiode fabrication work was centered on nominal $1 \times 1 \text{ mm}^2$ and $2 \times 2 \text{ mm}^2$ devices. Later on, when some uniform, high quality crystal material was identified, the work was shifted to the nominal $5 \times 5 \text{ mm}^2$ devices. As shown in Figure 4-3, the fabrication of these large area photodiodes was done in a manner such that, after pretesting, four single-element detectors could be pieced together to form the desired quadrantal array.

OPTICAL CONSIDERATIONS OF THE DESIGN

Because of the high doping concentration on the n-side of the p-n junction, the material is highly degenerate and the Fermi level lies well up into the conduction band. The situation is shown schematically in the energy band diagram of Figure 4-4(a). For degenerate material with a parabolic energy band structure, the relation between electron concentration n and the position of the Fermi level above the conduction band edge is ²³

$$n = \left(\frac{8\pi}{3} \right) \left(\frac{2m^*}{h^2} \right)^{3/2} (E_{Fn} - E_c)^{3/2} \quad (43)$$

²³ W. Shockley, "Electrons and Holes in Semiconductors", D. Van Nostrand Co., Inc., Princeton, N. J. (1950) p. 241.

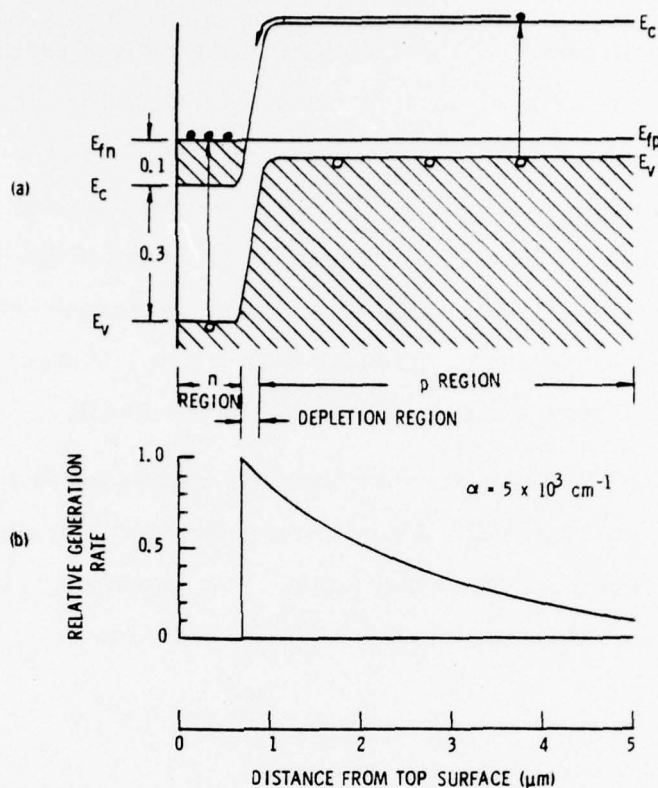


Figure 4-4. Optical Absorption Model for Ion Implanted Photodiodes. (a) Energy Band Diagram, (b) Relative Generation Rate Due to Absorbed Photons Having $\lambda > 3 \mu\text{m}$.

where m^* is the electron effective mass and h is Planck's constant. For HgCdTe alloys, the conduction band is not parabolic. However, this equation can still be used as a first approximation. By solving for the Fermi energy in terms of electron concentration, the equation becomes

$$(E_{Fn} - E_c) = 3.64 \times 10^{-15} \left(\frac{m_0}{m^*} \right)^{2/3} n \quad (44)$$

where m_0 is the free electron mass. Using the values $n = 1 \times 10^{18}/\text{cm}^3$ and $m^*/m_0 = 0.037$,²⁴ it is found that $(E_{Fn} - E_c) = 0.1 \text{ eV}$. The diagram in Figure 4-4(a) is drawn using this value.

²⁴ L. Sosnowski and R. R. Galazka, In "II-VI Semiconducting Compounds-1967 International Conference", Edited by D. G. Thomas, W. A. Benjamin, Inc., New York (1967) p. 888.

The significance of this result is that optical transitions in the lightly doped p-type side of the junction can be produced by photons of energy equal to or greater than the band gap energy ($E_C - E_V$). For a HgCdTe alloy with $x \approx 0.32$, $(E_C - E_V) = 0.3$ eV at 77°K. However, on the n-type side the optical transitions must go from the valence band to above the Fermi level and $(E_{F_n} - E_V) \approx 0.4$ eV. Thus the n-type layer is essentially transparent to photons having wavelengths greater than 3 μm . These photons will be absorbed on the p-type side as shown in Figure 4-4(b).

Since the minority carrier lifetime can be quite long in this lightly doped region, and because the minority carrier is a high mobility electron, the diffusion length can be quite long. For example, letting $\tau_n = 5 \times 10^{-7}$ sec, $\mu_n = 4 \times 10^4$ cm²/volt sec, and $T = 77^\circ\text{K}$, we have

$$L_n = \left(\tau_n \mu_n \frac{kT}{e} \right)^{\frac{1}{2}} = 115 \mu\text{m} \quad (45)$$

Such a long diffusion length will permit very efficient collection of the minority carriers at the p-n junction and give high quantum efficiency. Quantum efficiency is further enhanced by the application of the ZnS antireflection coating over the top surface of the photodiode. A quarter-wave coating is used which by direct measurement has been shown to reduce the reflectance to less than 5% at the wavelength of interest.

Section 5

DETECTOR TEST RESULTS

The work on this program began with small area detectors having nominal sensitive areas of $1 \times 1 \text{ mm}^2$ and $2 \times 2 \text{ mm}^2$. This was done for the purpose of checking out various crystals of HgCdTe and also for working out the detector fabrication procedures. Later on in the program, work was shifted to the fabrication of $5 \times 5 \text{ mm}^2$ detectors. With HgCdTe material designed for $2.06\text{-}\mu\text{m}$ detection, only the smaller area devices were made. With HgCdTe material designed for $3.85\text{-}\mu\text{m}$ detection, both small and large area devices were made. In this section, the results obtained with $3.85\text{-}\mu\text{m}$ detectors are presented first; the results on $2.06\text{-}\mu\text{m}$ detectors follow.

3.85- μm PV HgCdTe DETECTORS

Small Area Detectors

Evaluation of WK4 Material - A test array of circular mesa-type photodiodes was made on wafer No. WK4. This material was produced by the SSR process and was nominally 31% CdTe. A diagram of this array is shown in Figure 5-1. The mesa diameters were each about 0.053 inch. Hall effect

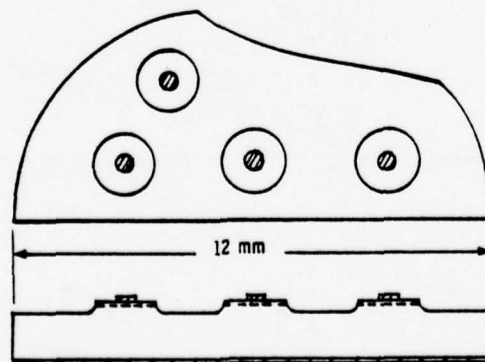


Figure 5-1. Layout of Four Mesa-Type Photodiodes on Half-Wafer No. WK4. Nominal Mesa Diameter is 0.053 Inch

measurements indicated an acceptor doping concentration of $2 \times 10^{16} \text{ cm}^{-3}$ in this wafer. The p-n junction was formed by B^+ ion implantation as described in Section 4.

Measurements were made on this array at three different temperatures, 77° , 145° , and 192°K . Figure 5-2 shows the current versus voltage curves at these temperatures. These curves show that, at the highest operating temperature, saturation current is high, causing large current flow in the reverse direction as well as a fast turn-on in the forward direction. At the lowest operating temperature, saturation current is low and the diode reverse current is probably leakage limited. At the intermediate operating temperature, the effect of increasing saturation current is just beginning to

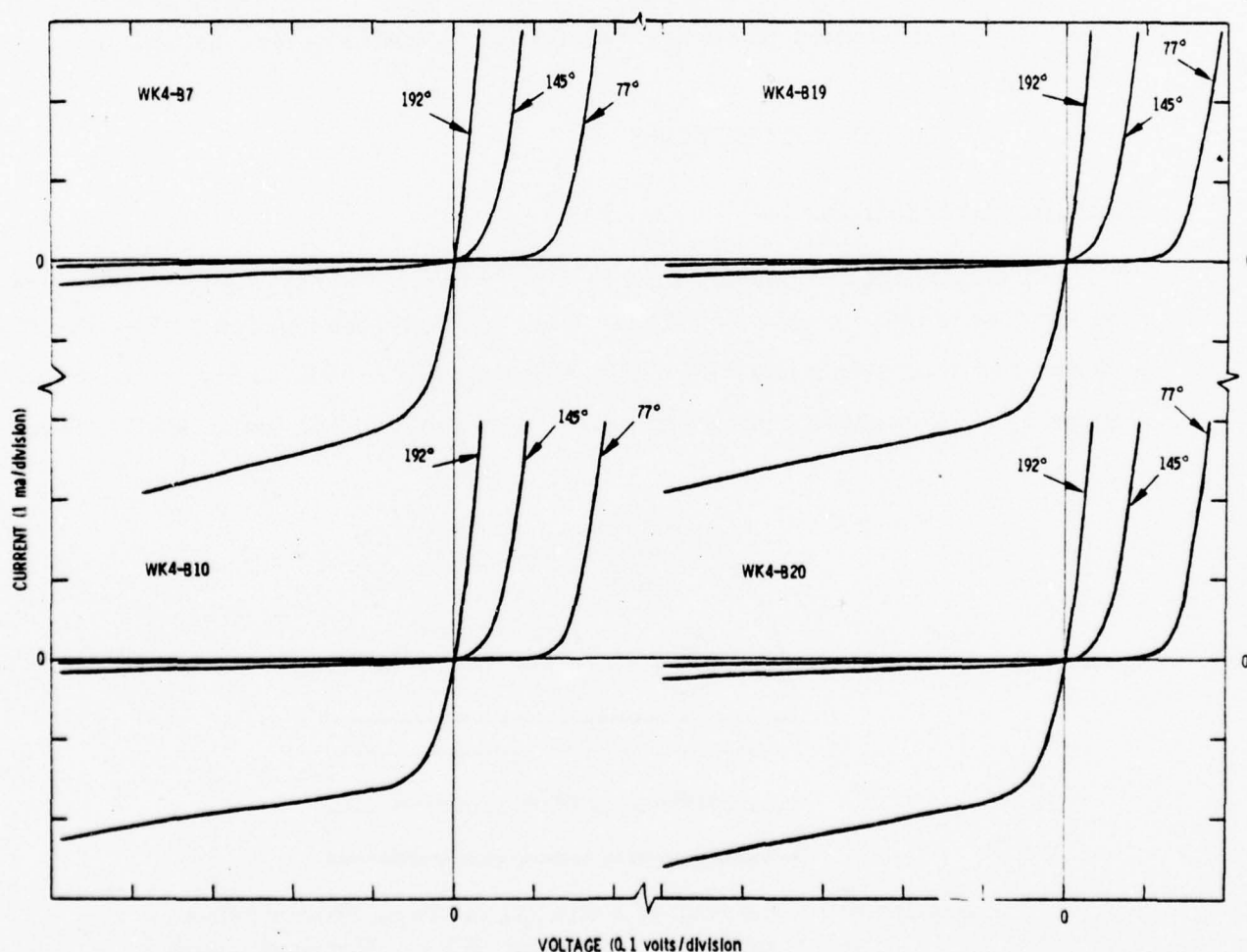


Figure 5-2. Current versus Voltage Characteristics for Four Photodiodes from Wafer WK4. R_{0A_j} Values are Listed in Table 5-1

be seen. The short-circuit photocurrent I_p due to background photons was on the order of $10 \mu\text{A}$ for these photodiodes and is, therefore, not seen with the current scale used for plotting this figure.

Figure 5-3 shows relative spectral response measurements for one of these photodiodes, No. WK4-20, at two temperatures, 77° and 145°K . Data at 192°K was not obtained because of poor signal-to-noise ratio (SNR) with our spectrometer. However, the calculated long-wavelength cutoff edge for this temperature is sketched on the figure as a dashed line. This calculation was based on a measured band gap widening with increasing temperature of $2.4 \times 10^{-4} \text{ eV}/^\circ\text{K}$. The spectral response of this material is adequate for detection of $3.85\text{-}\mu\text{m}$ laser radiation at all temperatures up to and above 200°K .

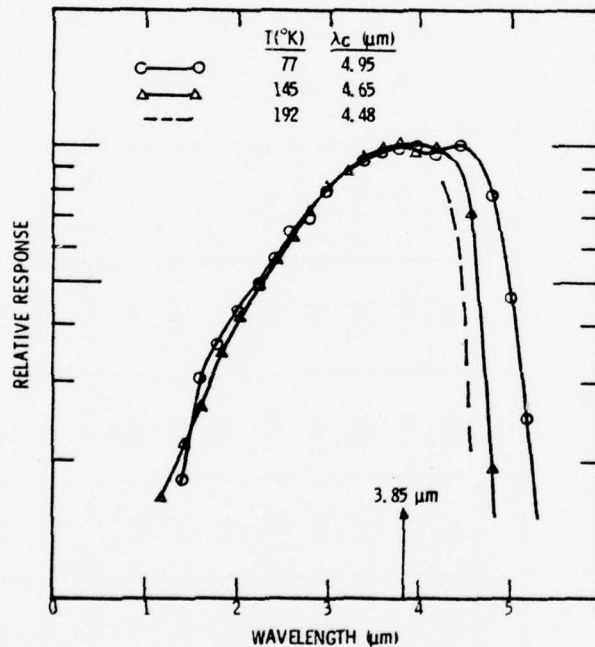


Figure 5-3. Relative Spectral Response at Three Temperatures for Detector No. WK4-B20

Measurements were also made of the detector properties of this photodiode such as responsivity, detectivity, and quantum efficiency. These data are summarized in Table 5-1 along with the dynamic resistance and capacitance data. All detectors were background photon noise limited (BLIP) when operated at 77°K and had quantum efficiencies of 40% to 50%. At 145°K ,

Table 5-1. Summary of Detector Properties of a Four-Element
PV HgCdTe Array Made from Wafer WK4

TEMPERATURE (°K)	77°				145°				192°			
	B7	B10	B19	B20	B7	B10	B19	B20	B7	B10	B19	B20
A_d (mm ²)	1.13	1.19	1.24	1.07	1.13	1.19	1.24	1.07	1.13	1.19	1.24	1.07
A_f (mm ²)	1.45	1.51	1.56	1.39	1.45	1.51	1.56	1.39	1.45	1.51	1.56	1.39
R_0 (ohms)	62K	131K	77K	66K	335	560	500	600	16	16	12	14
$R_0 A_f$ (ohm cm ²)	900	1,980	1,200	917	4.9	8.4	7.8	8.3	0.23	0.24	0.12	0.19
C_0 (pf)	998	871	973	823	-	-	-	-	-	-	-	-
C_0/A_f (pf/mm ²)	688	577	624	591	-	-	-	-	-	-	-	-
$I(\lambda_p)$ (a/w)	1.30	1.54	1.32	1.46	1.55	1.39	1.44	1.47	-	-	-	-
$D^* (\lambda_p, 2\text{KHz})$ (cm Hz ^{1/2} /w)	1.1×10^{11}	1.1×10^{11}	1.2×10^{11}	1.0×10^{11}	3.0×10^{10}	3.4×10^{10}	4.0×10^{10}	3.7×10^{10}	4.0×10^9 (ESTIMATED VALUE)	-	-	-
λ_p (μm)	4.00	4.00	4.00	4.00	3.9	3.9	3.9	3.9	-	-	-	-
η (at λ_p)	0.40	0.48	0.41	0.45	0.50	0.45	0.46	0.47	-	-	-	-

FOV ≈ 180°

detectivities dropped to around $3 \text{ to } 4 \times 10^{10} \text{ cm Hz}^{\frac{1}{2}}/\text{watt}$ and the detectors were no longer BLIP. At 192°K , detectivity dropped another order of magnitude to around $4 \times 10^9 \text{ cm Hz}^{\frac{1}{2}}/\text{watt}$. Because of the lack of accurate spectral response data, an accurate detectivity at λ_p could not be obtained. The value given in the table is an estimate.

Evaluation of 2-124 Material - A six-element test array of nominal $1 \times 1 \text{ mm}^2$ planar photodiodes was made on wafer 80 from crystal 2-124. This crystal was grown by a zone melting method. The nominal composition of this material was 32% CdTe, and the base region acceptor doping concentration was approximately $3 \times 10^{16} \text{ cm}^{-3}$. The layout of this detector array is shown in Figure 5-4. Testing of these detectors was also conducted at three temperatures, 77° , 145° , and 192°K .

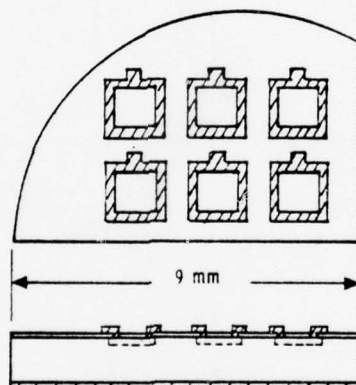


Figure 5-4. Layout of Six-Element Array of $1 \times 1 \text{ mm}^2$ Photodiodes on Wafer 2-124-80.

Figure 5-5 shows current versus voltage curves for these six photodiodes. At 77°K , all have a low reverse saturation current indicative of high R_o . The saturation current increases as temperature is increased. Although not evident with the current scale used for this figure, R_o values were found to drop by nearly three orders of magnitude on going to 145°K and by another order of magnitude at 192°K . Actual $R_o A_j$ data are presented in the summary (Table 5-2) for this array. Reverse breakdown commences at about 0.5 volt for all of these diodes.

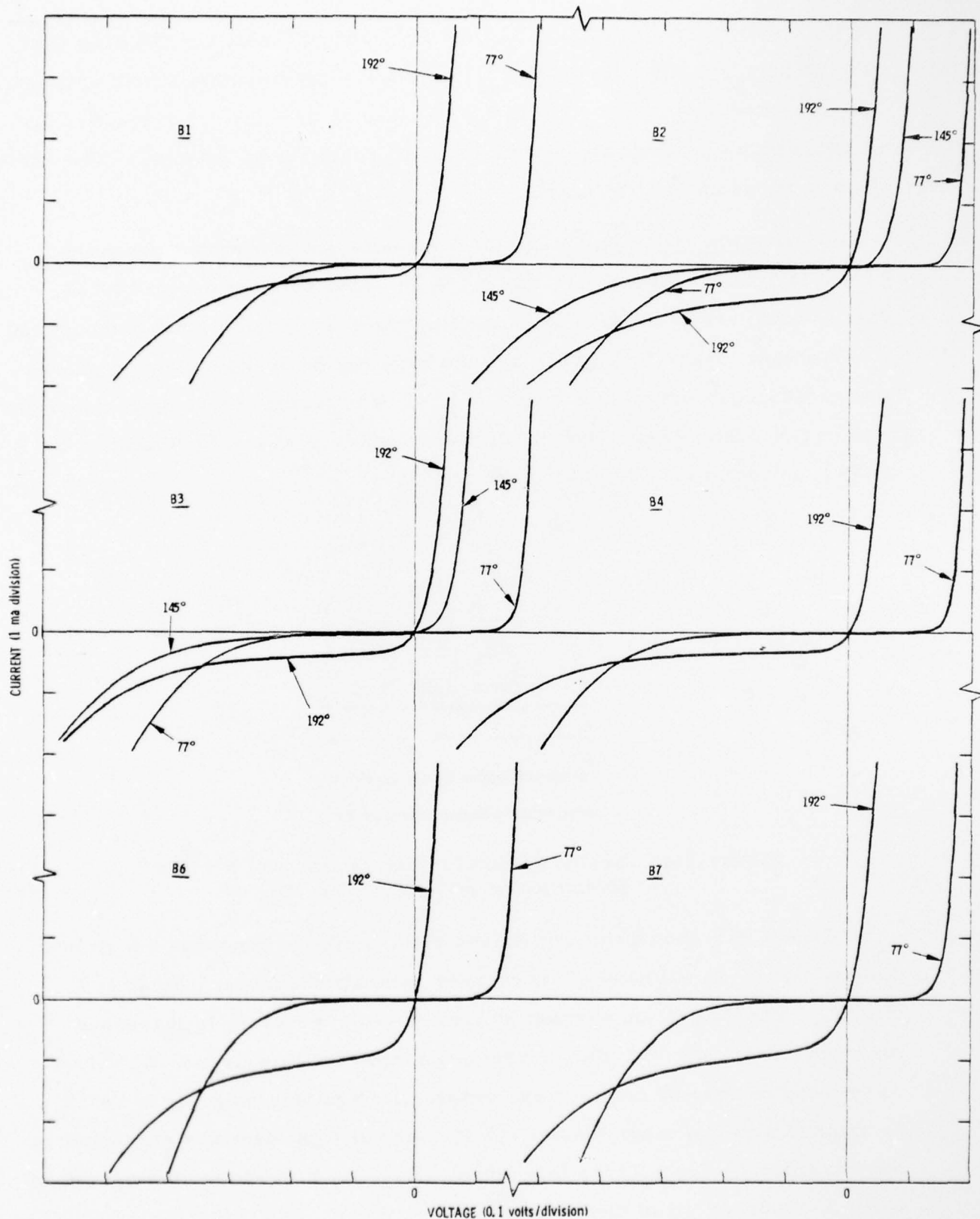


Figure 5-5. Current versus Voltage Characteristics for Six Photodiodes from Wafer 2-124-80 at Temperatures of 77°, 145°, and 192°K

Figure 5-6 shows the relative spectral response for one element of this array (B2) measured at the three temperatures. The cutoff wavelength of this material is close to $3.85 \mu\text{m}$, but the peak response is short of $3.85 \mu\text{m}$ for all operating temperatures. The shift of cutoff wavelength with increasing temperature corresponds to a bandgap dilation of $2.0 \times 10^{-4} \text{ eV}/^\circ\text{K}$ in agreement with the published data of Schmit and Stelzer.²⁵ The alloy composition of this material is a little too rich in CdTe. It would be more desirable to have the peak of the spectral response curve occur closer to the principle wavelength of interest, namely $3.85 \mu\text{m}$.

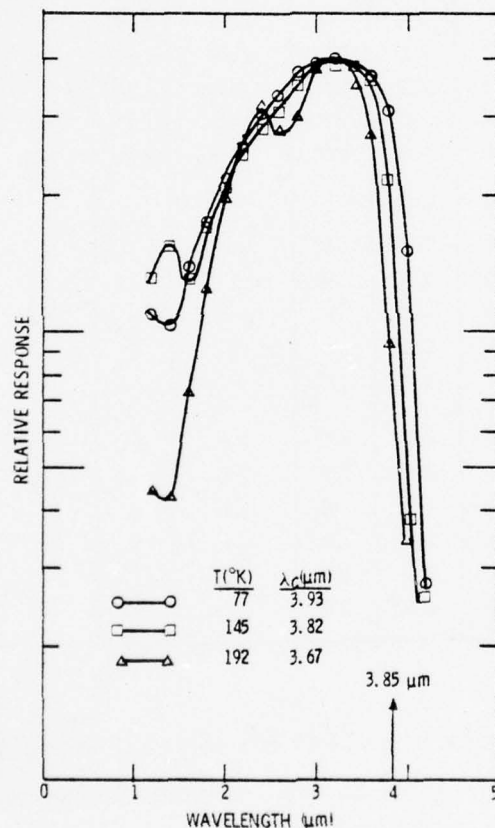


Figure 5-6. Relative Spectral Response at Three Temperatures for Detector No. 2-124-80-B2

²⁵ See Reference 7.

The detector properties of these photodiodes were measured and are listed in Table 5-2. At 77°K, four of the six detectors have BLIP limited detectivities and the other two are operating at about one-half of the BLIP limit. These two detectors did not suffer from low $R_o A_j$ or low quantum

Table 5-2. Summary of Detector Properties of a Six-Element PV HgCdTe Array Made from Wafer 2-124-80

DIODE NO.	T (°K)	A_d (mm ²)	A_j (mm ²)	R_o (ohms)	$R_o A_j$ (ohm cm ²)	C_o (pf)	C_o/A_j (pf/mm ²)	$I(\lambda_p)$ (a/w)	$D^* \lambda_p$ (2KHz) (cm Hz ^{1/2} /w)	λ_p (μm)	η (AT λ_p)
2-124-80											
81	77	1.0	2.32	105K	2.4K	1,832	790	1.42	2.5×10^{11}	3.2	0.55
82	77	1.0	2.32	530K	12.3K	1,989	860	1.55	2.4×10^{11}	3.2	0.60
83	77	1.0	2.32	300K	7.0K	1,803	780	1.42	2.3×10^{11}	3.2	0.55
84	77	1.0	2.32	530K	12.3K	1,748	750	1.38	2.8×10^{11}	3.2	0.54
86	77	1.0	2.32	133K	3.1K	1,273	550	1.45	1.3×10^{11}	3.2	0.56
87	77	1.0	2.32	400K	9.3K	1,086	470	1.33	1.2×10^{11}	3.2	0.52
81	145	1.0	2.32	-	-	-	-	-	3.9×10^{10}	3.0	-
82	145	1.0	2.32	1,840	43	-	-	-	7.9×10^{10}	3.0	-
83	145	1.0	2.32	730	17	-	-	-	4.0×10^{10}	3.0	-
84	145	1.0	2.32	-	-	-	-	-	4.0×10^{10}	3.0	-
86	145	1.0	2.32	-	-	-	-	-	3.3×10^{10}	3.0	-
87	145	1.0	2.32	-	-	-	-	-	2.7×10^{10}	3.0	-
81	192	1.0	2.32	120	2.8	-	-	-	3.9×10^9	3.0	-
82	192	1.0	2.32	38	0.9	-	-	-	6.7×10^9	3.0	-
83	192	1.0	2.32	60	1.4	-	-	-	3.6×10^9	3.0	-
84	192	1.0	2.32	70	1.6	-	-	-	1.9×10^9	3.0	-
86	192	1.0	2.32	20	0.5	-	-	-	-	3.0	-
87	192	1.0	2.32	30	0.7	-	-	-	1.2×10^9	3.0	-

FOV $\approx 180^\circ$

efficiency, but exhibited excess noise from some unknown source. At 145°K, the detectivity drops down to the 10^{10} cm Hz^{1/2}/watt range, and at 192°K, it is down in the 10^9 cm Hz^{1/2}/watt range. The drop in detectivity at elevated temperature is due to the drop in $R_o A_j$ product.

The capacitance per unit area values for these detectors are comparable to those for the WK4 material described previously. This is as expected because the base acceptor doping is about the same in the two wafers.

Evaluation of 5-20 Material - Test detector arrays were fabricated on two wafers of 5-20 HgCdTe material which was produced by the pressure reflux technique. The wafer numbers were 108 and 131. These wafers were doped with an acceptor concentration of about $2 \times 10^{16} \text{ cm}^{-3}$. The detectors were made by the planar method and were nominal $1 \times 1 \text{ mm}^2$ in area. The device layout was similar to that shown previously in Figure 5-4 for the 2-124-80 material. Four elements were tested on wafer 2-20-108, and nine on wafer 2-20-131.

The test results on these detectors are given in Table 5-3. The main thing to be noted in this table is the variation in long-wavelength cutoff λ_c .

Table 5-3. Summary of Detector Properties of Photodiode Arrays Made on Wafers 5-20-108 and 5-20-131

DIODE NO.	T (°K)	A _{d2} (mm ²)	A _{j2} (mm ²)	R _o (ohms)	R _o A _{j2} (ohm cm ²)	C _o (pf)	C _o /A _{j2} (pf/mm ²)	D ² (Apl) (cm Hz ^{1/2} /w)	λ_p (μm)	λ_c (μm)
<u>5-20-108</u>										
1	77	1.0	2.32	3K	70	-	-	5.2×10^{10}	3.7	4.4
3	77	1.0	2.32	330K	7,700	-	-	1.0×10^{11}	3.7	4.2
9	77	1.0	2.32	18K	420	-	-	7.7×10^{10}	3.8	4.5
10	77	1.0	2.32	53K	1,200	-	-	7.9×10^{10}	3.7	4.3
1	192	1.0	2.32	20	0.5	-	-	2.0×10^9	3.5	4.1
3	192	1.0	2.32	100	2.3	-	-	1.1×10^{10}	3.5	3.9
9	192	1.0	2.32	50	1.2	-	-	6.0×10^9	3.6	4.2
10	192	1.0	2.32	60	1.4	-	-	6.1×10^9	3.5	4.0
<u>5-20-131</u>										
1	77	1.0	2.32	333K	7.7K	-	-	1.0×10^{11}	3.0	3.7
3	77	1.0	2.32	444K	10.3K	1,788	770	0.9×10^{11}	2.9	3.3
4	77	1.0	2.32	400K	9.3K	1,608	692	2.3×10^{11}	2.6	3.0
5	77	1.0	2.32	135K	3.1K	1,370	590	0.7×10^{11}	2.8	3.2
6	77	1.0	2.32	364K	8.5K	1,360	586	0.4×10^{11}	2.9	3.3
7	77	1.0	2.32	230K	5.3K	1,443	622	1.0×10^{11}	3.0	3.6
9	77	1.0	2.32	667K	15.5K	1,439	620	2.4×10^{11}	2.9	3.1
10	77	1.0	2.32	500K	11.6K	1,552	669	1.3×10^{11}	2.8	3.0
11	77	1.0	2.32	1.1M	25.5K	1,865	804	2.2×10^{11}	2.8	3.0
1	192	1.0	2.32	115	2.7	-	-	0.7×10^{10}	3.0	3.5
3	192	1.0	2.32	750	17.4	-	-	3.0×10^{10}	2.7	3.1
4	192	1.0	2.32	850	19.7	-	-	4.0×10^{10}	2.4	2.8
5	192	1.0	2.32	750	17.4	-	-	2.3×10^{10}	2.6	3.0
6	192	1.0	2.32	800	18.5	-	-	1.9×10^{10}	2.7	3.1
7	192	1.0	2.32	270	6.3	-	-	1.2×10^{10}	2.8	3.4
9	192	1.0	2.32	3,000	70	-	-	3.7×10^{10}	2.7	2.9
10	192	1.0	2.32	2,800	65	-	-	3.6×10^{10}	2.6	2.8
11	192	1.0	2.32	7,250	168	-	-	7.0×10^{10}	2.6	2.8

FOV = 180°

which was found in this material. The variation is $0.3\text{ }\mu\text{m}$ in wafer 5-20-108 and $0.7\text{ }\mu\text{m}$ in wafer 5-20-131. Moreover, the variation between the two wafers is more than $1.0\text{ }\mu\text{m}$, and they were cut from the same crystal. The cutoff wavelengths for 5-20-108 are suitable for detection of $3.85\text{-}\mu\text{m}$ radiation, but for 5-20-131, they are too short.

The variation of R_0A_j product and $D^*(\lambda_p)$ within a given wafer is also somewhat greater than has been seen on other material. Although this could be due to array processing problems, on the other hand, it may also be indicative of material imperfections. The conclusion drawn from these test results was that this particular ingot would not be suitable for large area quadrant array fabrication.

Evaluation of WK9 Material - The next material evaluated was from crystal WK9 which was grown by the SSR method and was nominally 31% CdTe. The acceptor base doping in this material was approximately $5 \times 10^{15}\text{ cm}^{-3}$. One set of test photodiodes was made in the mesa form previously used on WK4 material. The mesa areas were nominally $1 \times 1\text{ mm}^2$ as before. Other test photodiodes were made by the planar technique with nominal sensitive areas of $2 \times 2\text{ mm}^2$. Testing of these detectors was done only at 77°K .

Figure 5-7 shows the current versus voltage curves for the four-element mesa photodiode array. One of these diodes had a very good I-V characteristic; the other three were poor. R_0A_j values ranged from 3.7 to 940 ohm cm^2 . Figure 5-8 shows the I-V curves for the $2 \times 2\text{ mm}^2$ planar photodiodes. These curves indicate R_0A_j values ranging from 77 to $2,040\text{ ohm cm}^2$. All the $2 \times 2\text{ mm}^2$ photodiodes exhibited premature reverse breakdown. This may possibly be a surface breakdown effect which would be connected by a better surface passivation treatment. However, the wide variation in R_0A_j values led us to suspect that material defects might also be playing a role in this material.

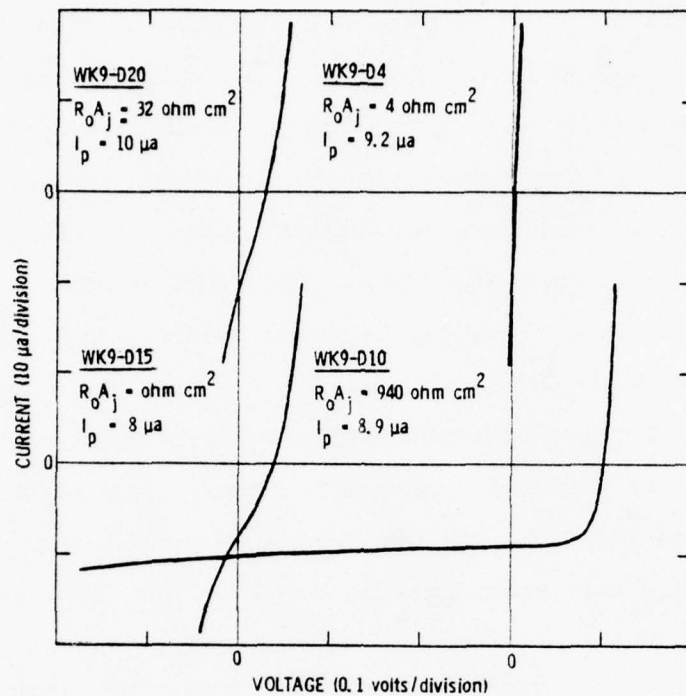


Figure 5-7. Current versus Voltage Curves for a Four-Element Mesa Array from Crystal WK9. $T = 77^\circ K$

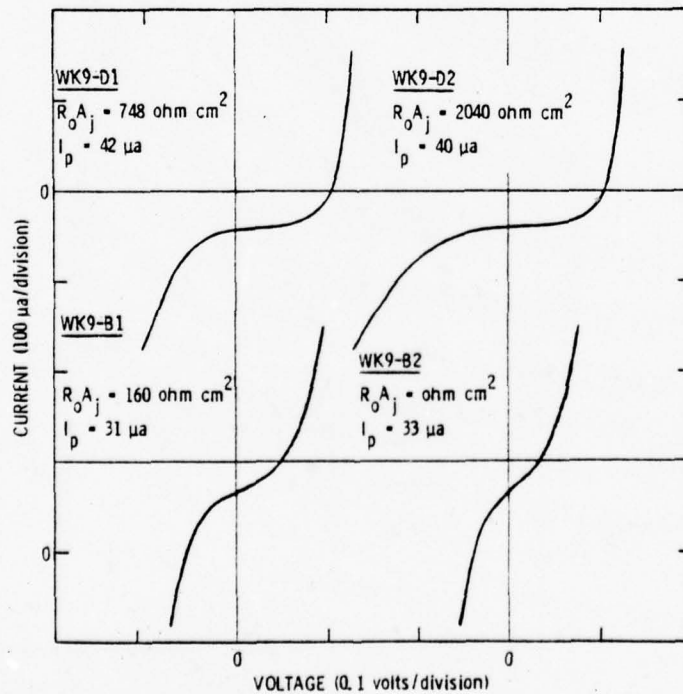


Figure 5-8. Current versus Voltage Curves for Four Nominal $2 \times 2 \text{ mm}^2$ Planar Photodiodes from Crystal WK9. $T = 77^\circ K$

The relative spectral response was measured on two of these photodiodes at 77°K and is shown in Figure 5-9. The cutoff wavelength is nearly identical for these two detectors. This demonstrates the good compositional uniformity of SSR material. The shape of these curves is very similar to that measured on WK4 material which was previously discussed. This is reasonable because the alloy composition is the same. Some differences in spectral response curve shapes may be produced by the antireflection coating, which is applied over the photodiode sensitive area. In the case of the curves shown in Figure 5-9, as well as those shown previously in Figure 5-3, the antireflection coating was a quarter-wave in thickness, peaked for a wavelength of 3.8 μm . This gives the spectral response curve a somewhat flat-topped appearance which may seem unusual if one did not consider the effect of this coating.

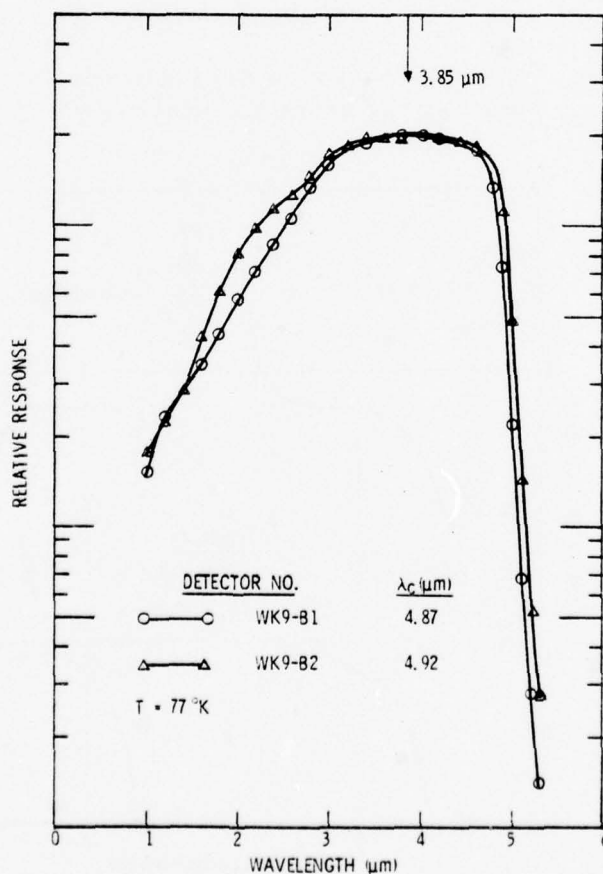


Figure 5-9. Relative Spectral Response for Two Photodiodes from Crystal WK9

The detector properties of all the test photodiodes made from WK9 are listed in Table 5-4. Three of these detectors exhibited BLIP limited detectivity values in the 10^{11} cm Hz^{1/2}/watt range. As expected, these were the ones with the highest R_0A_j values. The detectors with low R_0A_j values

Table 5-4. Summary of Detector Properties of Photodiodes Made from Crystal WK9

DIODE NUMBER	D1	D2	D4	D10	D15	D20	81	82
A_d (mm ²)	5.40	5.40	0.84	0.88	0.75	0.84	5.40	5.40
A_j (mm ²)	6.45	6.45	0.99	1.08	0.95	1.04	6.45	6.45
R_0 (ohms)	116K	317K	370	87K	6K	3.1K	2.5K	1.2K
R_0A_j (ohm cm ²)	748	2,040	4	940	57	32	160	77
C_0 (pf)	2,622	2,548	-	473	-	-	-	-
C_0/A_j (pf/mm ²)	406	395	-	440	-	-	-	-
I (A_d) (a/w)	2.2	2.5	-	2.8	2.9	2.8	-	-
$D^* (\lambda_D, 2kHz)$ (cm Hz ^{1/2} /watt)	1.2×10^{11}	1.7×10^{11}	2.4×10^9	1.4×10^{11}	7.0×10^{10}	3.5×10^{10}	6.1×10^{10}	4.2×10^{10}
λ_D (μm)	4	4	4	4	4	4	4	4
η (at λ_D)	0.69	0.78	-	0.87	0.90	0.87	-	-

T = 77°K

FOV ≈ 180°

showed detectivities significantly less than the BLIP limit. The capacitance per unit area of these photodiodes has been lowered to about 400 pf/mm² because of the lower base acceptor doping concentration.

Evaluation of 2-132 Material - The next material evaluated was from crystal 2-132, which was produced by the zone melting method. This material was nominally 32% CdTe. Hall effect measurements at 77°K indicated that the acceptor doping concentration in this material was in the range 1 to 2×10^{15} cm⁻³. A pair of nominal 2×2 mm² photodiodes were made by the planar process on part of Slice 10 for the purpose of evaluating this material. Testing of these detectors was done only at 77°K.

Figure 5-10 shows the current versus voltage curves on these two photodiodes. Fairly high R_0A_j values are obtained. The reverse breakdown is on the order of 0.4 to 0.5 volt which is low by some standards, but as good or better than many of the photodiodes measured on this program.

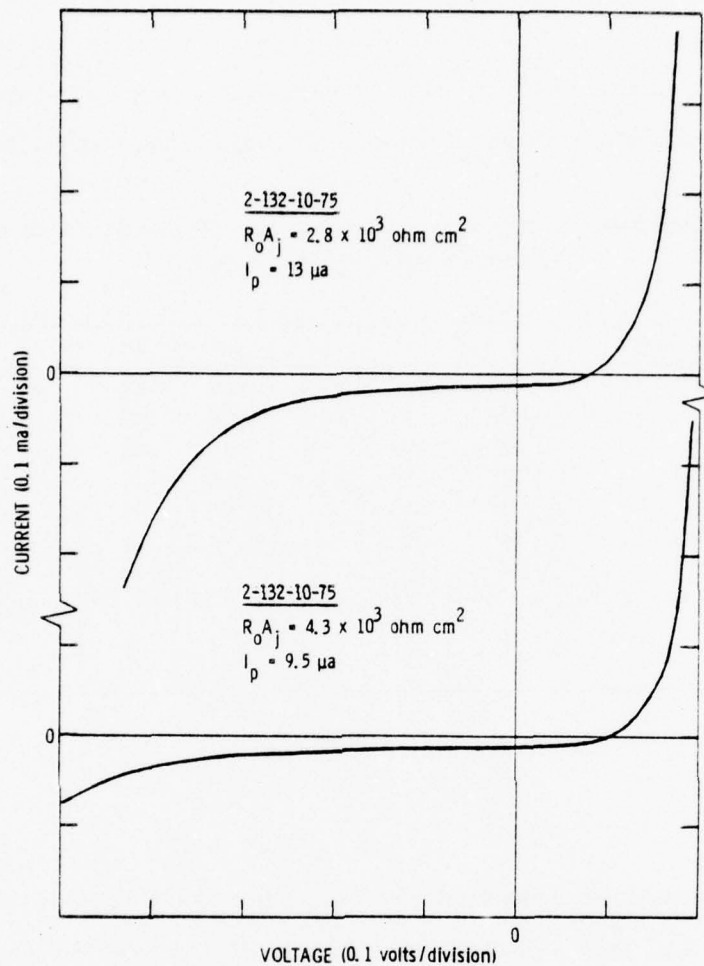


Figure 5-10. Current versus Voltage Curves for Two Photodiodes from Wafer 2-132-10. $T = 77^\circ\text{K}$

The measured difference in short-circuit current I_p due to background photons is a result of a slightly different cutoff wavelength for these two detectors. Because the 300°K photon spectral distribution is rising rapidly with wavelength at $4\text{ }\mu\text{m}$, a slight difference in cutoff can produce a significant difference in number of photons which are effective in producing photocurrent.

Figure 5-11 shows the relative spectral response of these two detectors. This material has a peak response right at the desired value of $3.85\text{ }\mu\text{m}$. A slight difference in cutoff wavelength is seen between the two detectors. This reflects a small alloy compositional variation which is sometimes seen in the

zone melted crystals. In this case, the variation is not enough to be of significance for detection of 3.85- μm radiation.

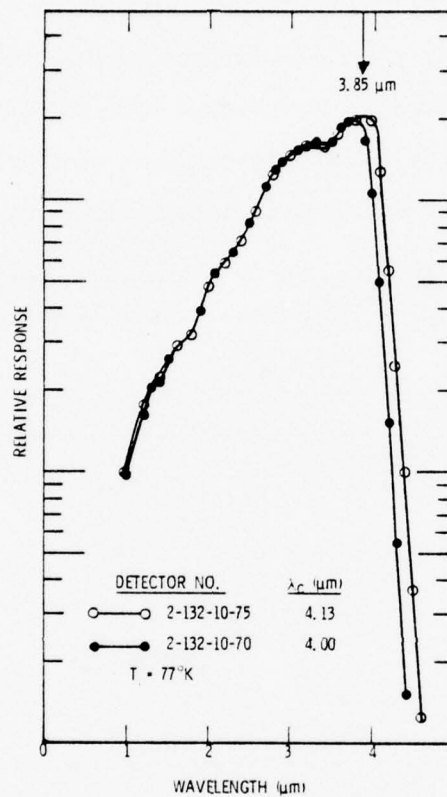


Figure 5-11. Relative Spectral Response for Two Photodiodes from Wafer 2-132-10

The measured detector properties for these two photodiodes are summarized in Table 5-5. A much lower capacitance per unit area was obtained on these devices because of the lower base doping concentration. The quantum efficiencies are extremely high, and this may also be due to the low base doping. The minority carrier lifetime in such material would be quite long (on the order of 0.5 μ sec) producing a long diffusion length which would result in very efficient collection of these carriers at the p-n junction. The detectivity values are essentially at the BLIP limit for both detectors.

Table 5-5. Summary of Detector Properties of Two Photodiodes from Wafer 2-132-10

DIODE NUMBER	2-132-10-70	2-132-10-75
A_d (mm ²)	5.40	5.40
A_j (mm ²)	6.45	6.45
R_0 (ohms)	6.7×10^4	4.3×10^4
$R_0 A_j$ (ohm cm ²)	4.3×10^3	2.8×10^3
C_0 (pf)	374	909
C_0/A_j (pf/mm ²)	136	141
f (λ_p) (a/w)	2.79	2.96
D^* (λ_p , 2 kHz) (cm Hz ^{1/2} /w)	4.0×10^{11}	2.8×10^{11}
λ_p (μ m)	3.8	3.9
η (at λ_p)	0.91	0.92

FOV $\approx 180^\circ$

T = 77°K

Because of the ideal spectral response, the low capacitance per unit area, high quantum efficiency and high detectivity obtained on these test detectors, it was decided to use this particular crystal for the fabrication of the larger 5×5 mm² detector elements required for the large area quadrant arrays.

Large Area Detectors

After completion of material evaluations and demonstration of a suitable device fabrication process using smaller area detectors, work was begun on fabrication and test of large area detectors. Most of these detectors were made from crystal 2-132, which was produced by the zone melting method. A few were made from other crystals. About three dozen nominal $5 \times 5 \text{ mm}^2$ detectors were fabricated with about twenty of these reaching final test and evaluation. Most were made by the mesa process previously described in Section 4; a few were made by the planar process. Testing was done only at liquid nitrogen temperature.

Table 5-6 summarizes the low-frequency test data acquired on fourteen of these large area detectors. The measured zero bias junction dynamic resistance values were on the order of 10^3 ohms. Junction capacitance values were on the order of 4,000 pf. The measured cutoff wavelength varied from 3.8 to 4.3 μm . This is a variation of only 0.5 μm over the whole length of ingot number 2-132 and demonstrates the good uniformity which can be

Table 5-6. Summary of Detector Properties for Fourteen Large Area Photodiodes Made from Ingot 2-132

ELEMENT NUMBER	R_0 (ohms)	C_0 (pf)	λ_D (μm)	λ_C (μm)	$I_r (\lambda_D)$ (a/w)	η (AT λ_D)	$D^* (\lambda_D^2 \text{kHz})$ ($\text{cm Hz}^{-1/2}/\text{w}$)
2-132-11	2,420	4,407	3.8	3.9	2.46	0.81	3.8×10^{11}
2-132-12	1,720	-	3.9	4.1	2.06	0.66	2.1×10^{11}
2-132-13	1,700	3,927	3.8	3.9	2.50	0.84	2.9×10^{11}
2-132-14	2,200	4,611	3.7	3.9	2.37	0.80	3.2×10^{11}
2-132-15	1,500	3,923	3.8	3.9	1.85	0.61	2.4×10^{11}
2-132-18	1,050	-	3.8	3.9	2.40	0.79	2.9×10^{11}
2-132-19	714	-	3.7	3.9	2.16	0.73	2.0×10^{11}
2-132-20	570	-	3.7	3.9	1.63	0.54	1.0×10^{11}
2-132-21	1,000	-	4.0	4.2	3.50	1.09	3.2×10^{11}
2-132-25	800	-	4.1	4.3	2.82	0.85	2.6×10^{11}
2-132-28	3,300	6,700	3.8	4.0	4.30	1.41	4.4×10^{11}
2-132-29	5,000	-	4.0	4.1	2.70	0.84	2.7×10^{11}
2-132-94	1,700	4,930	3.6	3.8	2.48	0.86	2.8×10^{11}
2-132-103	1,090	4,331	3.6	3.8	2.58	0.89	3.0×10^{11}

$T = 77^\circ\text{K}$

$\text{FOV} \approx 180^\circ$

$A_j = 0.312 \text{ cm}^2$

$A_d = 0.284 \text{ cm}^2$

achieved with the ZM process of crystal growth. Since the tail end of the ingot (slice numbers around 100) exhibited cutoff wavelengths that were a little too short, most of the large area detectors were made from wafers cut from the other end of the ingot.

The measured quantum efficiencies averaged about 80% for this group of large area detectors. It will also be noted that two detectors gave anomalously high values of quantum efficiency, 109 and 141%. This is probably due to some systematic error, and these values should be disregarded. The measured low-frequency $D^*(\lambda_p)$ values are around 3×10^{11} cm Hz^{1/2}/watt. This is essentially equal to the background limited value applying to our particular test conditions, namely, 180° FOV of room temperature background radiation. Therefore, most of these detectors are operating at the BLIP limit.

Figure 5-12 shows the relative spectral response curves for two of these large area detectors. The shape of these curves may be considered typical of those measured on 3.85- μ m detectors made from ingot No. 2-132. The relative response is not proportional to λ as expected for a true quantum detector; it rises more rapidly and peaks in the 3.8- to 4.0- μ m range. This spectral shape may be attributed to a combination of two effects. The first is the antireflection coating which is a quarter-wave coating peaked at 3.85 μ m. This increases the optical transmittance into the sample by about 40% at the peak wavelength but provides no increase at a wavelength of one-half the peak which in this case is 1.93 μ m. The second effect contributing to the unusual spectral response shape has to do with the energy band population on the n-side of the p-n junction and was previously discussed in Section 4 in connection with Figure 4-4. The n-side is transparent to photons with wavelength greater than about 3 μ m. Thus these photons pass through into the p-side where they create minority electrons, which are efficiently collected by the p-n junction. Photons with wavelength less than 3 μ m may be absorbed on the n-side where they would create minority holes. However, because of the extensive lattice damage on this side produced by the ion-implantation

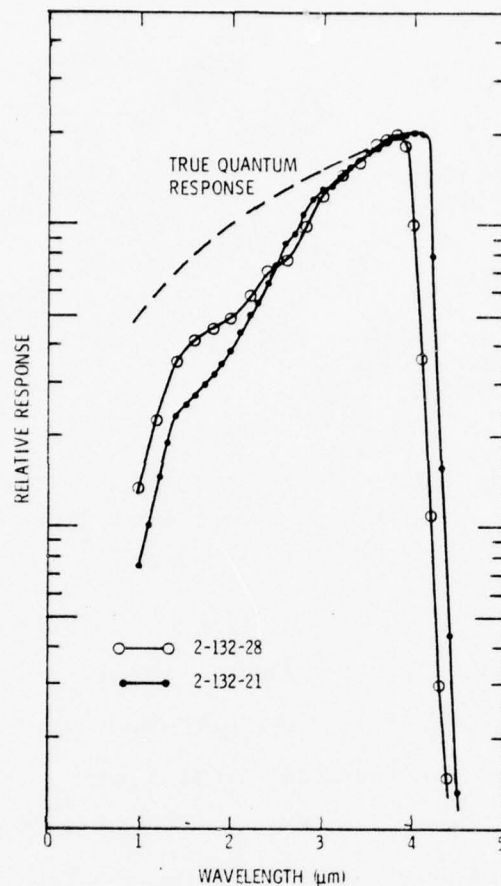


Figure 5-12. Relative Spectral Response for Two Typical Large Area PV HgCdTe Detectors

process, the hole lifetime may be extremely short with the result that these holes are not efficiently collected at the junction. Furthermore, a high surface recombination velocity at the front surface could also lead to poor hole collection and a reduction in the short-wavelength spectral sensitivity as exhibited in Figure 5-12.

Measurements of the uniformity of these large area detectors were also made using a fine spot contouring apparatus which is illustrated schematically in Figure 5-13. The radiation source for this measurement is an 800°K blackbody. Radiation emanating from the blackbody aperture is focused to a small spot by a diffraction limited optical system. The spot size can be as small as 0.001 inch in diameter. This small spot is focused

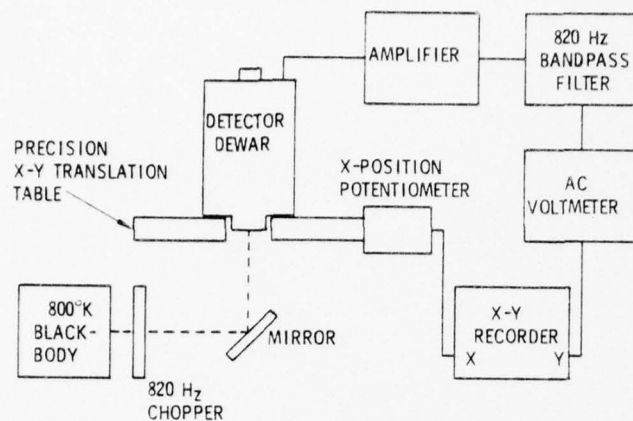


Figure 5-13. Block Diagram of Fine Spot Contouring Apparatus Used to Measure Sensitivity Profiles of Large Area PV HgCdTe Detectors

on the detector-dewar which sits on a precision X-Y translation table controlled by micrometer drive screws. These provide X-Y position control to a precision of ± 0.0001 inch. The blackbody radiation is chopped at a frequency of 820 Hz. This produces an ac signal in the detector which is amplified and read out on an ac voltmeter. The dc output from this meter is directed to the Y-input of an X-Y recorder. The X-input of this recorder is driven by a dc voltage taken from a potentiometer attached to the X-drive of the translation stage.

Figure 5-14 shows an example of the sensitivity profile of detector No. 2-132-21 measured with this apparatus. Each scan line is made with the fine spot moving across the detector in the X-direction with the Y-position held constant. The amplitude of the scan line represents the detector signal variation. Successive X-scans are made after moving the detector by 0.025-inch steps in the Y-direction. The eight scans shown map out essentially all the detector's sensitive area. The pronounced dip on the right-hand side of the scan profile is caused by the top metal electrode.

This particular detector was considered to be reasonably uniform. The fluctuations in signal amplitude are on the order of $\pm 12\%$. The fine structure in the sensitivity profile is a real signal change and not due to noise. Each profile may be reproduced in the same detail by repeated scans in either

direction. This fine structure is possibly related to crystal defects such as lineage described in Section 3.

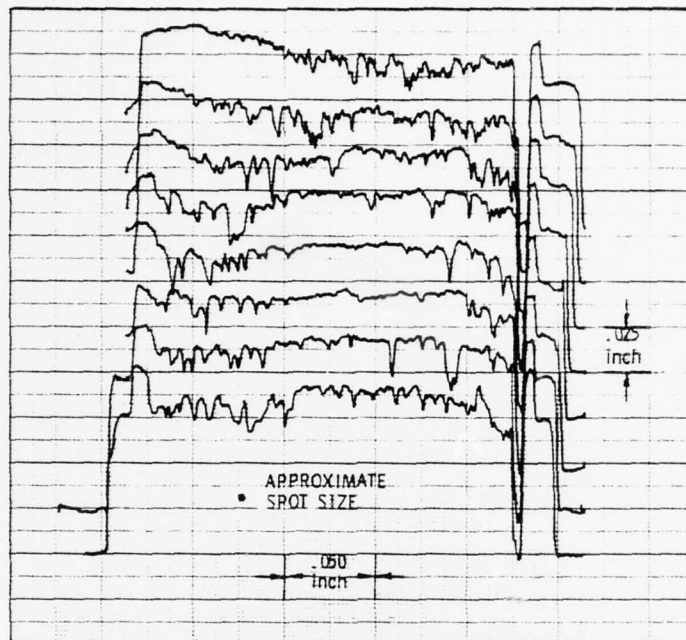


Figure 5-14. Fine Spot Sensitivity Profiles for Large Area PV HgCdTe Detector No. 2-132-21

Figure 5-15 shows another example of sensitivity profiles obtained from detector No. 2-132-19. This detector's profile was considered to be poor; consequently it was not used as part of a quadrant assembly. Variations in signal amplitude across this detector were as much as 100% with the sensitivity along one edge (the left-hand edge in Figure 5-15) being significantly higher than in the middle or the right-hand edge. No effort was expended to determine the cause of this non-uniformity.

After testing of this group of large area detectors, those with acceptable performance were selected for assembly into quadrant arrays. The method of assembly and packaging in a glass dewar is described in Section 6.

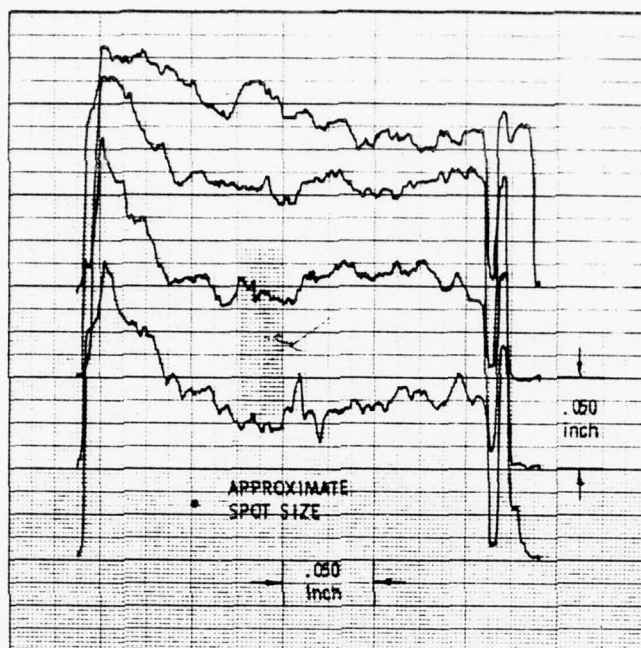


Figure 5-15. Fine Spot Sensitivity Profiles for Large Area PV HgCdTe Detector No. 2-132-19

Capacitance Versus Voltage Measurements

Measurements of diode capacitance versus reverse voltage were made for the purpose of diagnosing the junction characteristics. For an abrupt junction, the junction capacitance is given by ²⁶

$$C = A_j \left[\frac{\kappa_s \epsilon_0 e}{2(\phi_b + V_R)} \left(\frac{N_A N_D}{N_A + N_D} \right) \right]^{\frac{1}{2}} \quad (46)$$

The junctions made on this program were one-sided in that $N_D \gg N_A$. Therefore, Equation (46) becomes

$$C = A_j \left[\frac{\kappa_s \epsilon_0 e N_A}{2(\phi_b + V_R)} \right]^{\frac{1}{2}} \quad (47)$$

This equation can be rearranged to take the form

$$\frac{1}{C^2} = \frac{2(\phi_b + V_R)}{\kappa_s \epsilon_0 e N_A A_j^2} \quad (48)$$

²⁶ See Reference 6.

Thus, a plot of $1/C^2$ versus reverse voltage V_R should yield a straight line with slope

$$s = \frac{2}{\kappa_s \epsilon_0 e N_A A_j^2} \quad (49)$$

and y-intercept

$$y = \frac{2\phi_b}{\kappa_s \epsilon_0 e N_A A_j^2} \quad (50)$$

These two equations permit determination of N_A and ϕ_b values from experimental $1/C^2$ versus V_R data. In addition, the width of the depletion layer may be obtained from the equation

$$W = \frac{\kappa_s \epsilon_0 A_j}{C} \quad (51)$$

Figure 5-16 shows representative $1/C^2$ versus V_R plots obtained from B^+ ion-implanted diodes having different acceptor doping concentrations in the p-type base region. The straight lines obtained demonstrate that these are indeed abrupt junctions, and the analysis given above can be used to determine junction properties.

Table 5-7 lists the data obtained by C-V analysis at 77°K on 18 B^+ ion-implanted junctions. The capacitance measurements were made on a 100-kHz capacitance bridge (Boonton 74C-S8). All junctions were formed in $Hg_{1-x}Cd_xTe$ material with x value in the range 0.31-0.32. The dielectric constant κ_s was taken to be 16 for this composition.²⁷ The calculated built-in potential values are seen to range from 0.200 to 0.345 volt. These are in reasonable agreement with the energy band model discussed previously in Section 4. Values of the depletion layer width (at zero bias) were found to range from 0.13 to 1.1 μm . Base acceptor doping concentrations varied from 3.7×10^{14} to $2.6 \times 10^{16} \text{ cm}^{-3}$. The concentrations obtained from these C-V measurements were generally found to be a factor 2 to 5 lower than

²⁷ R. Dornhaus and G. Nimtz, "The Properties and Applications of the $Hg_{1-x}Cd_xTe$ Alloy System," Springer Tracts in Modern Physics, 78, Solid State Physics, Springer-Verlag, Berlin (1976) p. 93.

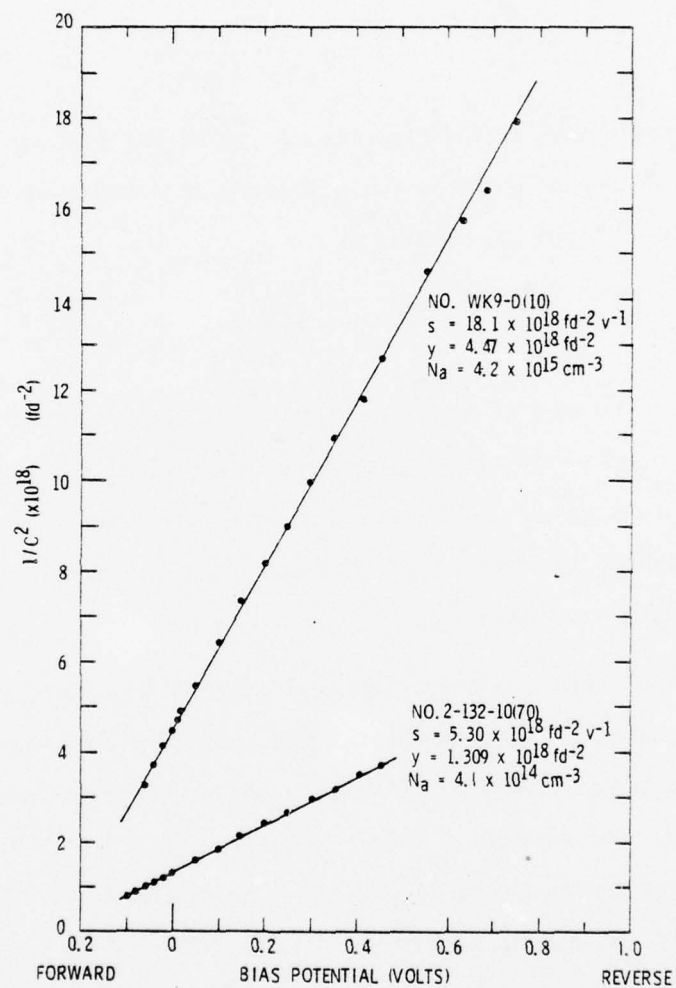


Figure 5-16. Representative $1/C^2$ versus V Curves for $\text{Hg}_{1-x}\text{Cd}_x\text{Te}$ Photodiodes. (x Value is 0.31-0.32 and Data were Taken at $77^\circ\text{K}.$)

Table 5-7. Data on 18 $\text{Hg}_{1-x}\text{Cd}_x\text{Te}$ Photodiodes
Analyzed by C-V Measurements

DIODE NUMBER	A(nom) (mm)	A _j (mm ²)	C ₀ (pf)	C ₀ /A _j (f/cm ²) (X 10 ⁻⁸)	Φ _B (volts)	W ₀ (μm)	N _A (cm ⁻³)	REMARKS
2-132-10 (70)	2 X 2	6.45	874	1.36	0.247	1.04	4.1 X 10 ¹⁴	LOW R ₀ , POOR NULL
2-132-10 (75)	2 X 2	6.45	909	1.41	0.219	1.02	3.8 X 10 ¹⁴	
2-132-15	5 X 5	31.2	3,923	1.26	0.266	1.13	3.7 X 10 ¹⁴	
2-132-94	5 X 5	31.2	4,930	1.58	-	-	-	
2-132-103	5 X 5	31.2	4,331	1.39	0.271	1.02	4.6 X 10 ¹⁴	
WK9-D (10)	1.3 DIA	1.08	473	4.4	0.247	0.32	4.2 X 10 ¹⁵	EARLY BREAKDOWN, POOR DATA AT REVERSE VOLTAGE
WK9-D-1	2 X 2	6.45	2,622	4.1	-	-	-	
WK9-D-2	2 X 2	6.45	2,548	4.0	-	-	-	
WK4-B7	1.3 DIA	1.13	998	8.83	0.146	0.13	1.6 X 10 ¹⁶	
WK4-B10	1.3 DIA	1.19	871	7.32	0.234	0.19	1.1 X 10 ¹⁶	
WK4-B19	1.3 DIA	1.24	973	7.84	0.212	0.18	1.1 X 10 ¹⁶	
WK4-B20	1.3 DIA	1.07	823	7.70	0.200	0.18	1.1 X 10 ¹⁶	
2-132-31 (5)	2 X 2	6.45	6,254	9.70	0.311	0.15	2.6 X 10 ¹⁶	
2-132-31 (6)	2 X 2	6.45	6,213	9.63	0.315	0.15	2.6 X 10 ¹⁶	
2-124-80 (2)	1 X 1	2.32	1,877	8.09	0.278	0.18	1.6 X 10 ¹⁶	
2-124-80 (3)	1 X 1	2.32	1,793	7.73	0.308	0.18	1.6 X 10 ¹⁶	
2-124-101 (M1)	1.3 DIA	0.93	797	8.57	0.321	0.17	2.1 X 10 ¹⁶	
2-124-101 (M2)	1.3 DIA	0.93	605	6.50	0.345	0.22	1.3 X 10 ¹⁶	

X = 0.31-0.32

T = 77°K

CAPACITANCE MEASURED AT 100 kHz

values obtained by Hall effect measurements before junction formation. The precise reason for this is not presently known. It may perhaps be due to compensation of base acceptors by the implanted donors in a narrow range near the p-n junction. This is the region that is analyzed in a C-V measurement.

Figure 5-17 shows a plot of capacitance per unit area versus base doping concentration which was constructed from the data in Table 5-7. The straight line drawn on this plot indicates that C_0/A_j is approximately proportional to N_A as indicated by Equation (47). Some deviations from the straight line occur because the built-in potential Φ_b is also a function of base doping as well as the ion-implantation doping on the n-side.

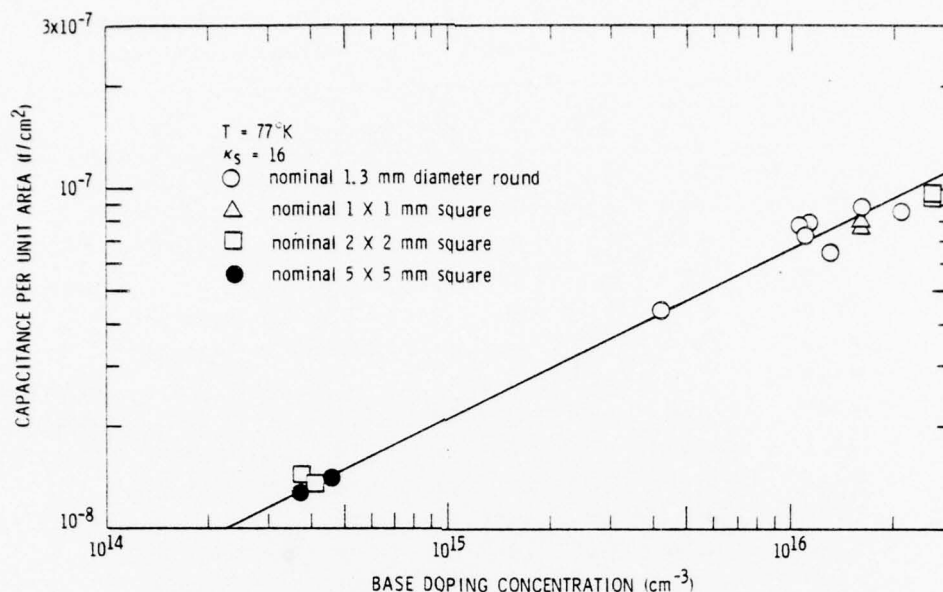


Figure 5-17. Zero Bias Capacitance versus Base Doping Concentration for 3.85- μm PV HgCdTe Detectors

The results of this capacitance versus voltage analysis demonstrate that the p-n junctions formed on this program are, indeed, one-sided step junctions. The expected reduction in junction capacitance is obtained by the use of low acceptor doping concentrations in the base region.

Laser Pulse Response Measurements

Laser pulse response measurements were made on selected HgCdTe photodiodes using the apparatus shown in block diagram form in Figure 5-18. The laser source was a GaAs diode emitting at a wavelength of 0.9 μm . It was driven by a Spencer Kennedy Labs 503A pulse generator. The laser

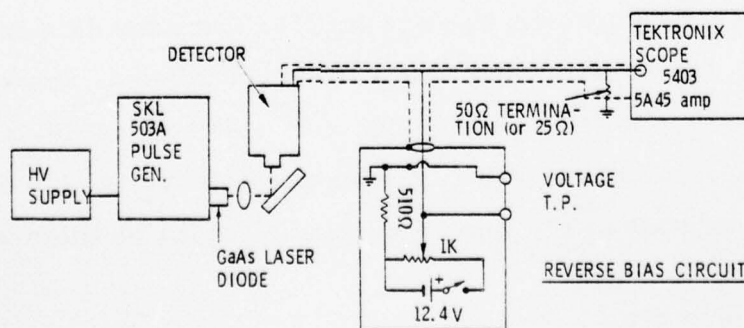


Figure 5-18. Circuit Used for τ Measurements with Reverse Bias

output pulse was 100 nsec in duration and had rise and fall times on the order of 1 nsec. Maximum pulse peak power could be as high as 1 watt at a repetition rate of 20 pulses per sec.

The detector signal output was observed on a Tektronix 5403 oscilloscope equipped with a 5A45 amplifier. This system had a 0-60 MHz frequency response. Most of the measurements were made with the detector output plugged directly into the scope amplifier with either a 50- or 25-ohm termination at the scope input. Some measurements were made with the SBRC A231 preamplifier inserted between the detector and scope. This preamplifier has a basic 18 MHz bandwidth, which should allow observation of response times down to about 10 nsec. A reverse biasing circuit was also attached to the detector cable to permit observation of pulse response with increasing reverse bias.

Figure 5-19 illustrates how the pulse shapes are analyzed. The time base moves from right to left. When the laser pulse turns on, the detector signal output starts to rise. One hundred nsec later, the laser pulse turns off. However, the pulse has not been on long enough for the detector response to rise up to its maximum level. When the laser pulse turns off, the detector

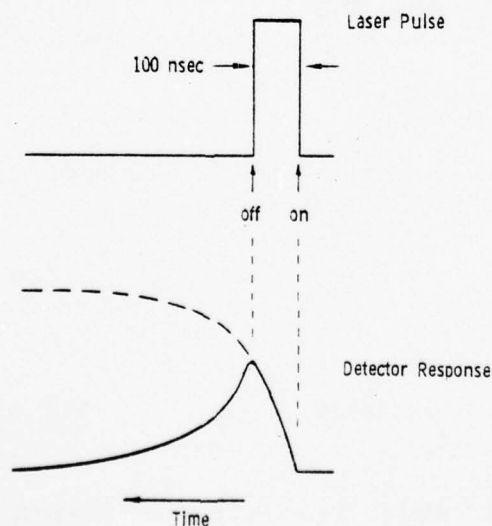
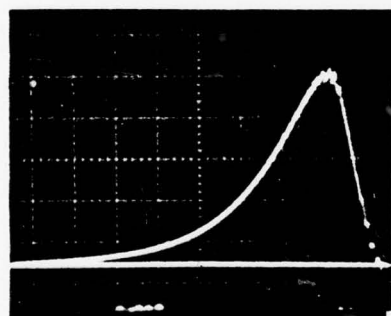


Figure 5-19. Illustration of Method of Analysis of Detector Pulse Response Data

response then begins to decay. Since the laser pulse stays off for a long time before the next pulse begins, there is now sufficient time for the detector signal to decay to zero. Therefore, detector response time information can be obtained only from the decay portion of the oscilloscope trace. We use the conventional definition of detector response time which is the measured time interval required for the detector's response to decay from its peak value to $1/e$ (or 37%) of the peak value.

Figure 5-20 shows the response of a nominal $5 \times 5 \text{ mm}^2$ detector (No. 2-132-15) measured with the detector output fed directly into the scope and using either a 50- or 25-ohm termination. A reduction in response time of roughly a factor of 2 is observed with the smaller termination resistance. This implies that the detector is RC limited. In the circuit of Figure 5-18, R is effectively the termination resistance, and C the detector junction



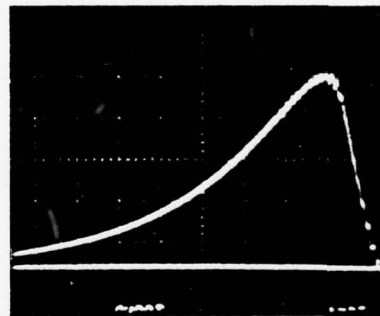
100 nsec/division

(a) Detector Pulse Response with a 25-ohm Termination

$$\tau \approx 200 \text{ nsec}$$

$$C = 4,000 \text{ pf}$$

$$RC = 100 \text{ nsec (calculated)}$$



100 nsec/division

(b) Detector Pulse Response with a 50-ohm Termination

$$\tau \approx 340 \text{ nsec}$$

$$C = 4,000 \text{ pf}$$

$$RC = 200 \text{ nsec (calculated)}$$

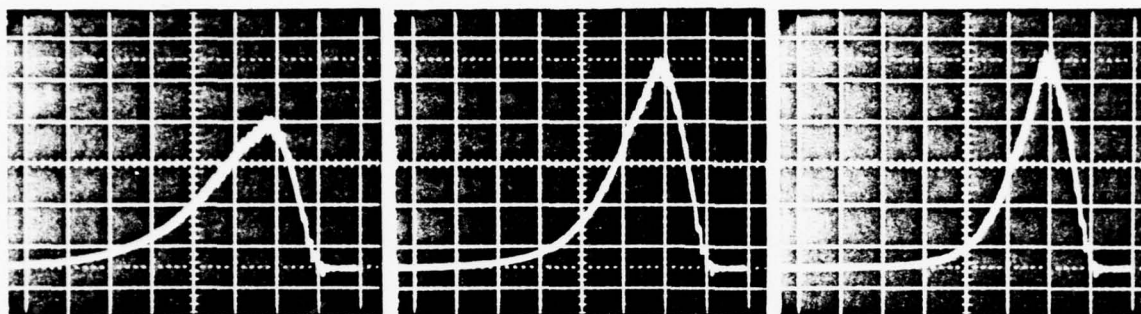
Figure 5-20. Pulse Response Measurements of PV HgCdTe Detector No. 2-132-15. Nominal Detector Area is $5 \times 5 \text{ mm}^2$; λ_p is $3.8 \text{ }\mu\text{m}$; Operating Temperature was 77°K

capacitance plus any stray capacitance to ground in the cables. However, if one uses the measured capacitance data for this detector, namely, 3923 pf for junction capacitance, 50 pf for cable capacitance, and 20 pf for scope input capacitance, the calculated RC values turn out to be about 50% of the measured response time. These calculated values are indicated on Figure 5-20. The reason for this is not known.

Figure 5-21 shows the effect of increasing reverse bias on this same detector. It was found that, as reverse bias was increased from 0 to 0.7 volt, the response time decreased from 210 to 70 nsec. A 25-ohm termination was used in these measurements.

Figure 5-22 shows pulse response data on a nominal $2 \times 2 \text{ mm}^2$ detector (No. 2-132-10). Parts (a) and (b) show the effect of reverse bias voltage. An increase from 0 to 0.5 volt decreased the response time from 50 to 25 nsec. Parts (c) and (d) show zero-bias response curves taken with direct scope input using a 25-ohm termination compared to using the SBRC A231 preamplifier before the scope. Since the response time is a little faster with the SBRC preamplifier, this implies that the effective input impedance of the preamplifier is less than 25 ohms. In fact, the design input impedance is 20 ohms and this is verified by the measured data.

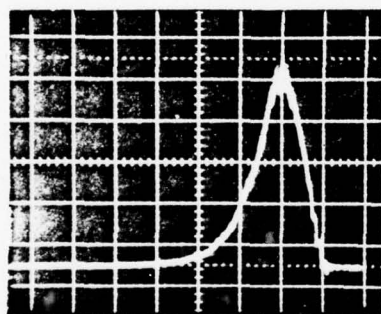
More data on the comparison of measured detector pulse response times with calculated RC times was collected on smaller area detectors. Figure 5-23 shows plots of measured response time versus reverse bias for one nominal $2 \times 2 \text{ mm}^2$ detector and one $1 \times 1 \text{ mm}^2$ detector. The data points represent measured response times with error bars indicating the estimated error in reading the $1/e$ point from the scope trace. The solid lines are calculated RC values based on measured capacitance versus reverse voltage measurements. Again it is seen that the calculated RC values are about one-half of the actual measured response times, a result that is similar to the case of the $5 \times 5 \text{ mm}^2$ detector previously described.



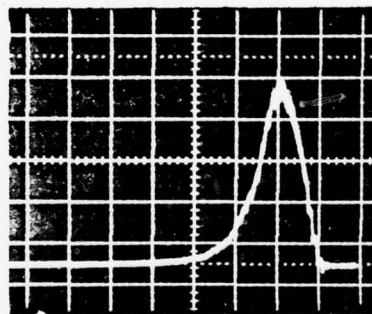
(a) $V_R = 0$ volt
 $\tau = 210$ nsec

(b) $V_R = 0.2$ volt
 $\tau = 150$ nsec

(c) $V_R = 0.35$ volt
 $\tau = 110$ nsec

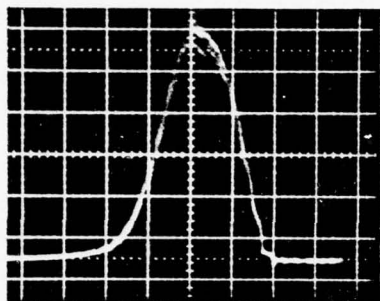


(d) $V_R = 0.5$ volt
 $\tau = 80$ nsec

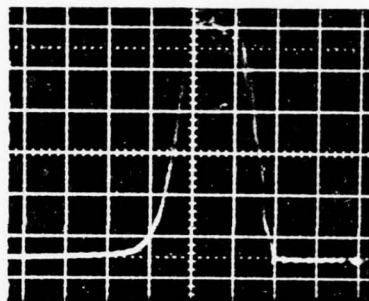


(e) $V_R = 0.7$ volt
 $\tau = 70$ nsec

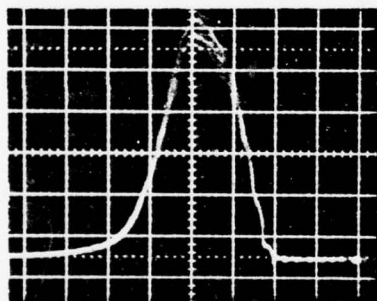
Figure 5-21. Pulse Response Curves on Detector No. 2-132-15 showing the Decrease in Response Time with Increasing Reverse Bias. $T = 77^\circ\text{K}$, Time Base is Right to Left at 100 nsec/division, Load Resistor Termination was 25 ohms.



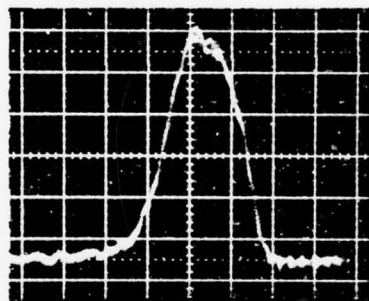
(a) $V_R = 0$ volt
 $\tau = 50$ nsec



(b) $V_R = 0.5$ volt
 $\tau = 25$ nsec



(c) $V_R = 0$ volt
 $\tau = 50$ nsec



(d) $V_R = 0$ volt
 $\tau = 40$ nsec

SBRC A231 Preamplifier

Figure 5-22. Pulse Response Curves for a Nominal 2×2 mm² Detector, No. 2-132-10. $T = 77^\circ\text{K}$, Time Base is Right to Left at 50 nsec/division, Load Resistor Termination is 25 ohms (except for (d), which was obtained using the SBRC A231 Current Mode Preamplifier).

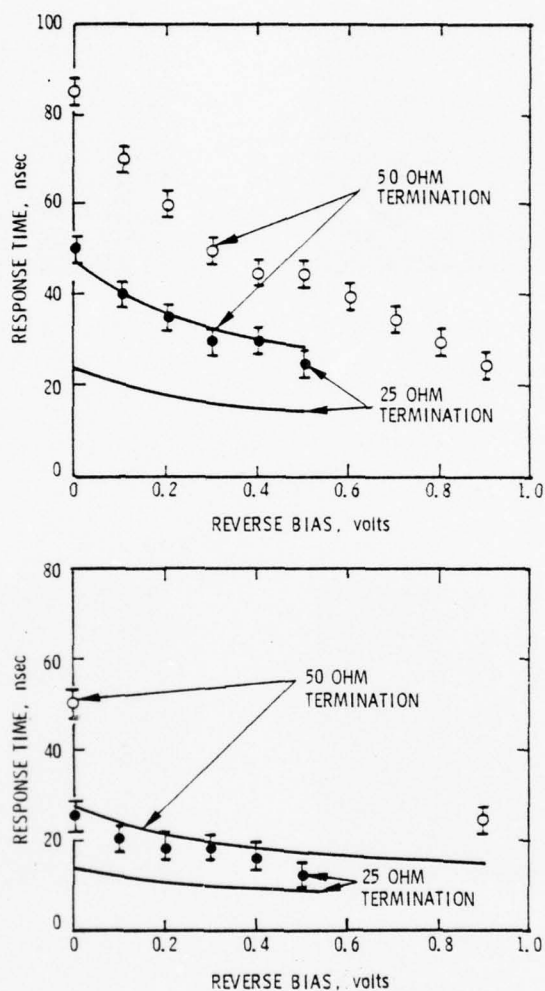


Figure 5-23. Comparison of Measured Detector Response Times (Data Points) with Calculated RC Times (Solid Lines). A) Detector 2-132-10-70, $A_j = 5.40 \text{ mm}^2$; B) Detector WK9-D10, $A_j = 1.08 \text{ mm}^2$. Operating Temperature was 77°K .

As previously mentioned, an explanation for this result is not presently available. However, the data acquired seem to indicate that it is related to junction capacitance. The following comments summarize the observed results.

1. Calculated RC times are always less than measured response times by about a factor of one-half.
2. The effect is independent of detector area. Decreasing A_j decreases C_j and response time proportionately.
3. Decreasing R decreases the response time proportionately.
4. The effect is independent of laser light intensity with the laser radiation utilized, i. e., GaAs at 0.9 μm .

A possible hypothesis which can be offered is that the effect is related to deep states within the forbidden band which are activated by the laser light but not by the C-V measurement. Activation of these states would create additional charge within the junction depletion region thereby effectively increasing junction capacitance. Means to investigate this possibility might include: measurements of capacitance and pulse response time versus temperature, measurements of small-signal capacitance with different intensities and/or different wavelengths of light on the junction,²⁸ and deep level transient spectroscopy (DLTS).²⁹ Measurements such as these would require a significant additional effort which was felt to be beyond the intended scope of this program and were, therefore, not attempted. Furthermore, the pulse response times achieved for $5 \times 5 \text{ mm}^2$ detectors were adequate for the intended application. A detailed investigation of this problem would be more appropriate for some future program.

²⁸ A. M. White, P. Porteous and P. J. Dean, J. Electronic Material, 5, 91, (1976).

²⁹ D. V. Lang, J. Appl. Phys. 45, 3023 (1974).

2.06 μm PV HgCdTe DETECTORS

Summary of Detector Properties

Detectors for operation at 2.06 μm were made from two different ingots. One (No. RC4) was produced by the SSR method, the other (No. 2-138) was produced by the zone melting method. Table 5-8 summarizes the test data acquired on a number of 2.06 μm PV HgCdTe detectors which were fabricated on this program.

Table 5-8. Summary of Properties of 2.06 μm PV HgCdTe Detectors

DIODE NUMBER	T ($^{\circ}\text{K}$)	A_d (mm^2)	A_j (mm^2)	R_0 (ohms)	$R_0 A_j$ (ohm cm^2)	C_0 (pf)	C_0/A_j (pf/ mm^2)	$1/\lambda_D$ (a/w)	η (AT λ_D)	$D^*(\lambda_D, 2\text{kHz})$ ($\text{cm}^2 \text{Hz}^{1/2}/\text{w}$)	λ_D (μm)	λ_C (μm)
2-138-3B-1	77	5.40	6.45	3.3×10^4	2.1×10^3	-	-	1.72	0.89	4.5×10^{11}	2.4	2.5
2-138-3B-2	77	5.40	6.45	9.0×10^4	4.9×10^3	-	-	1.45	0.75	8.5×10^{11}	2.4	2.5
RC4-3E-14	77	2.06	2.32	1.3×10^5	3.0×10^3	1,435	620	1.02	0.60	5.5×10^{11}	2.1	2.2
RC4-3E-14	192	2.06	2.32	1.3×10^3	2.9×10^1	1,635	705	0.98	0.60	0.4×10^{11}	2.1	2.2
RC4-2B	77	5.40	6.45	7.8×10^4	5.0×10^3	3,052	565	0.93	0.53	7.0×10^{11}	2.2	2.3
RC4-2B	192	5.40	6.45	3.3×10^3	2.1×10^2	-	-	-	-	-	-	-
RC4-2K-L	77	5.40	6.45	2.3×10^4	1.5×10^3	-	-	0.97	0.55	2.7×10^{11}	2.1	2.3
RC4-2K-L	192	5.40	6.45	1.2×10^4	7.7×10^2	3,516	651	1.22	0.69	1.9×10^{11}	2.2	2.3
RC4-2K-R	77	5.40	6.45	2.4×10^4	1.5×10^3	-	-	0.97	0.55	2.4×10^{11}	2.1	2.3
RC4-2K-R	192	5.40	6.45	3.6×10^3	2.3×10^2	4,638	761	1.22	0.69	0.9×10^{11}	2.2	2.3
RC4-4E-L	77	5.40	6.45	1.0×10^5	6.5×10^3	-	-	1.72	1.02	7.0×10^{11}	2.1	2.2
RC4-4E-L	192	5.40	6.45	3.0×10^3	1.9×10^2	-	-	1.57	0.93	1.1×10^{11}	2.1	2.2
RC4-4E-R	77	5.40	6.45	4.5×10^4	2.9×10^3	3,400	630	1.98	1.17	2.9×10^{11}	2.1	2.2
RC4-4E-R	192	5.40	6.45	1.3×10^4	8.1×10^2	4,001	741	1.65	0.98	1.1×10^{11}	2.1	2.2
RC4-5J-L	77	5.40	6.45	6.5×10^4	4.2×10^3	-	-	1.34	0.79	6.2×10^{11}	2.1	2.2
RC4-5J-L	192	5.40	6.45	3.3×10^3	2.1×10^2	2,215	411	1.30	0.77	1.1×10^{11}	2.1	2.2
RC4-5J-R	77	5.40	6.45	8.8×10^5	5.7×10^4	2,459	455	1.10	0.65	6.3×10^{11}	2.1	2.2
RC4-5J-R	192	5.40	6.45	3.0×10^4	1.9×10^3	2,465	457	1.20	0.71	3.1×10^{11}	2.1	2.2
AVERAGE VALUE								(1.31)	(0.76)			

FOV $\approx 180^{\circ}$

All but one of these detectors were nominal $2 \times 2 \text{ mm}^2$ devices (actual sensitive area of 5.40 mm^2). The remaining one was a nominal $1 \times 1 \text{ mm}^2$ device (actual sensitive area of 2.06 mm^2). Measurements were made at both 77° and 192°K . At 77°K , the zero bias dynamic resistance (R_0) values for these detectors were in the 10^4 to 10^5 ohm range, and $R_0 A_j$ values ranged between 1.5×10^3 and 5.7×10^4 ohm cm^2 . At 192°K , R_0 values

AD-A067 306

SANTA BARBARA RESEARCH CENTER GOLETA CALIF
DEVELOPMENT OF LARGE AREA PV HgCdTE DETECTORS FOR 2.06 AND 3.85--ETC(U)
MAY 78 P R BRATT

DAAB07-76-C-0803

F/G 17/5

NL

UNCLASSIFIED

2 OF 2

AD
A067306



END
DATE
FILMED
6-79
DDC

decreased to somewhere between 0.5 to 0.01 of the 77°K values and the R_0A_j products ranged between 2.9×10^1 and 1.9×10^3 ohm cm^2 . The 192°K measured R_0A_j values are in reasonable agreement with theoretical estimates based on a saturation current density dominated by g-r current. The 77°K measured R_0A_j values are much lower than calculated from theory. This implies that the 77°K R_0A_j values are limited by leakage current. This leakage current could be due to bulk material imperfections crossing the plane of the p-n junction (e. g., edge dislocations or point imperfections), or surface leakage around the junction periphery where it comes to the surface of the HgCdTe. No attempts were made during the course of this program to determine which mechanism predominates.

The measured capacitance data on several of these 2.06 μm detectors is also shown in Table 5-8. The capacitance per unit area at zero bias ranged between 411 and 761 pf/mm^2 . There was little change in capacitance between 77° and 192°K. These capacitance per unit area values imply a base doping concentration in the 10^{16}cm^{-3} range. Most of the material used for these detectors was gold-diffused under the same conditions that were used for 3.85- μm detectors which gave base doping concentrations of about 10^{15}cm^{-3} . A possible explanation for this difference is as follows. After gold diffusion, a thin Au-HgCdTe alloy layer is left on the wafer surface and must be removed by polishing and etching operations. Underneath this alloy layer is the layer of Au-doped HgCdTe which has the desired low acceptor concentration. In the case of 3.85- μm material, this layer may be 0.004 to 0.005 inch thick, whereas in the case of 2.06- μm material, this layer may be only 0.001 to 0.002 inch thick. Thus, the polishing operation could have removed the desired low-doped region on the 2.06- μm material. This exposed a more heavily p-type region (due to Hg vacancies) in the wafer interior. A revised wafer annealing procedure would have to be developed to achieve the very low base doping concentrations required for a significant reduction in junction capacitance. Methods for doing this are known, but there was insufficient time to try them during the course of the present program.

Table 5-8 also includes the measured detector properties of these photodiodes such as current responsivity, quantum efficiency and detectivity. The current responsivity averaged 1.2 a/w and the quantum efficiency averaged 76%. It may be noted that quantum efficiencies on two detectors exceeded 100%. This is attributed to experimental error. The quantum efficiency values were obtained from photocurrent measurements with a 500°K blackbody source. The conversion factor used to change 500°K blackbody photocurrent to peak photocurrent at 2.1 μm is a rather large number on the order of 10^3 and subject to a substantial error depending on how accurate the detector's spectral response curve is known. Nevertheless, it is believed that the averaged data are reasonably accurate and it can be concluded that these detectors are exhibiting very good quantum efficiencies.

The detectivity values shown in Table 5-8 range between 2.4 to 8.5×10^{11} $\text{cm Hz}^{\frac{1}{2}}/\text{watt}$ for 77°K operation and 0.4 to 3.1×10^{11} $\text{cm Hz}^{\frac{1}{2}}/\text{watt}$ for 192°K operation. The detectivity of these detectors is not background limited because the photon flux from a 300°K background in the spectral interval below 2.2 μm is not great enough to produce a significant photon noise current. Thus the noise current may be dominated by contributions from the detector's thermal noise, the feedback resistor thermal noise or the amplifier noise. In the case where detectivity is limited by detector thermal noise, the equation for D^* is

$$D^*(\lambda) = \frac{\eta e \lambda}{hc} \left[\frac{R_o A_j}{4 kT} \left(\frac{A_d}{A_j} \right) \right]^{\frac{1}{2}}$$

Assuming the following typical values for 77°K operation,

$$\eta = 0.76$$

$$\lambda_p = 2.1 \mu\text{m}$$

$$R_o A_j = 3 \times 10^3 \text{ ohm cm}^3$$

$$A_d/A_j = 5.40/6.45 = 0.837$$

we obtain

$$D^*(\lambda_p) = 9.8 \times 10^{11} \text{ cm Hz}^{\frac{1}{2}}/\text{watt}$$

Although one detector approaches this $D^*(\lambda_p)$ value, most are significantly below it. It is concluded that other noise sources are contributing to reduce the 77°K $D^*(\lambda_p)$ below the expected detector thermal noise limited value.

For 192°K operation, the same values above are assumed with the exception that $R_0A_j = 3 \times 10^2 \text{ ohm cm}^3$. In this case, we obtain

$$D^*(\lambda_p) = 2.0 \times 10^{11} \text{ cm Hz}^{\frac{1}{2}}/\text{watt}$$

Two detectors approach or exceed this value, but they had much larger R_0A_j values. The others are significantly lower in $D^*(\lambda_p)$. In these cases, it must again be concluded that other noise sources are contributing to reduce the 192°K $D^*(\lambda_p)$ below the detector thermal noise limited value.

The background limited $D^*(\lambda_p)$ value for these detectors was calculated to be $3.3 \times 10^{12} \text{ cm Hz}^{\frac{1}{2}}/\text{watt}$ assuming $\eta = 0.76$, $\lambda_p = 2.1 \text{ } \mu\text{m}$ and $Q_B = 4 \times 10^{12} \text{ ph/sec/cm}^2$. To achieve this $D^*(\lambda_p)$ value, detectors would have to be made with much larger R_0A_j values, on the order of 10^5 ohm cm^2 . This may be possible for 77°K operation if the sources of leakage current are identified and greatly reduced. For 192°K operation, the R_0A_j values will probably be limited by g-r current and this will prohibit the attainment of BLIP operation at this temperature.

Spectral Response

The last columns of Table 5-8 list the wavelengths of peak spectral response and cutoff. Detectors made from crystal 2-138 peaked at $2.4 \text{ } \mu\text{m}$, while those made from RC4 peaked at 2.1 to $2.2 \text{ } \mu\text{m}$. Figure 5-24 shows the measured spectral response for detector No. 2-138-3B-2 at 77°K. Notice the very sharp cutoff wavelength (one-half of peak response) at $2.52 \text{ } \mu\text{m}$ and a peak response at $2.40 \text{ } \mu\text{m}$. Also to be noticed is the significant departure from true quantum response on the short-wavelength side. The reasons for this have already been described in the previous discussion of the spectral response for $3.85\text{-}\mu\text{m}$ detectors.

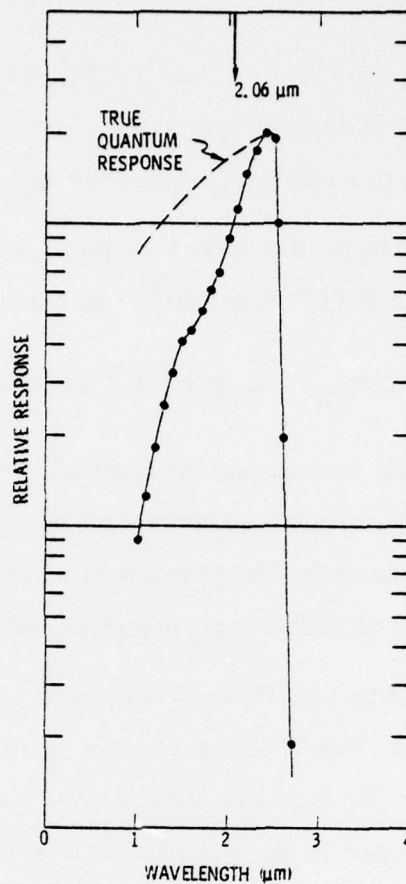


Figure 5-24. Relative Spectral Response at 77°K for Detector No. 2-138-3B-2

Figure 5-25 shows the spectral response for detector No. RC4-2B measured at 77° and 192°K. The peak response of this detector is at 2.1 μm, much closer to the desired 2.06-μm wavelength than the 2-138 material. The shift in cutoff wavelength with changing temperature is very small for this alloy composition. Our measured data indicated cutoffs of 2.30 μm at 77°K and 2.27 μm at 192°K, a shift of only 0.03 μm. Since the experimental error in the measurements is on this same order, it is difficult to obtain a precise value for the temperature coefficient of the energy bandgap from this data.

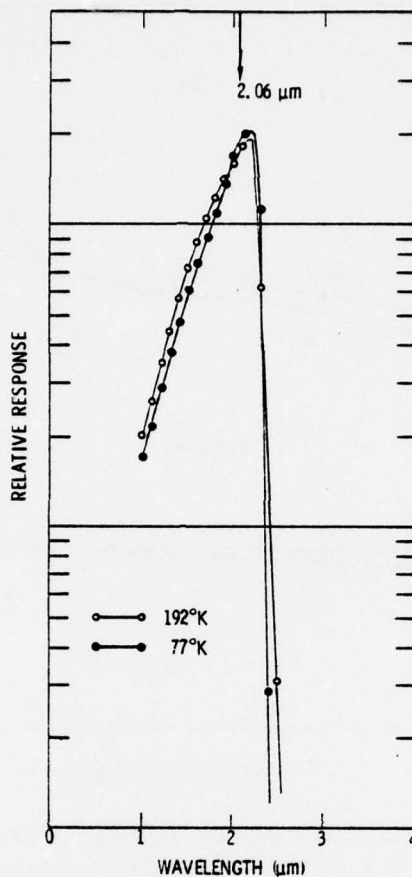


Figure 5-25. Relative Spectral Response at 192°K and 77°K for Detector No. RC4-2B

Current-Voltage Characteristics

Figure 5-26 shows representative current-voltage curves for two nominal $2 \times 2 \text{ mm}^2$ detectors at temperatures of 77° and 192°K. The R_0 and $R_0 A_j$ values for these detectors were listed in Table 5-8. The reverse bias curves are seen to be somewhat better for detector No. RC4-4E-R than for No. RC4-4E-L. The short-circuit photocurrent for these detectors is quite small, on the order of 30 na and cannot be distinguished with the current scale used here. Both of these detectors showed somewhat higher series resistance than might be expected. RC4-4E-R was 50 ohms and RC4-4E-L was 68 ohms. The series resistance is about the same at 77° and 192°K. According to the detector-preamplifier analysis presented in Section 2, such a high series resistance could cause some reduction in detectivity at frequencies in the MHz range. The cause of the high series resistance is thought to

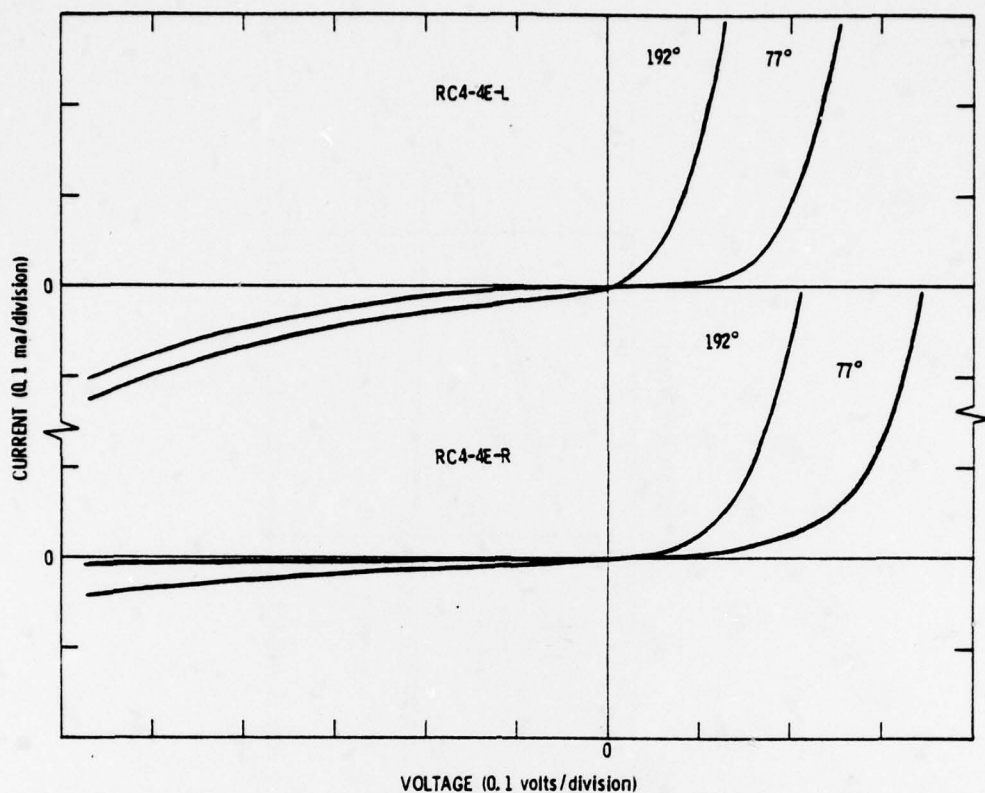


Figure 5-26. Current versus Voltage Curves for Two Nominal $2 \times 2 \text{ mm}^2$ PV HgCdTe Detectors for $2.06 \mu\text{m}$ Operation

be at the contacts to either the p- or n-type side of the junction rather than in the diode itself. Development of better metallization techniques should eliminate this problem.

Response Times

The response time of $2.06\text{-}\mu\text{m}$ detectors was measured utilizing the GaAs laser diode pulse method previously described. Measured response times for nominal $2 \times 2 \text{ mm}^2$ detectors were in the range 200 to 400 nsec and appeared to be limited by junction capacitance.

One detector, No. RC4-5J-R, showed much longer response times in the vicinity of 1,000 nsec which did not correlate with junction capacitance. The measured response time of this detector also showed a large variation depending on where the spot of laser light struck the detector surface. No explanation for this behavior was discovered. Since this was only observed

on one detector, it was assumed to be an anomaly and was dismissed from further consideration.

Measurements of response time were found to decrease with reverse bias as expected from a reduction of junction capacitance. Figure 5-27 shows data taken on detector No. RC4-4E-R at two temperatures, 77° and 192°K.

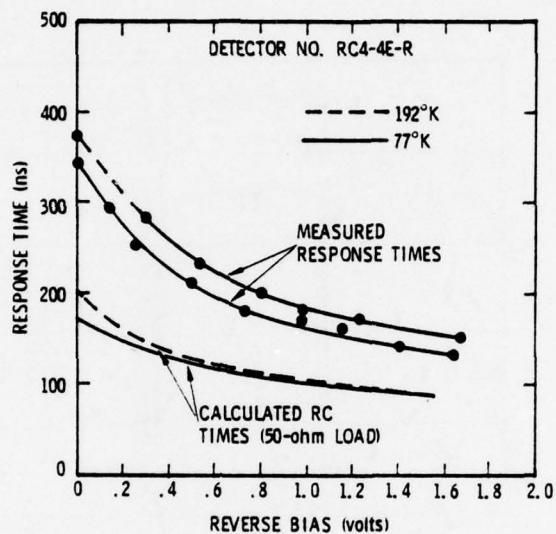


Figure 5-27. Measured and Calculated Response Times versus Reverse Bias Voltage for a 2.06- μ m PV HgCdTe Detector

The response times are only slightly different for these two temperatures and decrease from about 350 nsec at zero bias to about 140 nsec at 1.6 volts reverse bias. Also shown in this figure are calculated RC times based on measured capacitance data for this detector and a 50-ohm termination at the scope input. The calculated RC times are seen to be roughly a factor of two lower than the measured response times just as in the case of the 3.85- μ m detectors discussed previously.

Sensitivity Profiles

The sensitivity profiles of nominal $2 \times 2 \text{ mm}^2$ 2.06- μm detectors were generally found to be quite uniform. Figure 5-28 shows representative data for detector No. RC4-2B at 77°K. The worst variations are seen to be no greater than $\pm 6\%$. The large dip on the right-hand side is due to obscuration by the top electrode.

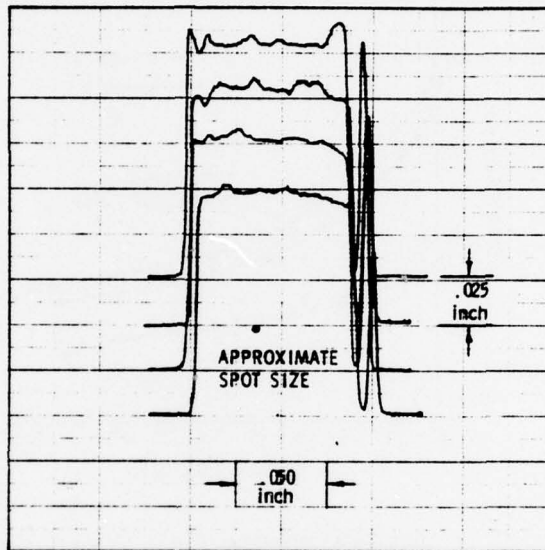


Figure 5-28. Fine Spot Sensitivity Profiles for a $2 \times 2 \text{ mm}^2$ 2.06- μm PV HgCdTe Detector (No. RC4-2B)

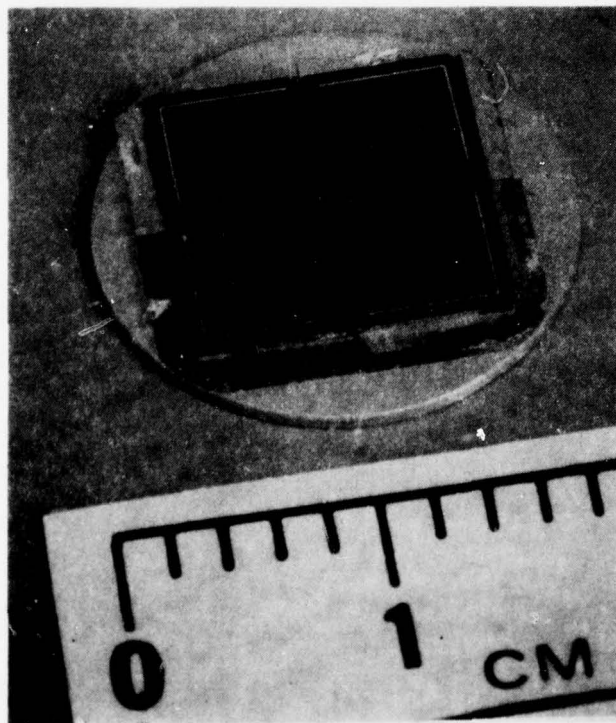
Section 6

ASSEMBLY OF QUADRANT ARRAYS

DETECTOR ASSEMBLY

The large area ($5 \times 5 \text{ mm}^2$) detectors for $3.85 \mu\text{m}$ were assembled into quadrant arrays. The detectors for $2.06 \mu\text{m}$ were not assembled into quadrant arrays, but were delivered as single elements. However, the techniques developed for the $3.85\text{-}\mu\text{m}$ quadrant arrays are also applicable to the $2.06\text{-}\mu\text{m}$ material and it is believed that, should the need arise, large area $2.06\text{-}\mu\text{m}$ quadrants can also be made.

After pretesting of the individual $5 \times 5 \text{ mm}^2$ elements, four are chosen for assembly into a quadrant array as shown in Figure 6-1. The four individual elements, each on its own substrate, are butted together and cemented



77-2-36

Figure 6-1. Photograph of $3.85\text{-}\mu\text{m}$ Large Area Quadrant Array Assembled from Four $5 \times 5 \text{ mm}^2$ Elements

down to another substrate. In the case of quadrant arrays delivered in glass dewars, this other substrate was the metal end of the dewar inner cold finger. There is inevitably some dead space between the four elements of the array. In the present design, this amounts to 0.7 mm.

Figure 6-2 shows a drawing of the glass dewar, which was used to house the quadrant detectors. The dewar is permanently evacuated and sealed off. A getter is used to maintain high vacuum over long periods of time. The dewar has a sapphire window to admit the infrared radiation to the detector array. Cooling of the detector to approximately 80°K is obtained by a Joule-Thomson expanding gas cryostat which operates on high-pressure nitrogen gas. The glass dewar is protected from breakage by an aluminum metal housing. The housing is made in two sections which screw together and clamp onto the dewar flange to retain it. A foam material is placed between the glass dewar wall and the metal housing for cushioning against shock and for thermal insulation. For this exploratory development model, the foam material is removable, and the glass vacuum dewar can be

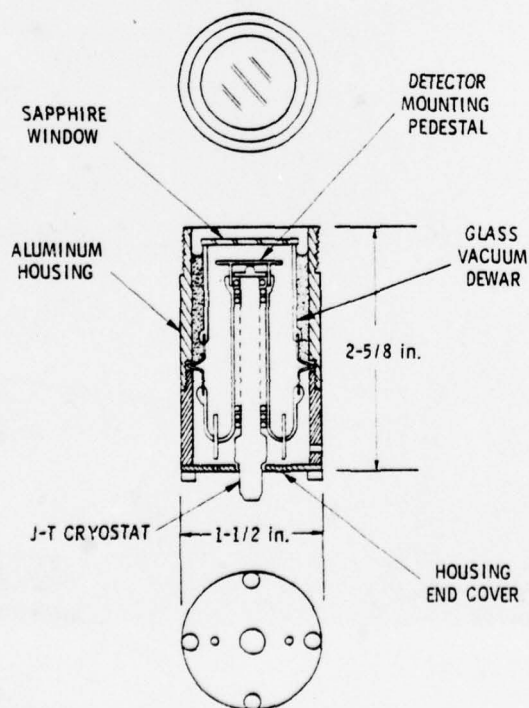


Figure 6-2. Large Area PV HgCdTe Detector Dewar Assembly

easily removed from the metal housing. In a production model, the foam would form a permanent seal and the glass vacuum dewar would not be removable. The housing serves the additional function of providing electrostatic shielding for the detector array. An end cover to the metal housing provides protection for the electrical connections to the glass vacuum dewar and also serves to prevent the J-T cryostat from slipping out of the dewar. This cover is held in place by four socket head screws.

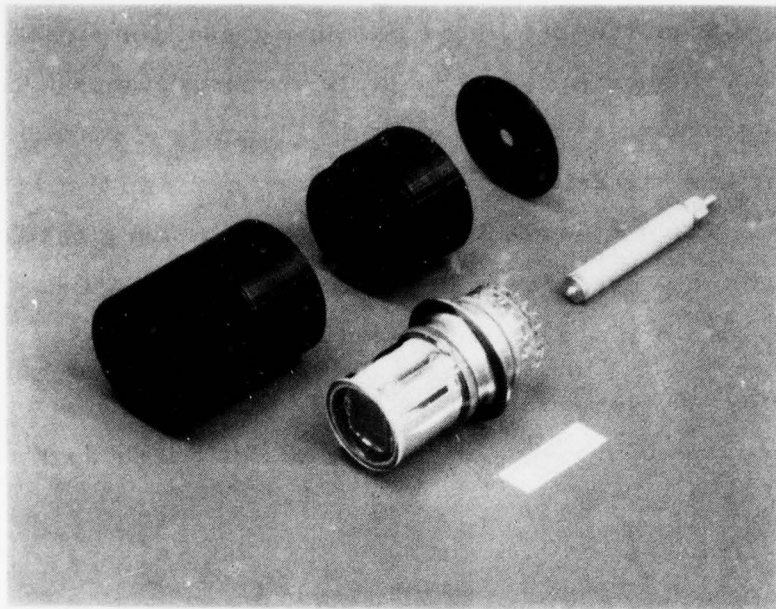
Figure 6-3 shows an exploded view of the detector assembly. Figure 6-4 shows an assembled view with the four cables attached which lead to the preamplifier.

PREAMPLIFIER

A four-channel preamplifier was fabricated using a proven low-noise circuit design (Model A231), which had been previously developed by SBRC for use with photovoltaic type infrared detectors. The basic design, shown in Figure 6-5, consists of a current-mode preamplifier stage followed by a voltage-mode post-amplifier.

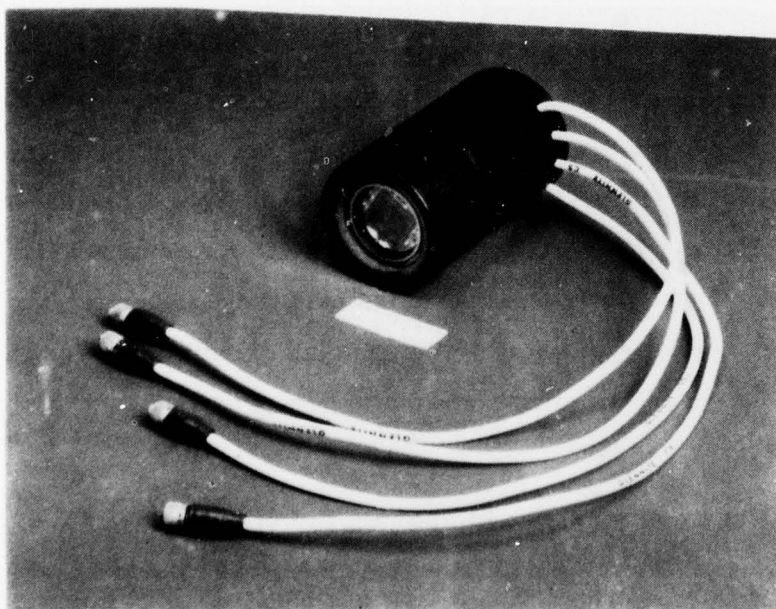
The voltage gain of the current-mode stage is essentially unity; the gain of the voltage-mode stage is 10 when the output is terminated in a 50-ohm load, or 20 if unterminated. The output signal is negative-going; that is, a radiation pulse hitting the PV HgCdTe detector produces a negative output voltage pulse from the amplifier. The output saturates at about -0.4 volt when terminated into 50 ohms or at -1 volt if unterminated. Four independent, identical amplifier channels are provided; one for each quadrant of the detector array.

The power requirements to operate the amplifier (all four channels) are +15 volts at 190 ma. Built-in voltage sources provide a suitable reverse bias on each detector of the quadrant array to optimize its speed of response and detectivity. This reverse bias is fixed by insertion of a suitable resistor in a voltage dividing network and is not easily changed in the field.



77-7-51

Figure 6-3. Exploded View Showing the Various Parts of the Detector Assembly for the 3.85- μm Quadrant Array



77-7-46

Figure 6-4. Assembled View of Large Area PV HgCdTe Detector Assembly for 3.85 μm

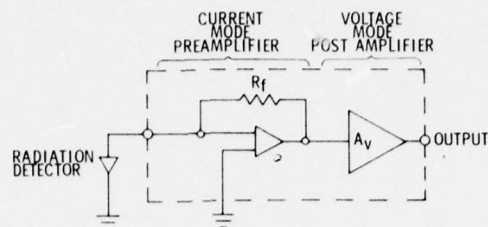
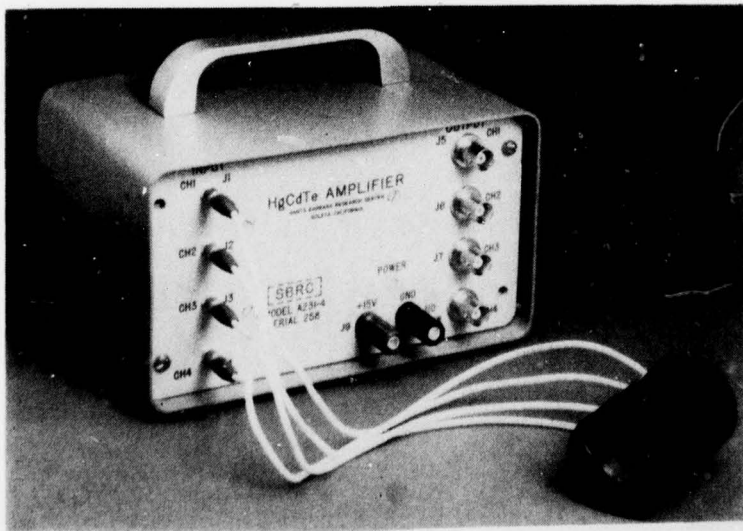


Figure 6-5. Block Diagram of PV HgCdTe Detector-Preamplifier Circuit

Table 6-1 summarizes the amplifier characteristics; Figure 6-6 shows a photograph of the amplifier with the PV HgCdTe detector quadrant array connected to it.

Table 6-1. Specifications for PV HgCdTe Preamplifier, Model A231-4

FEEDBACK RESISTANCE:	$R_f = 1.0 \text{ kohm}$
POST-AMPLIFIER VOLTAGE GAIN:	$A_v = 10 \text{ INTO A } 50\text{-ohm LOAD,}$ $= 20 \text{ UNTERMINATED}$
MAXIMUM OUTPUT:	$v_o = -0.4 \text{ volt PEAK INTO A } 50\text{-ohm LOAD}$ $= -1.0 \text{ volt PEAK UNTERMINATED}$
OUTPUT IMPEDANCE:	$z_o = 50 \text{ ohms}$
BANDWIDTH:	
UPPER 3-db FREQUENCY:	$f_h \approx 2.3 \text{ MHz WITH } 3500 \text{ pf OF INPUT SHUNT CAPACITANCE}$
LOWER 3-db FREQUENCY:	$f_l \approx 300 \text{ Hz}$
RISE TIME:	$t_r \leq 150 \text{ nsec WITH } 3500 \text{ pf OF INPUT SHUNT CAPACITANCE}$
DC OFFSET VOLTAGE:	$V \leq +2 \text{ mv}$
SHORTED INPUT NOISE:	$\bar{v}_n \approx 0.8 \text{ nv/Hz}^{1/2} \text{ AT } 10 \text{ kHz}$
POWER REQUIREMENTS:	+15 volts dc AT 190 ma
DETECTOR BIAS VOLTAGE:	PRESET TO TEST SPECIFICATIONS FOR EACH DETECTOR CHANNEL



78-3-47

Figure 6-6. View of Large Area PV HgCdTe Detector Assembly and Preamplifier

Section 7

FINAL TEST DATA

Two complete quadrant arrays of $5 \times 5\text{-mm}^2$ elements for $3.85\text{-}\mu\text{m}$ detection were assembled, tested, and delivered under this program. In addition, six single-element detectors were delivered. These single elements were either $5 \times 5\text{ mm}^2$ or $2 \times 2\text{ mm}^2$; four were designed for $3.85\text{-}\mu\text{m}$ operation and two for $2.06\text{-}\mu\text{m}$ operation. In this section, the final test data on these detectors is reported.

QD NO. 1

The first $3.85\text{-}\mu\text{m}$ quadrant array assembled was labeled QD-1. Test data taken on this quadrant array included 500°K blackbody responsivity, relative spectral response, noise versus frequency, current versus voltage, capacitance, and pulse response to radiation from a GaAs laser diode ($0.9\text{-}\mu\text{m}$ radiation). From this basic test data, the relevant detector parameters are obtained either directly or after suitable calculations.

Table 7-1 summarizes the important detector parameters. Only two of the four channels were operating at the time of the final test. For this reason the table lists both preassembly and post-assembly data. Channel 1 failed during pump and bake-out of the glass vacuum dewar. It was partially shorted internally and only a small portion of the total diode area was responsive to signal radiation. It did show diode I-V characteristics and some blackbody responsivity. Channel 2 was originally working, but developed an open circuit after a number of temperature cycles between 77°K and 300°K . This problem is probably correctable, but would require opening of the glass dewar package. Channels 1 and 2 are operating as expected.

The responsivity and detectivity values at high frequency were obtained indirectly in the following way. A conventional chopped blackbody signal was used to obtain a value for responsivity at some low frequency, for example, 2 kHz. The blackbody responsivity was then converted to peak responsivity

Table 7-1. Measured Test Data on PV HgCdTe Large Area Quadrant Array No. QD-1

CHANNEL NUMBER	PREASSEMBLY TEST				POST-ASSEMBLY TEST			
	1	2	3	4	1	2	3	4
D^* (λ_p , 2kHz) (cm Hz ^{1/2} /watt)	2.1×10^{11}	2.3×10^{11}	2.2×10^{11}	2.4×10^{11}	0.6×10^{11}	3.5×10^{11}	2.8×10^{11}	3.2×10^{11}
D^* (λ_p , 1MHz) (cm Hz ^{1/2} /watt)	-	-	-	-	-	-	4.0×10^{10}	6.1×10^{10}
R_V (λ_p , 2kHz) (volts/watt)	2.2×10^3	2.8×10^3	2.4×10^3	2.7×10^3	-	-	1.6×10^3	2.1×10^3
R_V (λ_p , 1MHz) (volts/watt)	-	-	-	-	-	-	1.4×10^3	1.7×10^3
τ (nsec)	450	<100	100	100	100	-	110	100
C_0 (pf)	>11,000	4,407	5,750	3,927	2,735	4,434	4,611	3,383
I_{sc} (μ a)	43	40	35	40	3	48	33	41
R_0 (ohms)	2.8×10^3	2.4×10^3	2.2×10^3	1.7×10^3	1.9×10^4	4.3×10^4	3.5×10^4	1.0×10^5
$R_0 A_j$ (ohm cm ²)	8.7×10^2	7.5×10^2	6.9×10^2	5.3×10^2	5.9×10^3	1.3×10^4	1.1×10^4	3.1×10^4
η (at λ_p)	0.74	0.90	0.78	0.90	-	0.87	0.64	0.79
λ_p (μ m)	3.9	3.8	3.6	3.8	-	-	-	-

$A_d = 0.284 \text{ cm}^2$

$A_j = 0.312 \text{ cm}^2$

$R_f = 1 \text{ K ohm}$

$T = 77 \text{ to } 80^\circ \text{K}$

using the detector's relative spectral response curve and the usual integration procedure. After measurement of the detector's response time τ with the GaAs laser pulse, the high-frequency responsivity at any point f was then calculated from the formula

$$R_V(\lambda_p, f) = \frac{R_V(\lambda_p, 2\text{kHz})}{[1 + (2\pi f)^2 \tau^2]^{\frac{1}{2}}}$$

The 2-kHz responsivity is at a low enough frequency so that it is essentially the dc or zero frequency value. The use of this expression presumes that the detector has a simple exponential response time. Since exponential decay curves were observed with the GaAs laser pulse it is believed that this procedure yields valid responsivity data in the high-frequency range.

The noise at high frequencies was measured directly using a wave analyzer which measures to 18 MHz (Hewlett-Packard Model 312A). With this noise data and the calculated responsivity values, the detectivity could then be calculated at any frequency. A plot of $D^*(\lambda_p)$ versus frequency generated in this way is shown in Figure 7-1. The drop off in $D^*(\lambda_p)$

at low frequencies is caused by $1/f$ noise in the preamplifier. The drop off at high frequencies is caused by both loss of responsivity and an increase of noise which is characteristic of current-mode amplifiers. As described in Section 2, these factors are primarily controlled by the detector capacitance. Figures 7-2 through 7-7 show additional final test data on QD-1, including responsivity and noise versus frequency, relative spectral response, and current-voltage curves.

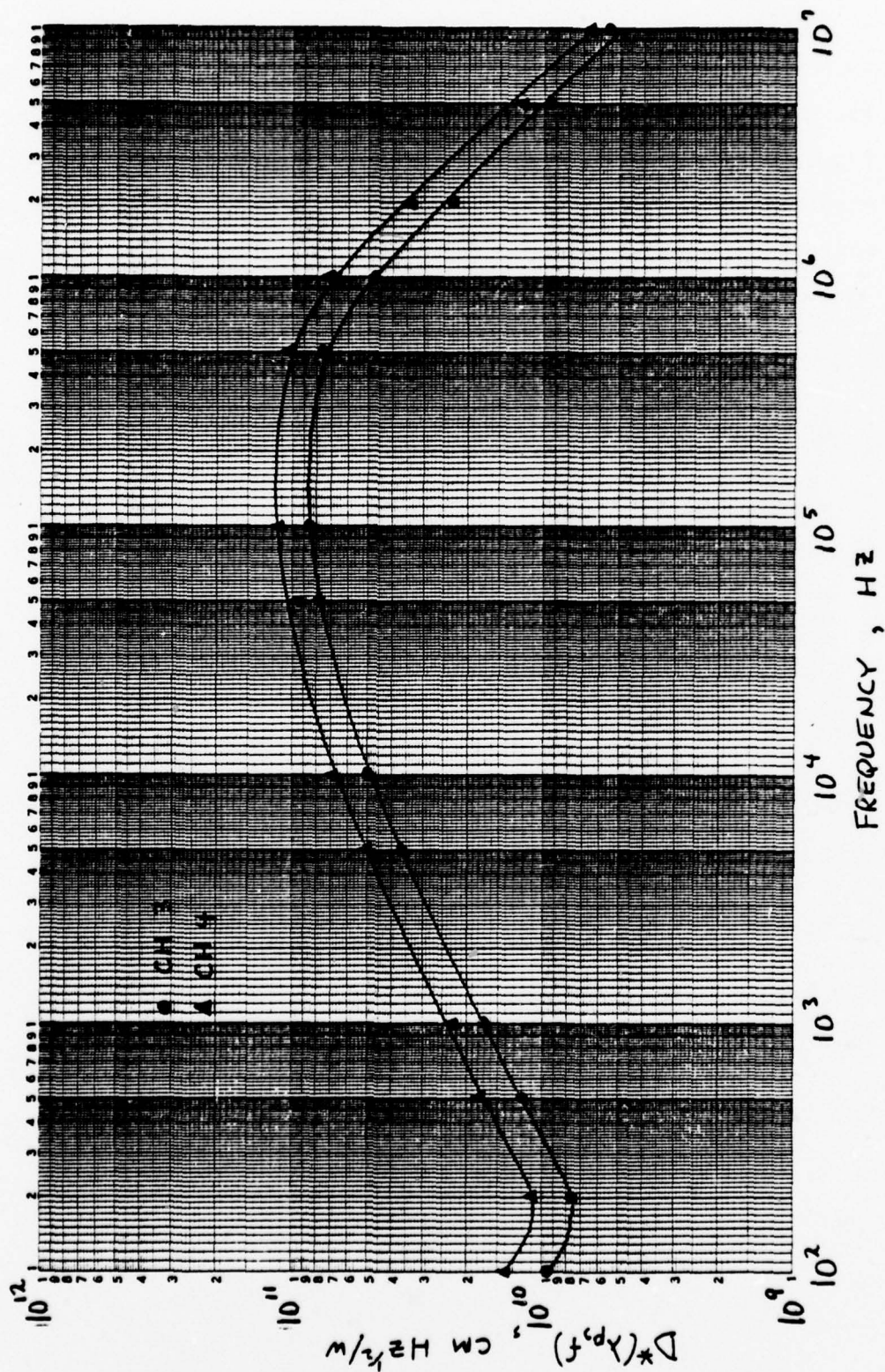


Figure 7-1. Detectivity versus Frequency for QD No. 1

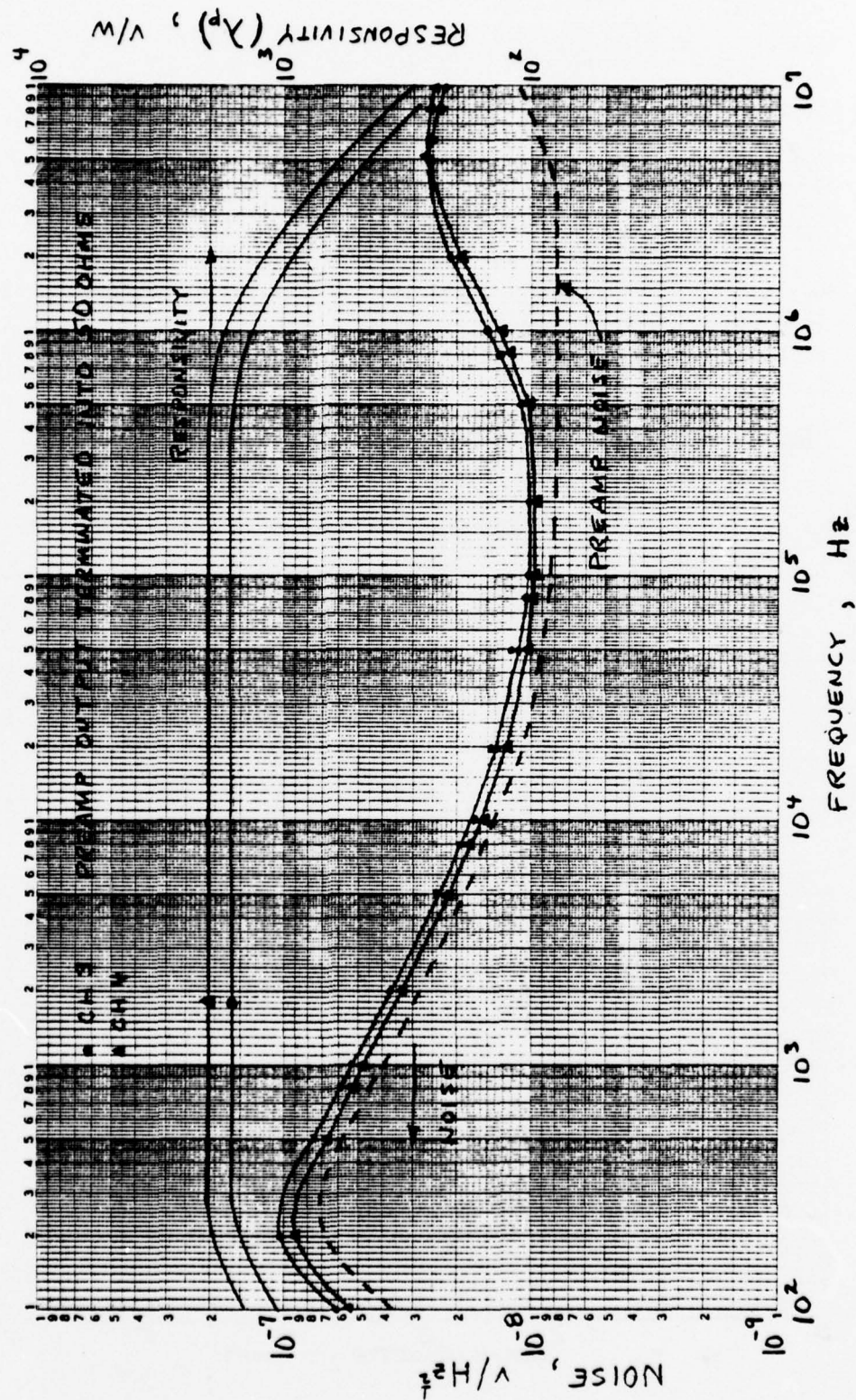


Figure 7-2. Responsivity and Noise versus Frequency for QD No. 1

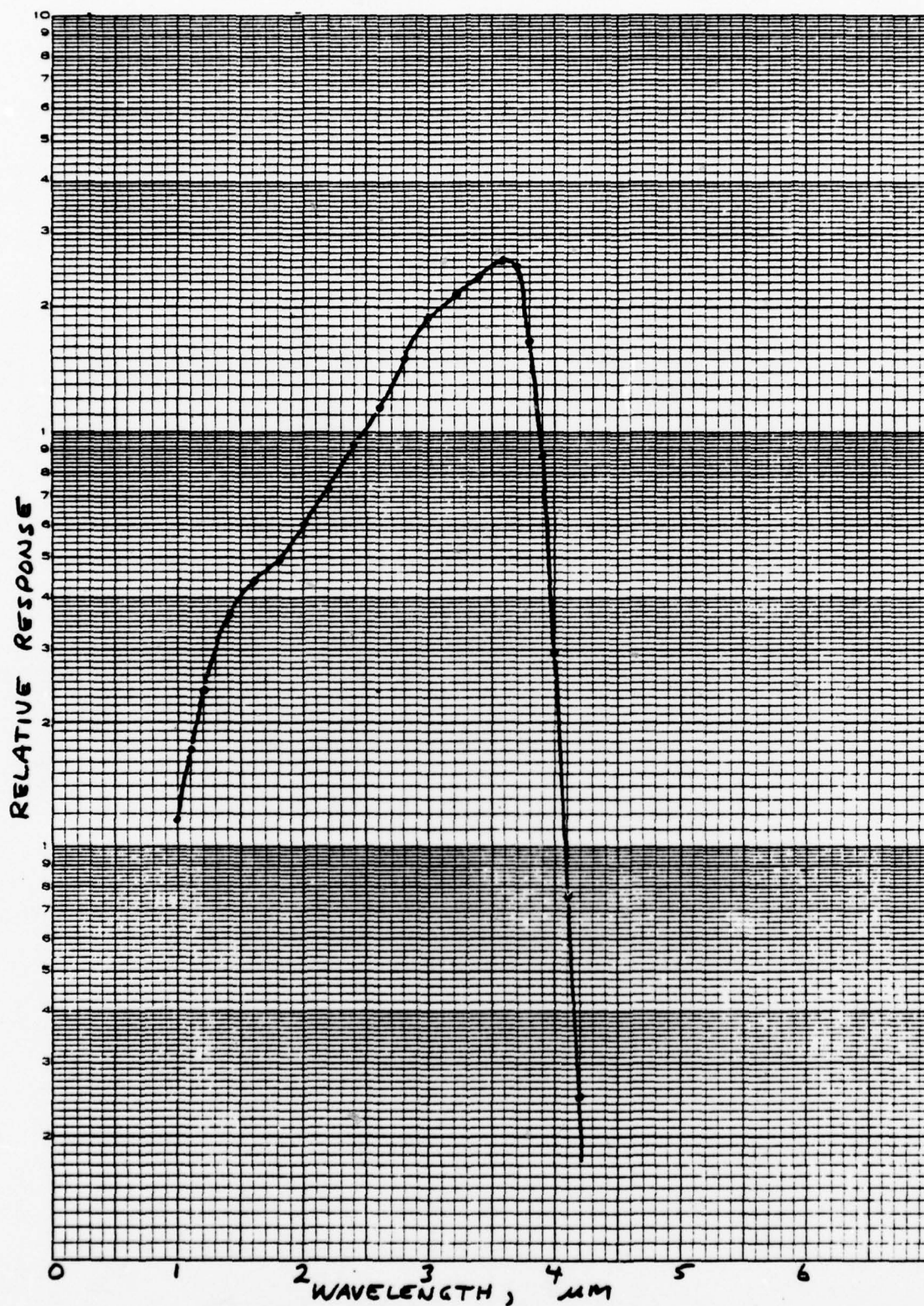


Figure 7-3. Relative Spectral Response for Channel 3 of QD No. 1

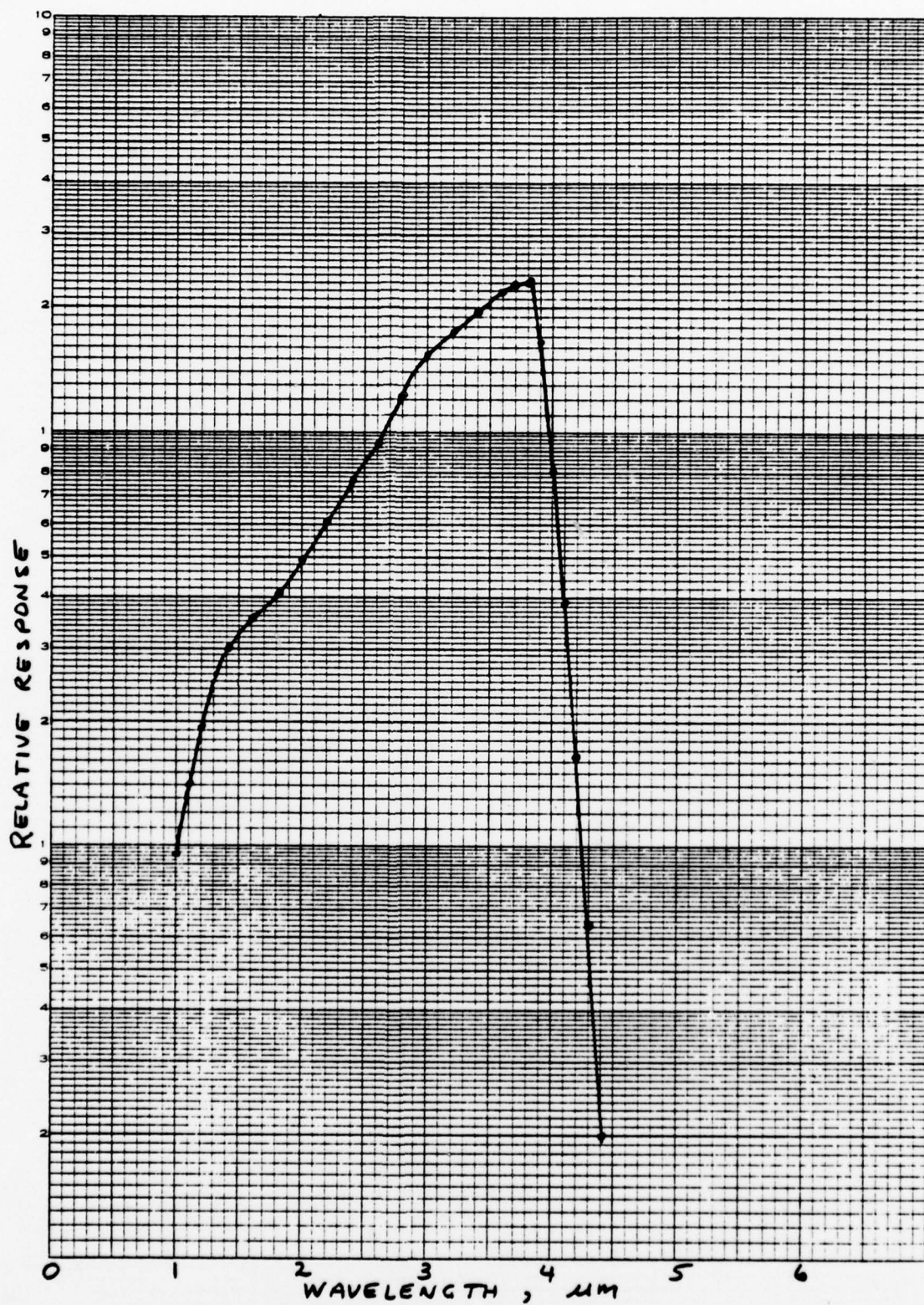


Figure 7-4. Relative Spectral Response for Channel 4 of QD No. 1

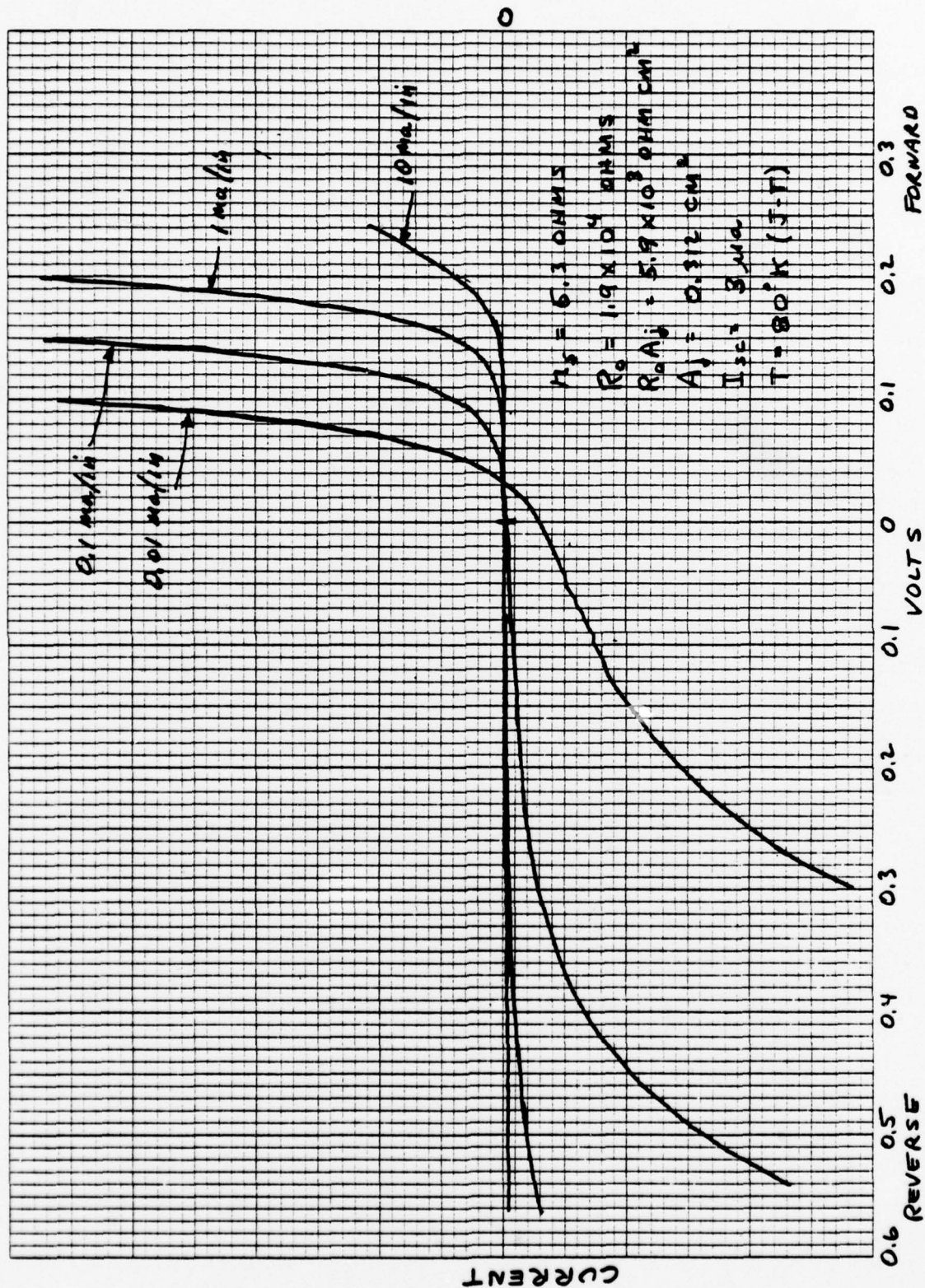


Figure 7-5. Current versus Voltage Curves for Channel 1 of QD No. 1

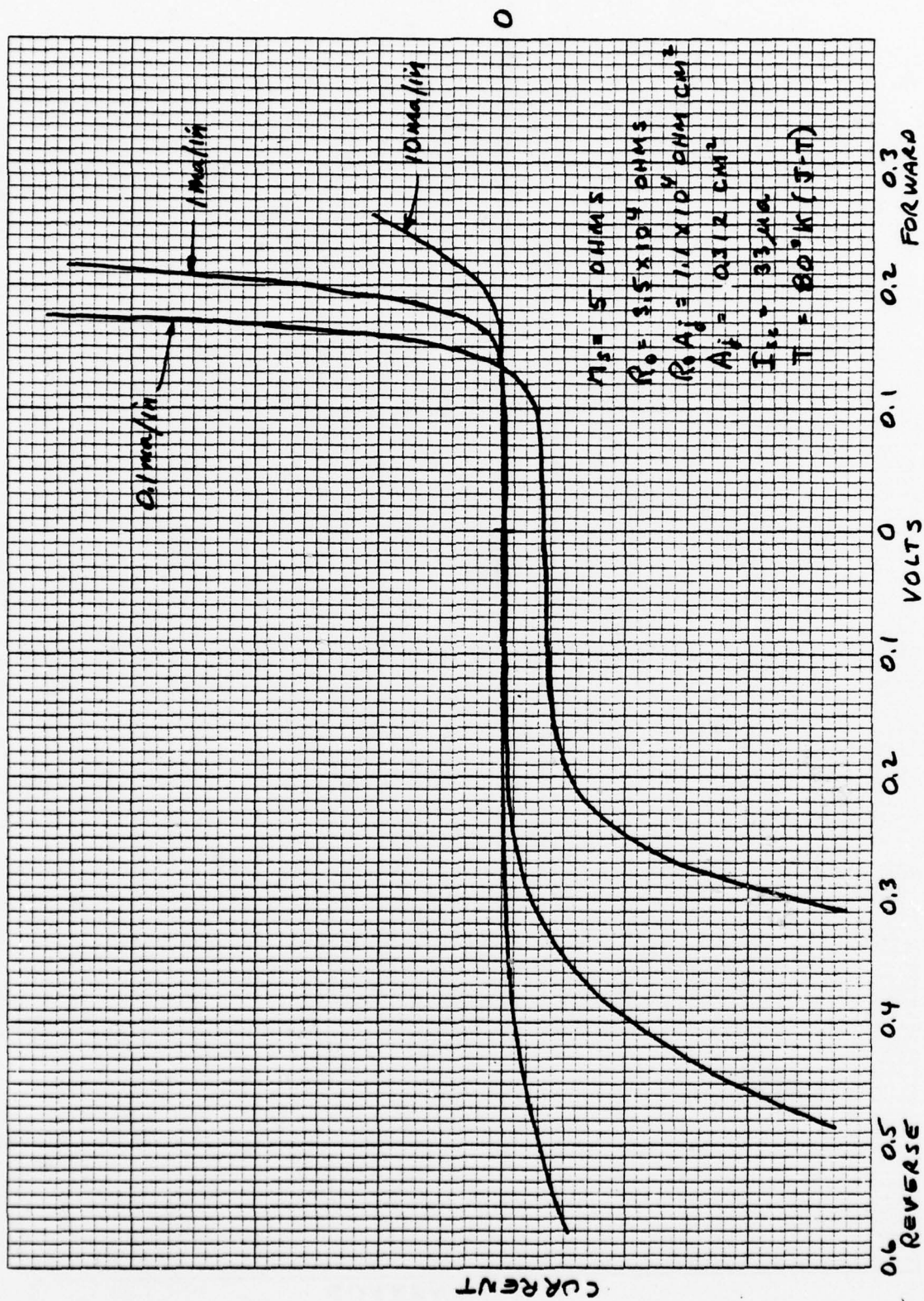


Figure 7-6. Current versus Voltage Curves for Channel 3 of QD No. 1

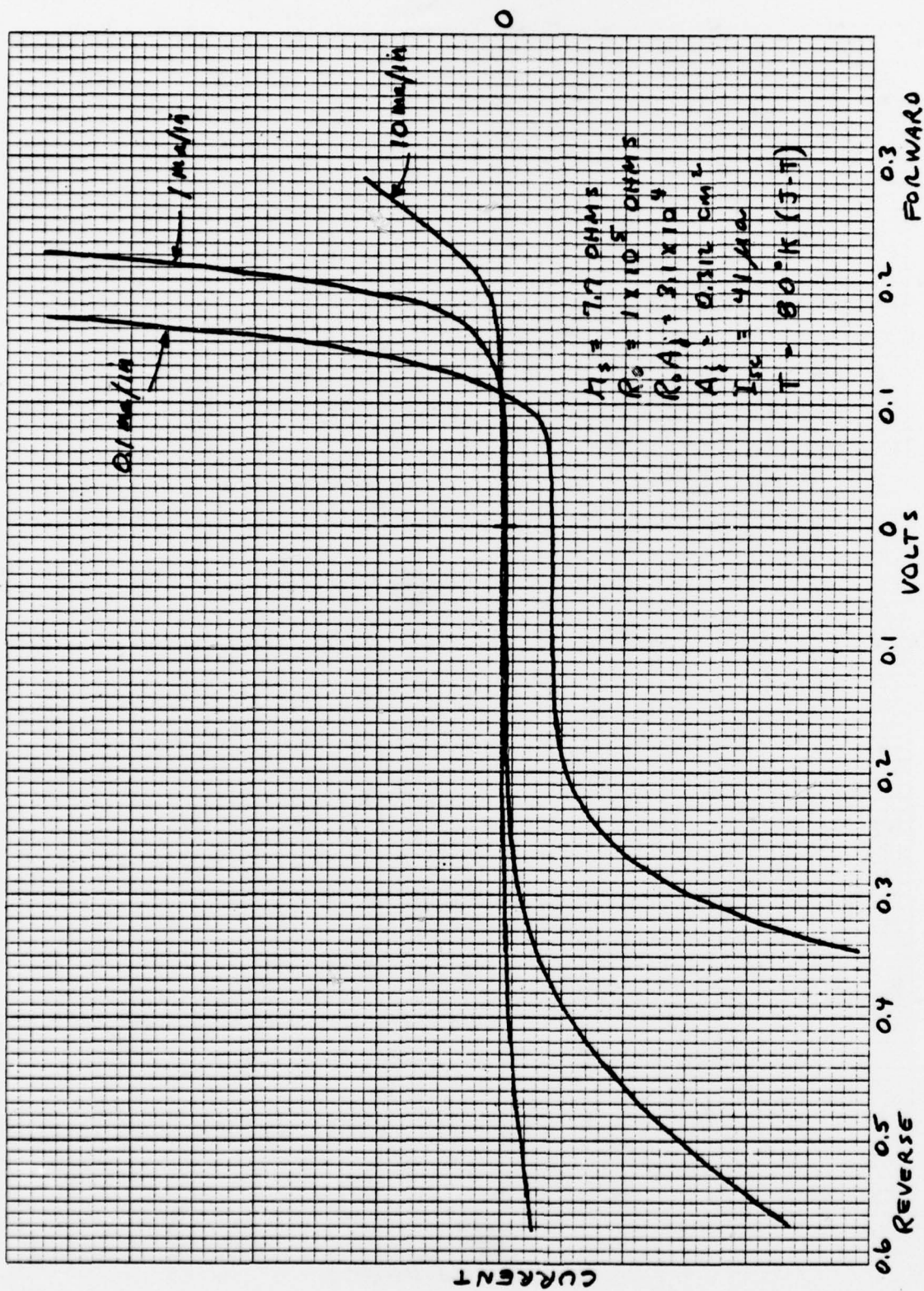


Figure 7-7. Current versus Voltage Curves for Channel 4 of QD No. 1

QD NO. 2

The second 3.85- μm quadrant array assembled was labeled QD No. 2. This array was tested in the same manner as the first quadrant array. Table 7-2 summarizes the important detector test parameters. Figures 7-8 through 7-17 show additional final test data including detectivity, responsivity and noise versus frequency, relative spectral response, current-voltage curves and spot scan uniformity profiles.

Table 7-2. Measured Test Data on PV HgCdTe Large Area Quadrant Array No. QD-2

CHANNEL NUMBER	1	2	3	4
D^* (λ_p , 2kHz) ($\text{cm Hz}^{1/2}/\text{watt}$)	8.9×10^{10}	7.2×10^{10}	9.0×10^{10}	10.1×10^{10}
D^* (λ_p , 1MHz) ($\text{cm Hz}^{1/2}/\text{watt}$)	5.8×10^{10}	4.5×10^{10}	5.9×10^{10}	7.9×10^{10}
R_V (λ_p , 2kHz) (volts/watt)	3.7×10^3	2.9×10^3	4.0×10^3	3.7×10^3
R_V (λ_p , 1MHz) (volts/watt)	2.4×10^3	1.8×10^3	2.6×10^3	2.9×10^3
τ (nsec)	190	200	180	130
I_{sc} (μa)	54	41	70	47
R_0 (ohms)	3.2×10^3	2.3×10^3	9.5×10^2	2.1×10^3
R_{0A_j} (ohm cm^2)	9.9×10^2	7.2×10^2	3.0×10^2	6.6×10^2
λ_p (μm)	4.0	4.1	4.1	3.8

$$A_d = 0.284 \text{ cm}^2$$

$$A_j = 0.312 \text{ cm}^2$$

$$R_f = 1 \text{ K ohm}$$

$$T = 80^\circ\text{K}$$

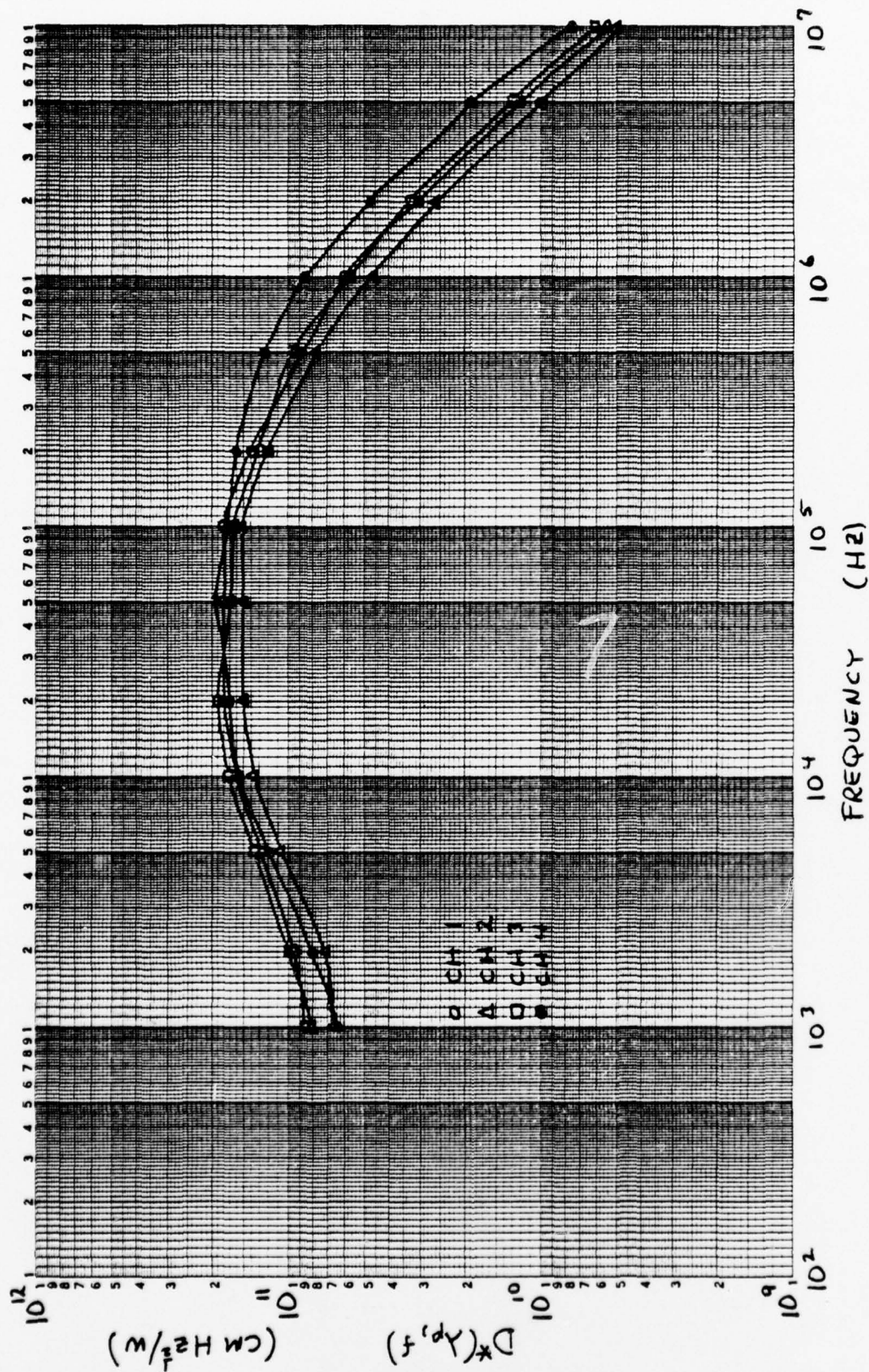


Figure 7-8. Detectivity versus Frequency for QD No. 2

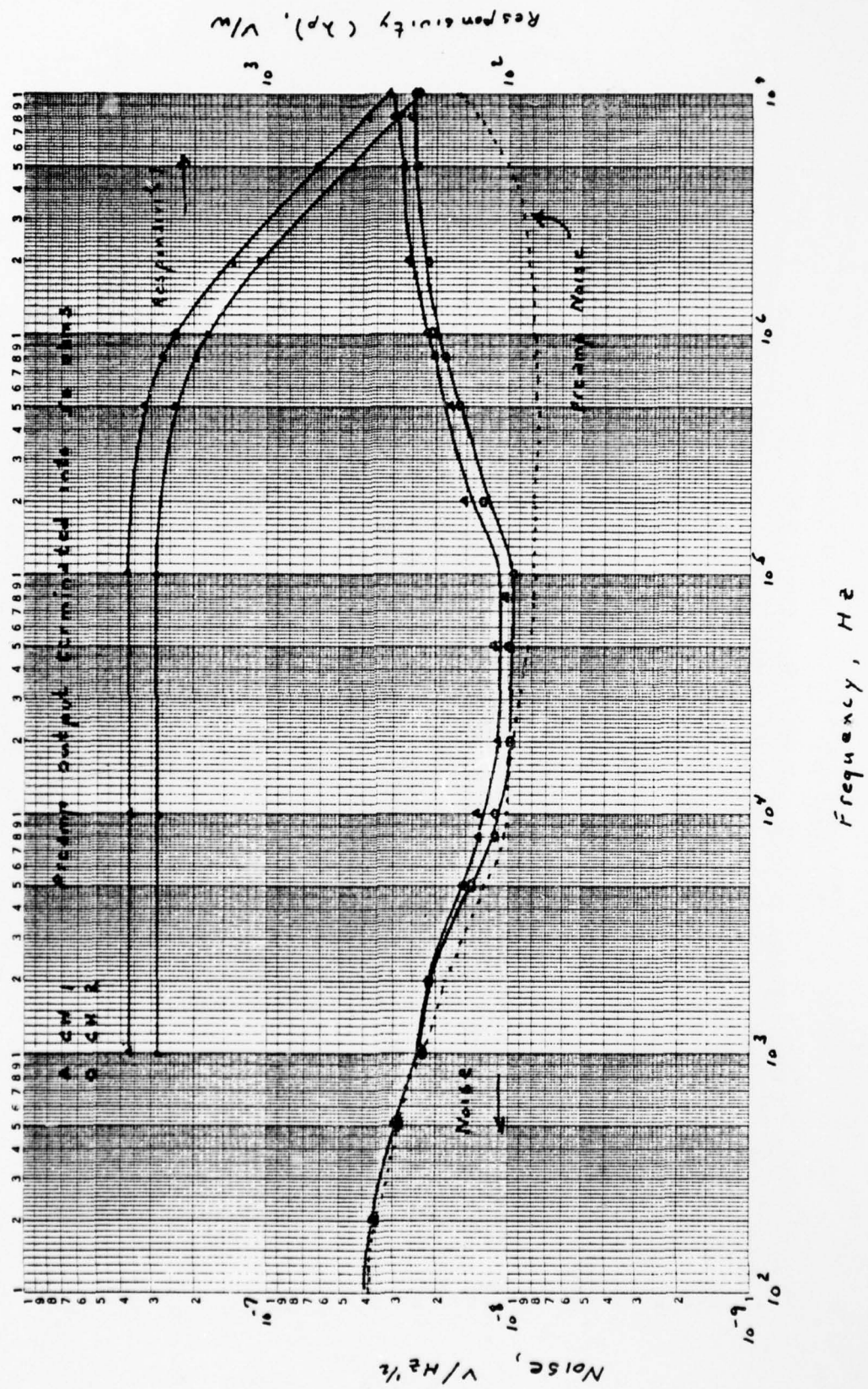


Figure 7-9. Responsivity and Noise versus Frequency for Channels 1 and 2 of QD No. 2

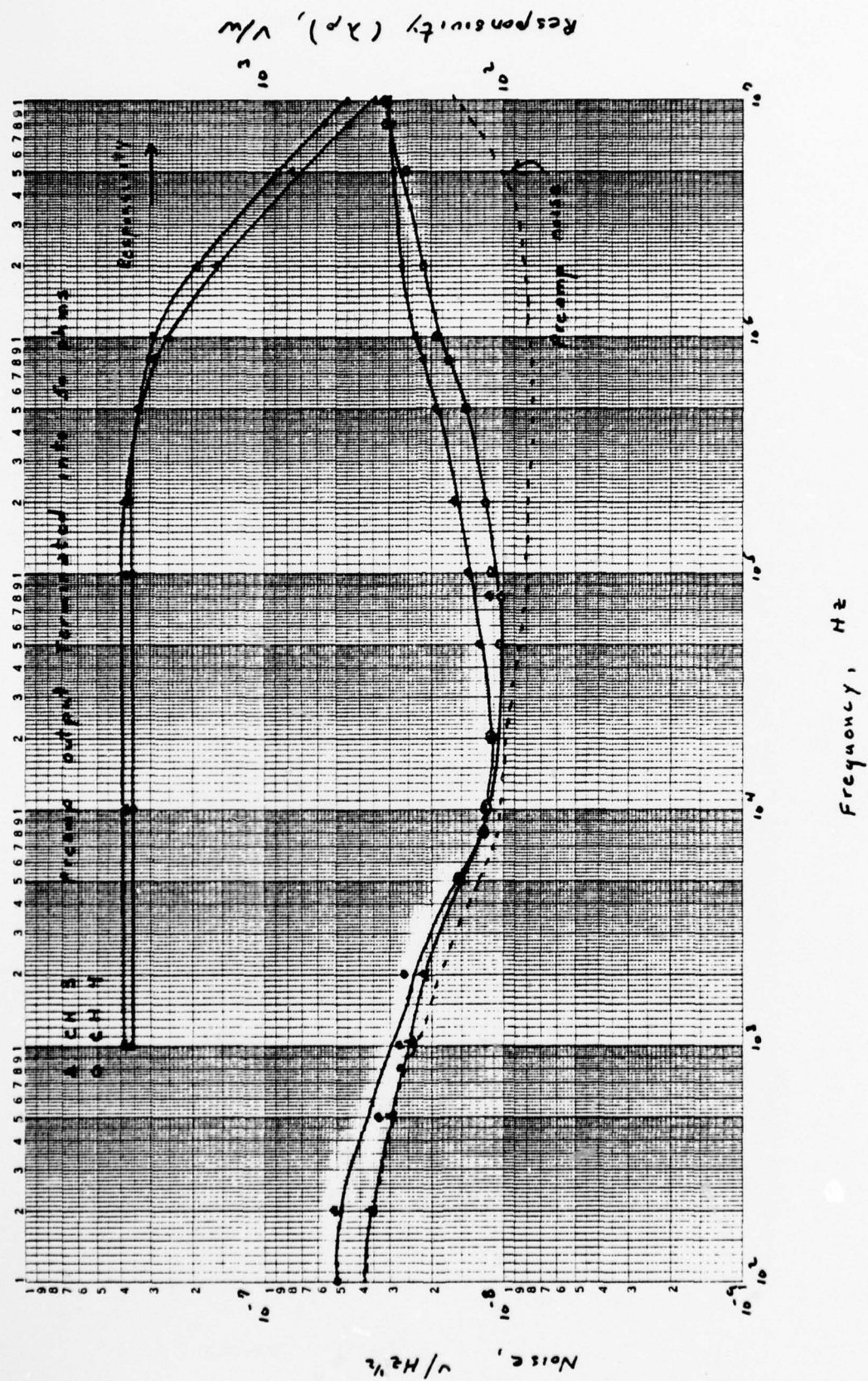


Figure 7-10. Responsivity and Noise versus Frequency for Channels 3 and 4 of QD No. 2

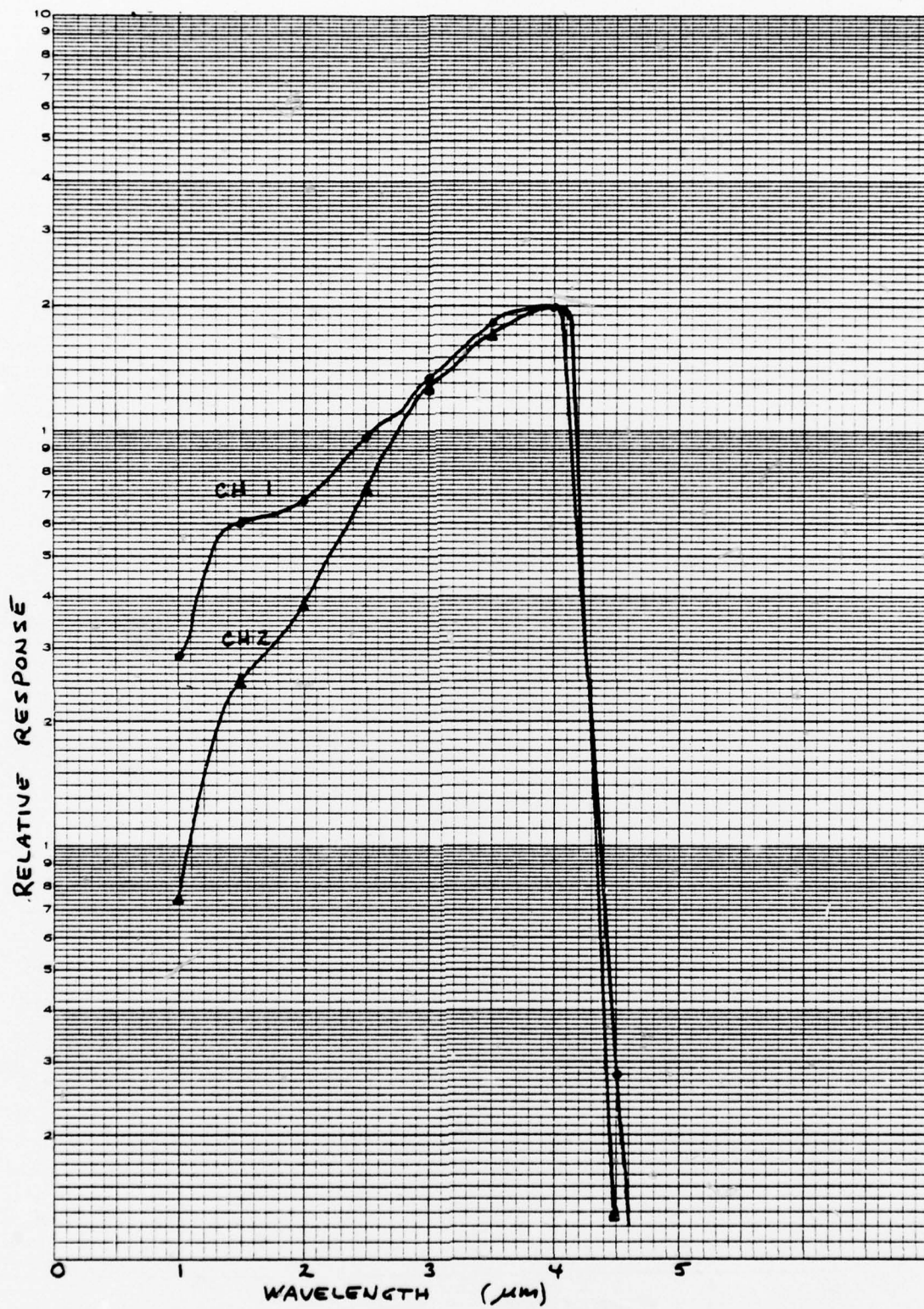


Figure 7-11. Relative Spectral Response for Channels 1 and 2 of QD No. 2

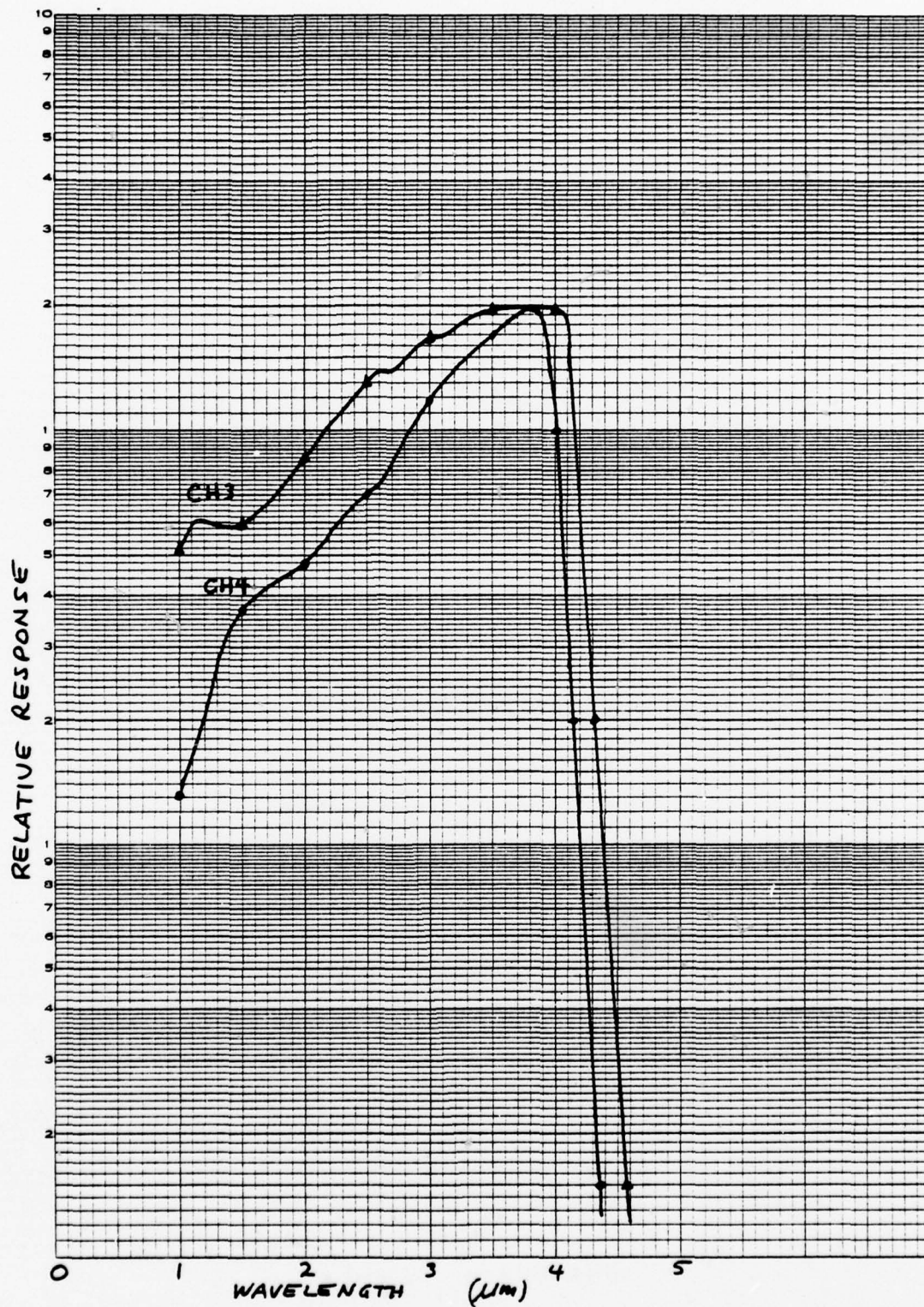


Figure 7-12. Relative Spectral Response for Channels 3 and 4 of QD No. 2

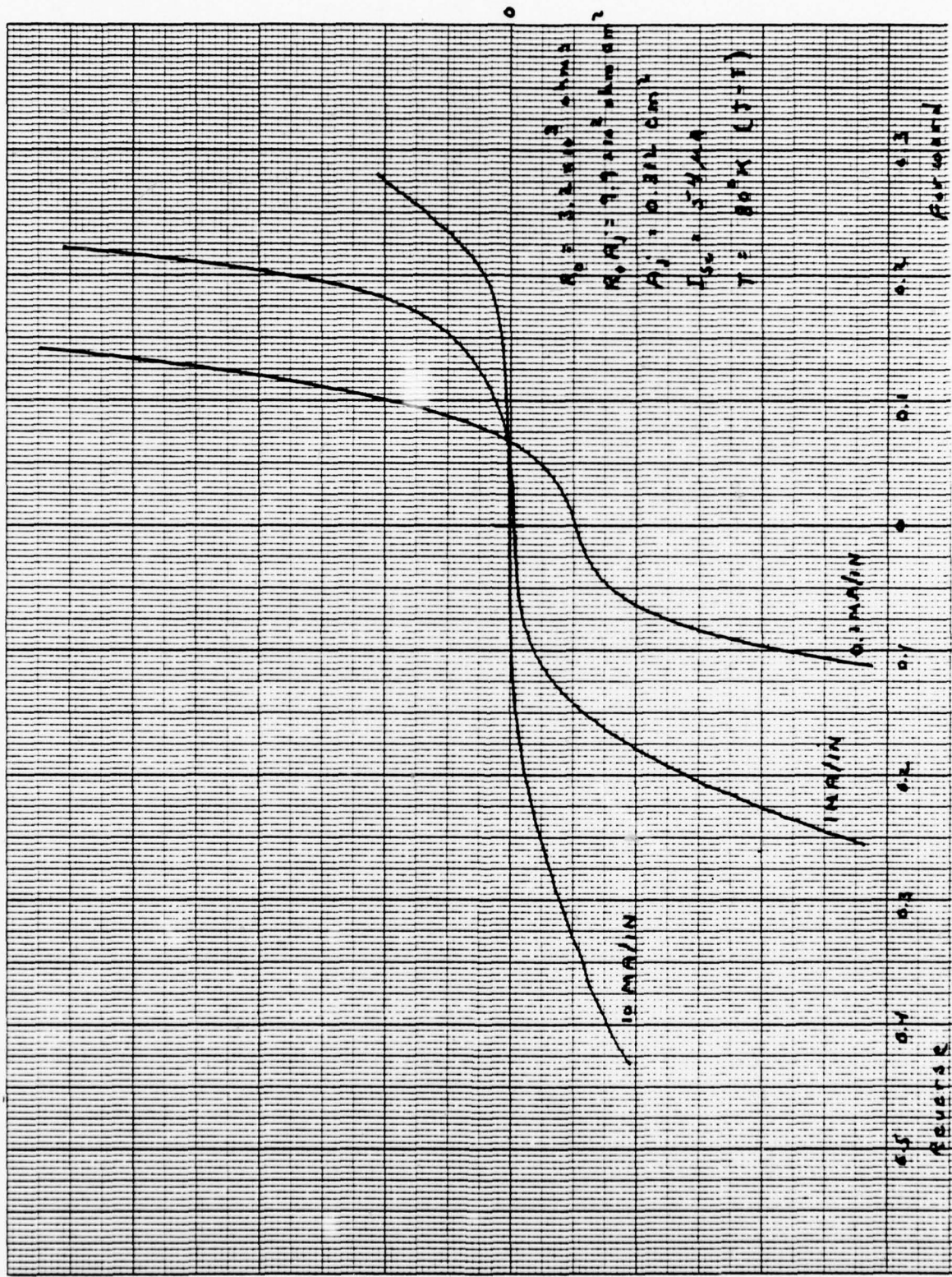


Figure 7-13. Current versus Voltage Curves for Channel 1 of QD No. 2

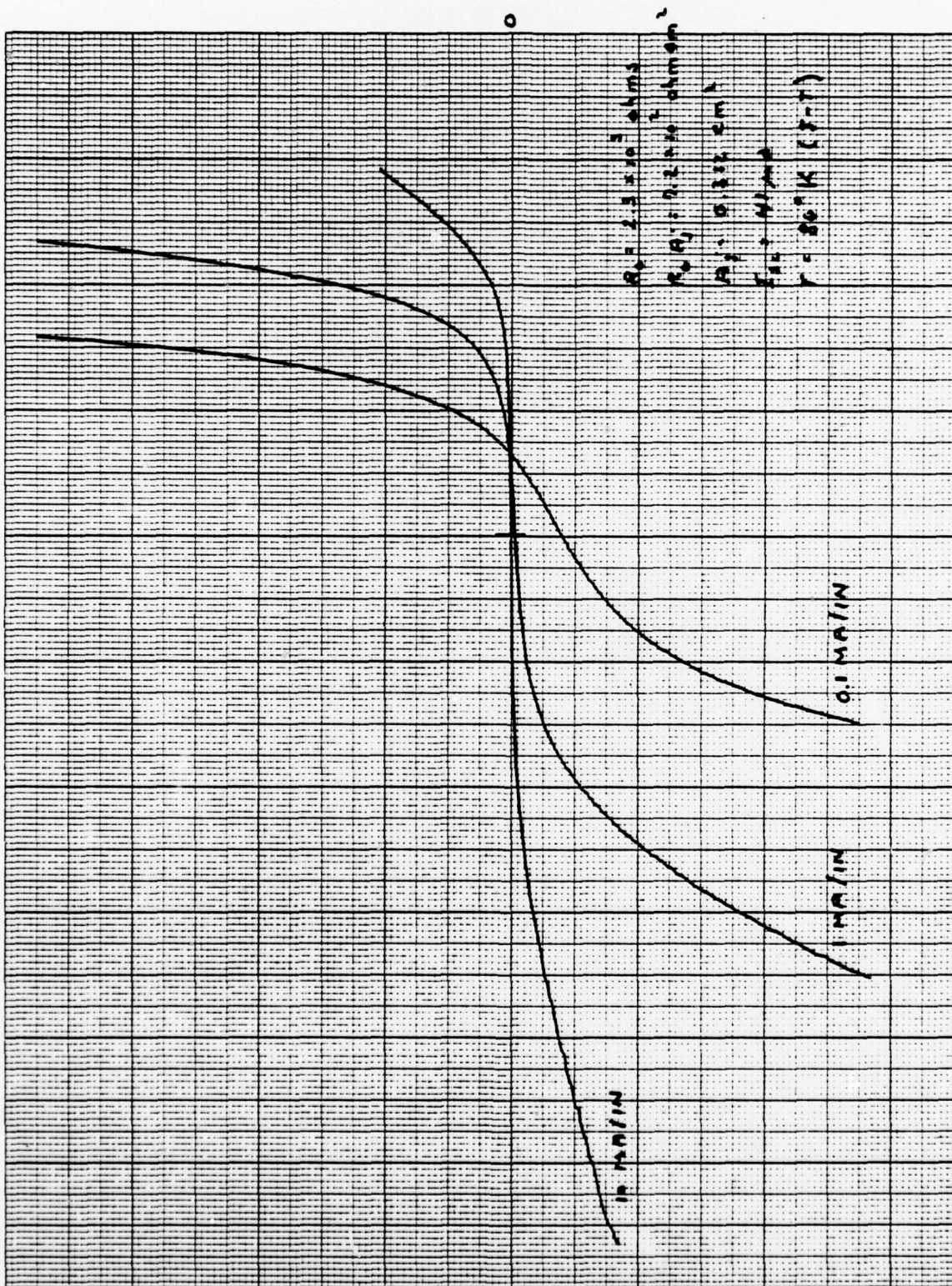


Figure 7-14. Current versus Voltage Curves for Channel 2 of QD No. 2

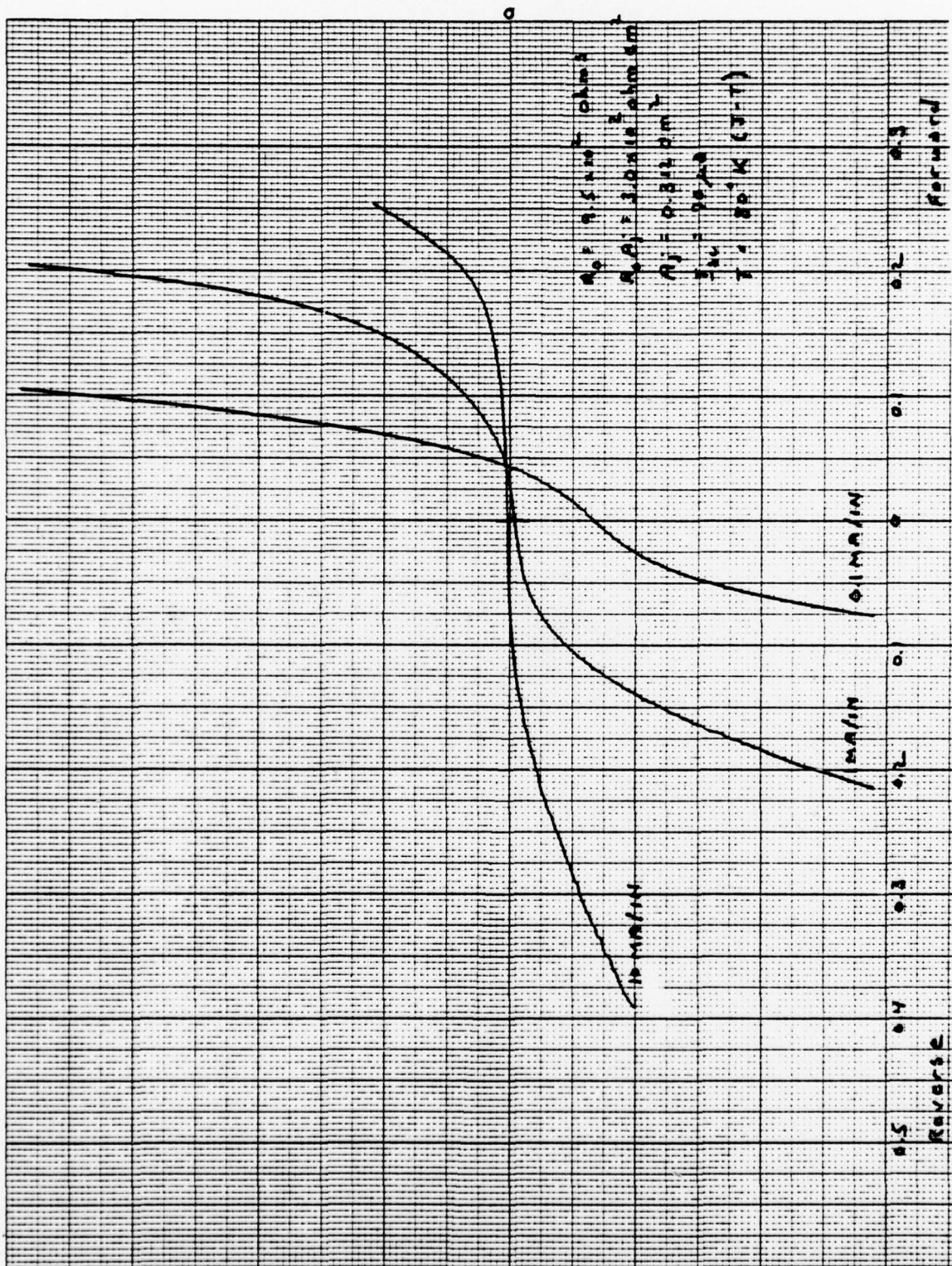


Figure 7-15. Current versus Voltage Curves for Channel 3 of QD No. 2

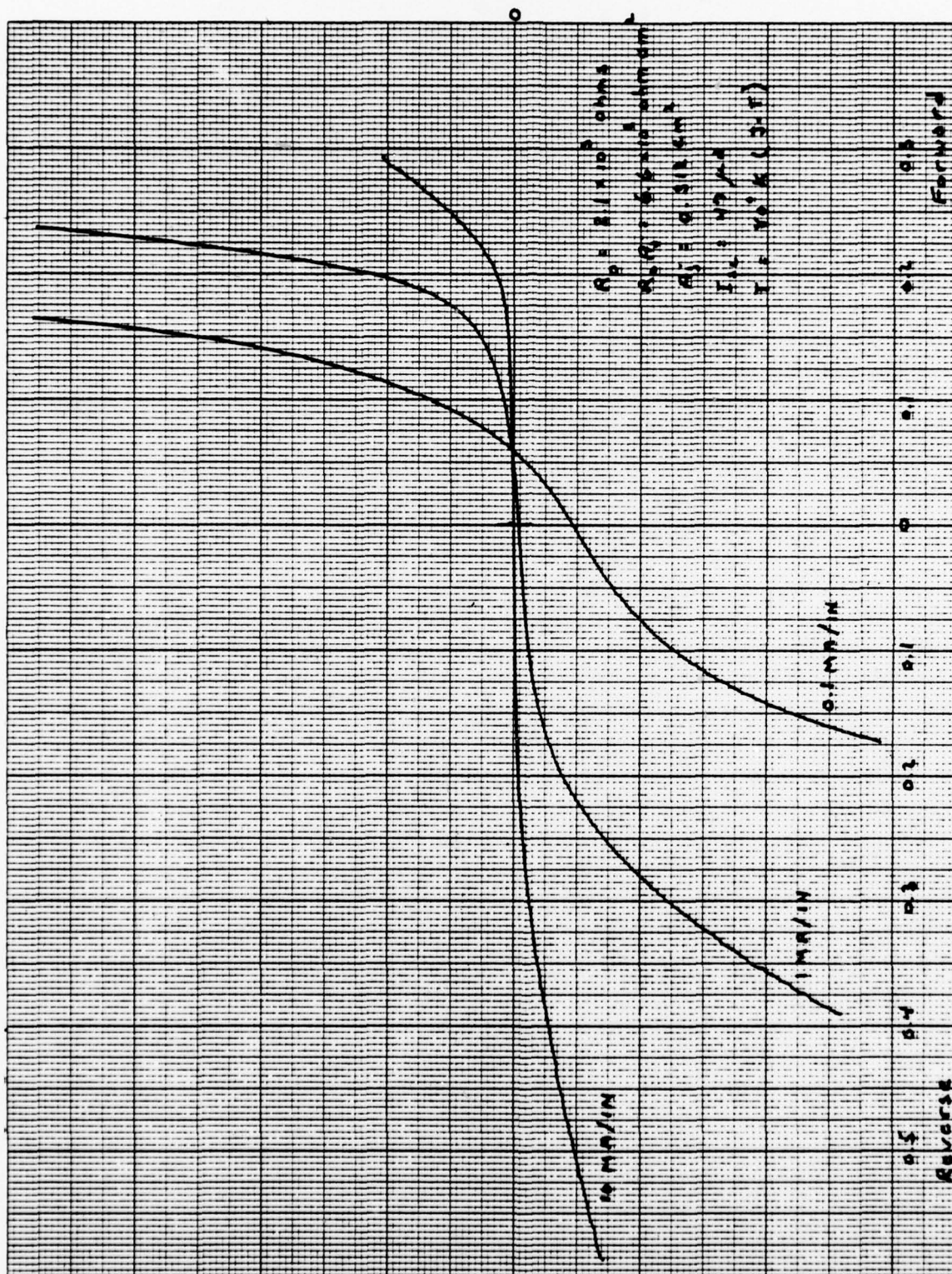


Figure 7-16. Current versus Voltage Curves for Channel 4 of QD No. 2

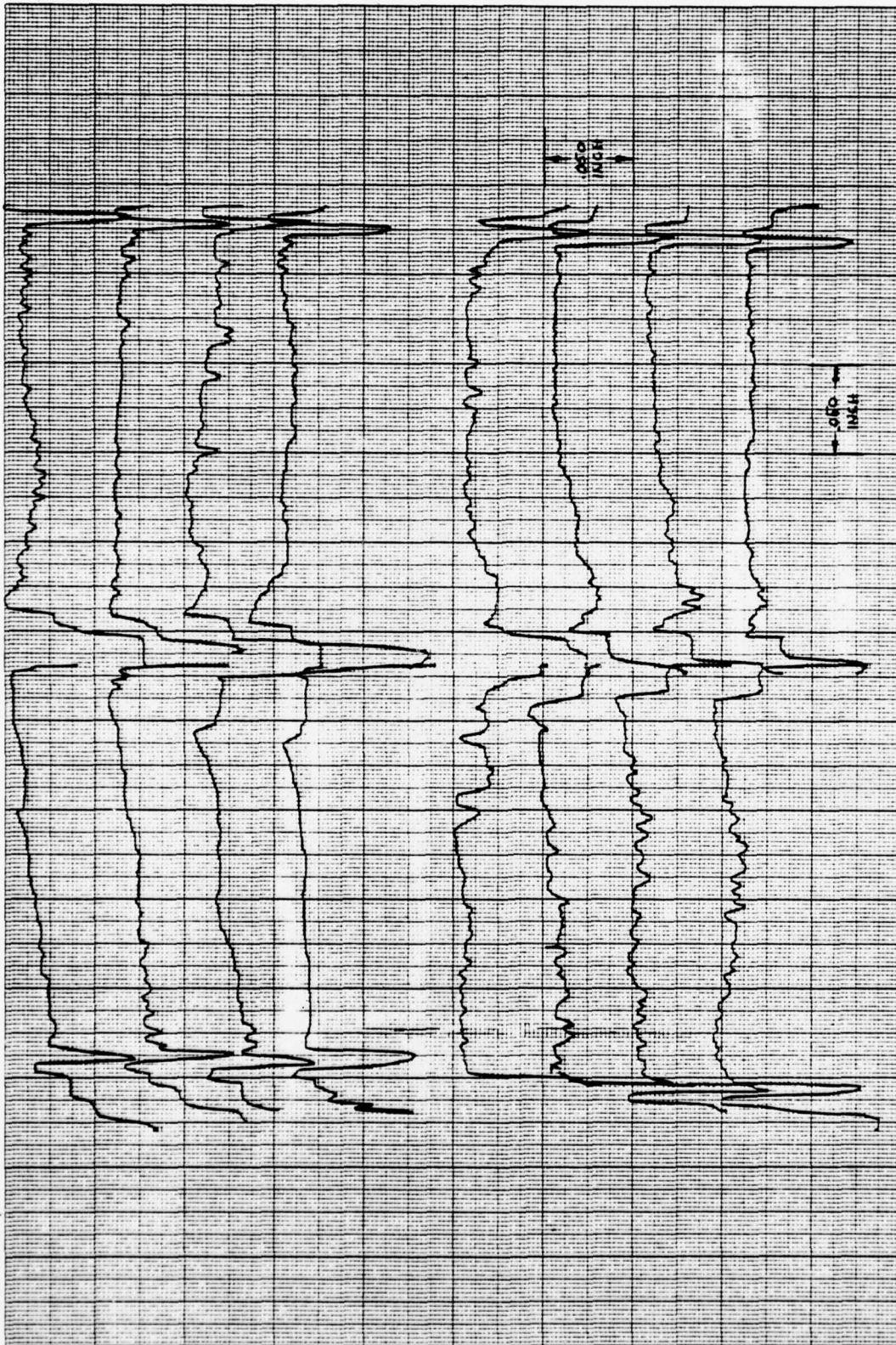


Figure 7-17. Spot Scan Profiles for the Completed Array QD No. 2

SINGLE ELEMENT DETECTORS

The six single-element detectors were delivered as separate items along with a metal LN₂ dewar for testing them. These elements were mounted on metal disks which are easily installed or removed from the dewar. After installation of a detector, the dewar can be evacuated by attaching to a vacuum pump station capable of pumping to less than 10^{-5} torr. A valve on the dewar is then closed off and the dewar will maintain vacuum for several weeks of operation before it needs repumping.

Table 7-3 lists the serial numbers of these six detectors, their nominal peak wavelengths and their areas.

Table 7-3. Serial Numbers of Single Element Detectors

SERIAL NO.	WAVELENGTH	AREA
2-132-25	3.85 μm	5 X 5 mm ²
2-132-20	3.85 μm	5 X 5 mm ²
2-132-10-1	3.85 μm	2 X 2 mm ²
2-132-10-2	3.85 μm	2 X 2 mm ²
RC4-2K-L	2.06 μm	2 X 2 mm ²
RC4-2K-R	2.06 μm	2 X 2 mm ²

The following pages give the test data acquired on these detectors. There is a "Detector Test Report" page for each detector. Following each of these pages are other graphs showing additional test data such as spectral response, current-voltage curves, or spot scan profiles. In the case of the 2.06- μm detectors, data is given for operating temperatures of both 77° and 192°K.

Santa Barbara Research Center
75 Coromar Drive
Goleta, California 93017
(805) 968-3511

DETECTOR TEST REPORT

Detector Serial Number 2-132-25 Test Date 5/5/77

DETECTOR CONSTRUCTION

Type	<u>PV HgCdTe</u>	Dewar Style	<u>40742</u>	S. N.	<u>3643</u>
Sensitive Area	<u>0.284</u> cm^2	Filter	<u>None</u>		
Configuration	<u>nom. 5 x 5 mm²</u>	Window: Material	<u>Sapphire</u>		
Field of View	<u>11</u> Deg	Window: AR Coating Pk	<u>--</u>	μm	
FOV Aperture: Size	<u>--</u>	Element to window distance	<u>15/16 inch</u>		
	Distance from cell				
	<u>--</u>				

TEST RESULTS

$R(\lambda_p)$	<u>2.8</u>	amp/watt
NEP (λ_p)	<u>2.0×10^{-12}</u>	watt/Hz ^{1/2}
$D^*(\lambda_p)$	<u>1.3×10^{11}</u>	$\text{cm Hz}^{1/2}/\text{w}$
$D^*(\text{BB})$	<u>1.9×10^{10}</u>	$\text{cm Hz}^{1/2}/\text{w}$
Resistance	<u>210</u>	ohms
Signal	<u>5.2</u>	m volt
Noise	<u>0.24</u>	μ volt
Time Constant	<u>not measured, approx. 0.1</u>	μ sec (5)
λ_p	<u>4.1</u>	μm (4)
Blackbody to Peak Conversion Factor	<u>13.6</u>	
Quantum Efficiency (at λ_p)	<u>85%</u>	

CONDITIONS OF MEASUREMENT

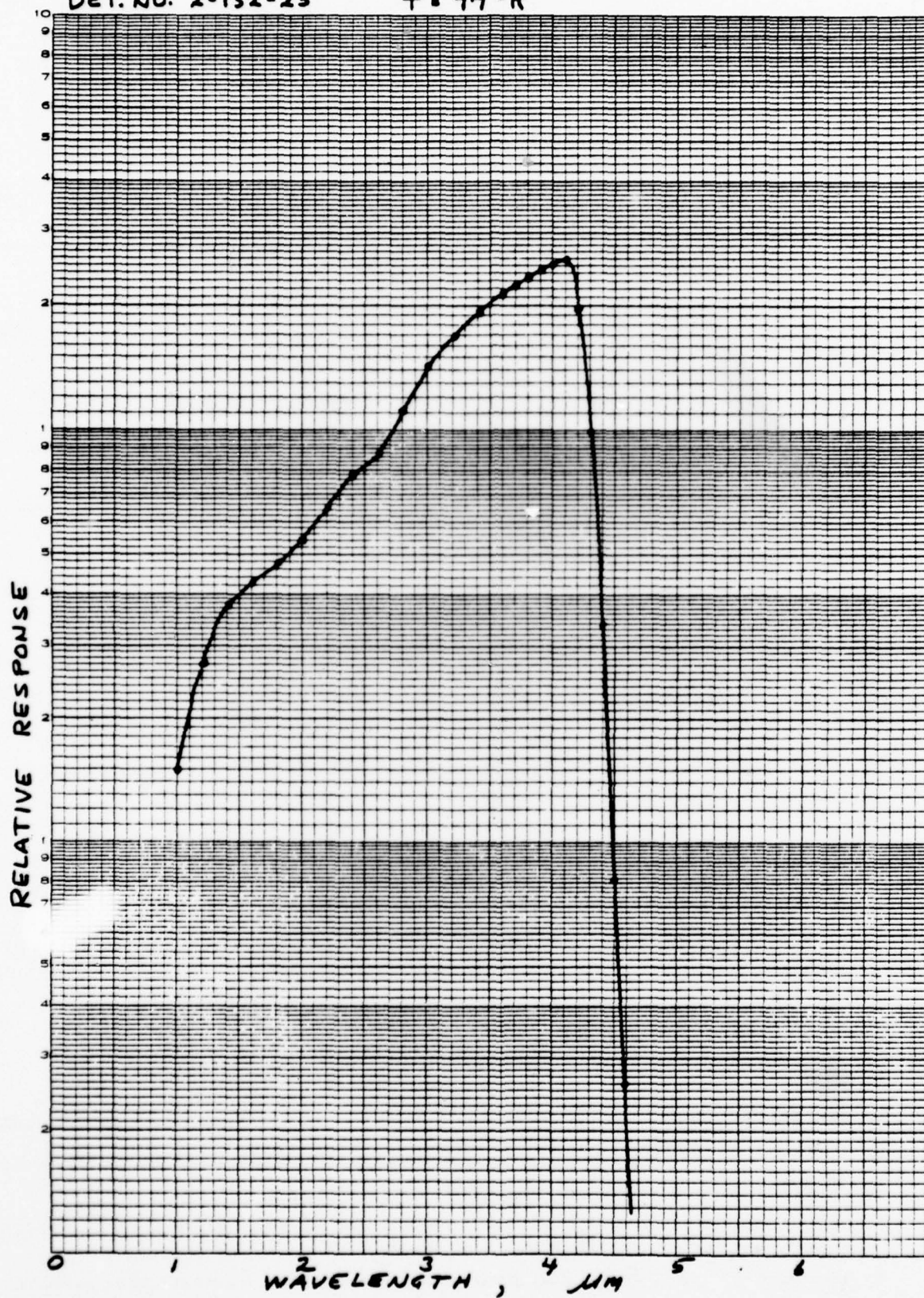
Frequency	<u>1800</u>	Hertz
Bandwidth	<u>6</u>	Hertz
BB Flux Density	<u>10</u>	$\mu\text{w}/\text{cm}^2$
BB Temperature	<u>500</u>	Deg K
Detector Temp.	<u>77</u>	Deg K
Feedback Resistor	<u>10^4</u>	ohms
Bias Voltage	<u>0</u>	volts

NOTES:

1. For all correspondence relative to this detector, please refer to SBRC W/A B214.
2. Customer U.S. Army Electronics Command, Ft. Monmouth
3. Customer's P. O. No. Cont. No. DAAB07-76-C-0803
4. The BB to peak conversion factor listed is based on the relative spectral response measurements included with this data sheet.
5. Measured with SBRC Model A231 preamplifier which has a 1-kohm feedback resistor.

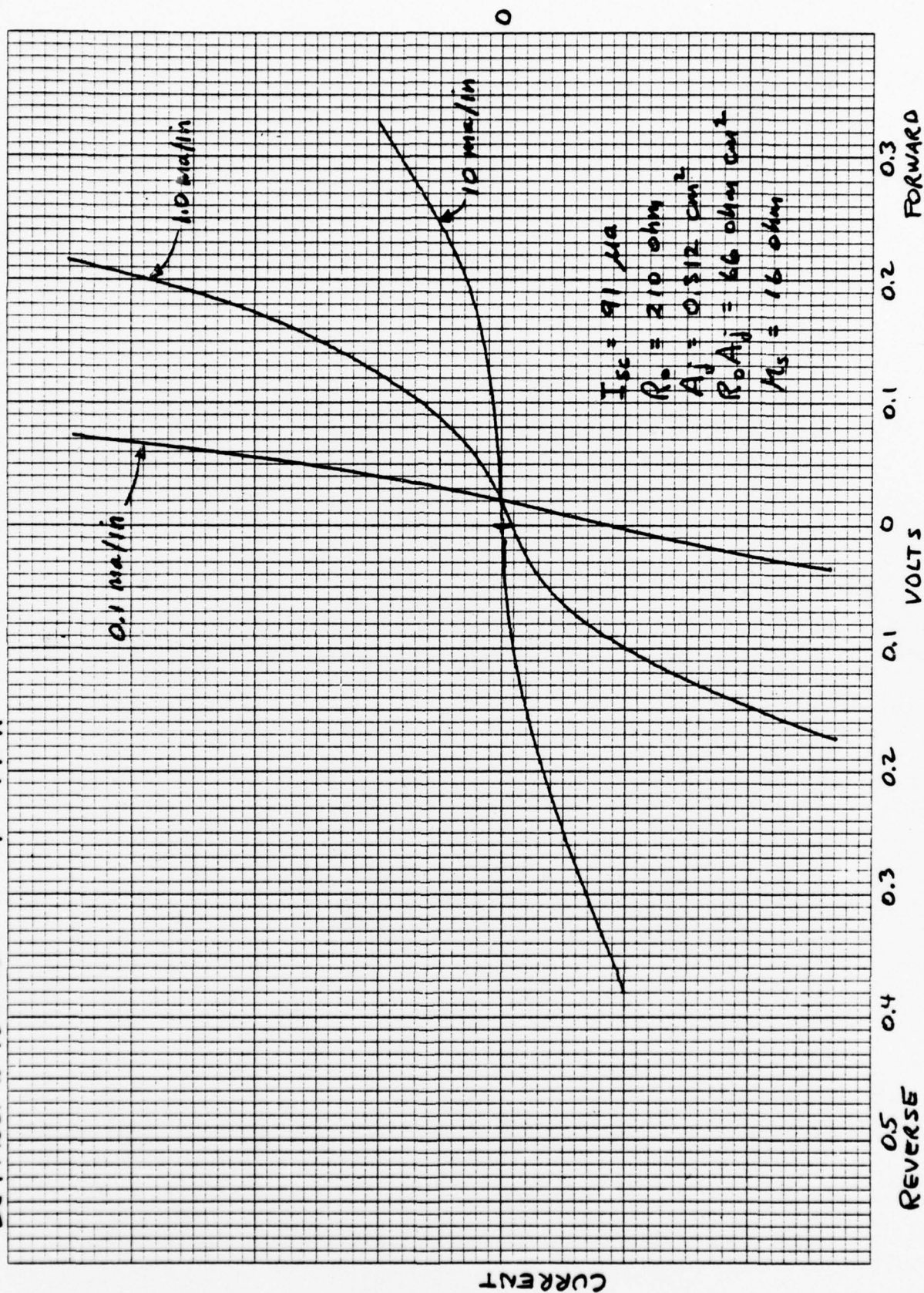
DET. NO. 2-132-25

T = 77°K



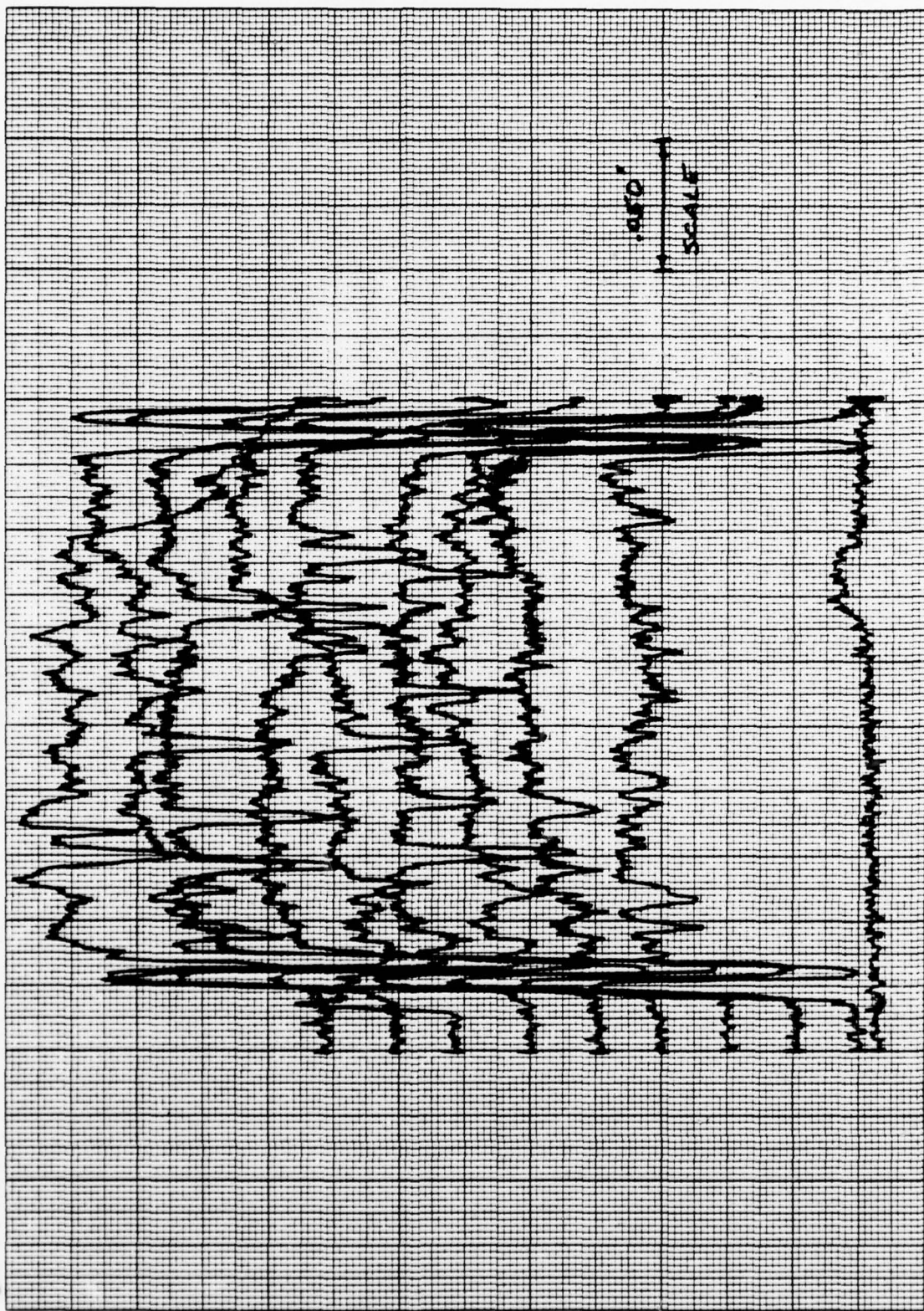
DET. NO. 2-132-25

T = 77°K



T = 77°K

DET. NO. 2-132-25



SENSITIVITY CONTOURS

Santa Barbara Research Center
75 Coromar Drive
Goleta, California 93017
(805) 968-3511

DETECTOR TEST REPORT

Detector Serial Number 2-132-20 Test Date 4/21/77

DETECTOR CONSTRUCTION

Type	<u>PV HgCdTe</u>	Dewar Style	<u>None</u>	S. N.	<u>--</u>
Sensitive Area	<u>0.284</u> <u>cm²</u>	Filter	<u>--</u>		
Configuration	<u>nom. 5 x 5 mm²</u>	Window: Material	<u>--</u>		
Field of View	<u>--</u> <u>Deg</u>	Window: AR Coating Pk	<u>--</u>	<u>μm</u>	
FOV Aperture: Size	<u>--</u>	Element to window	<u>--</u>		
	<u>Distance from cell</u>	distance	<u>--</u>		
	<u>--</u>				

TEST RESULTS

R (λ_p)	<u>2.2</u>	<u>amp/watt</u>
NEP (λ_p)	<u>7.9×10^{-12}</u>	<u>watt/Hz^{1/2}</u>
D* (λ_p)	<u>6.7×10^{10}</u>	<u>cm Hz^{1/2}/w</u>
D* (BB)	<u>3.8×10^9</u>	<u>cm Hz^{1/2}/w</u>
Resistance	<u>173</u>	<u>ohms</u>
Signal	<u>0.7</u>	<u>m volt</u>
Noise	<u>0.085</u>	<u>μ volt</u>
Time Constant	<u>not measured, approx. 0.1</u>	<u>μ sec (5)</u>
λ_p	<u>3.8</u>	<u>μm (4)</u>
Blackbody to Peak		
Conversion Factor	<u>17.6</u>	
Quantum Efficiency (at λ_p)	<u>54%</u>	

CONDITIONS OF MEASUREMENT

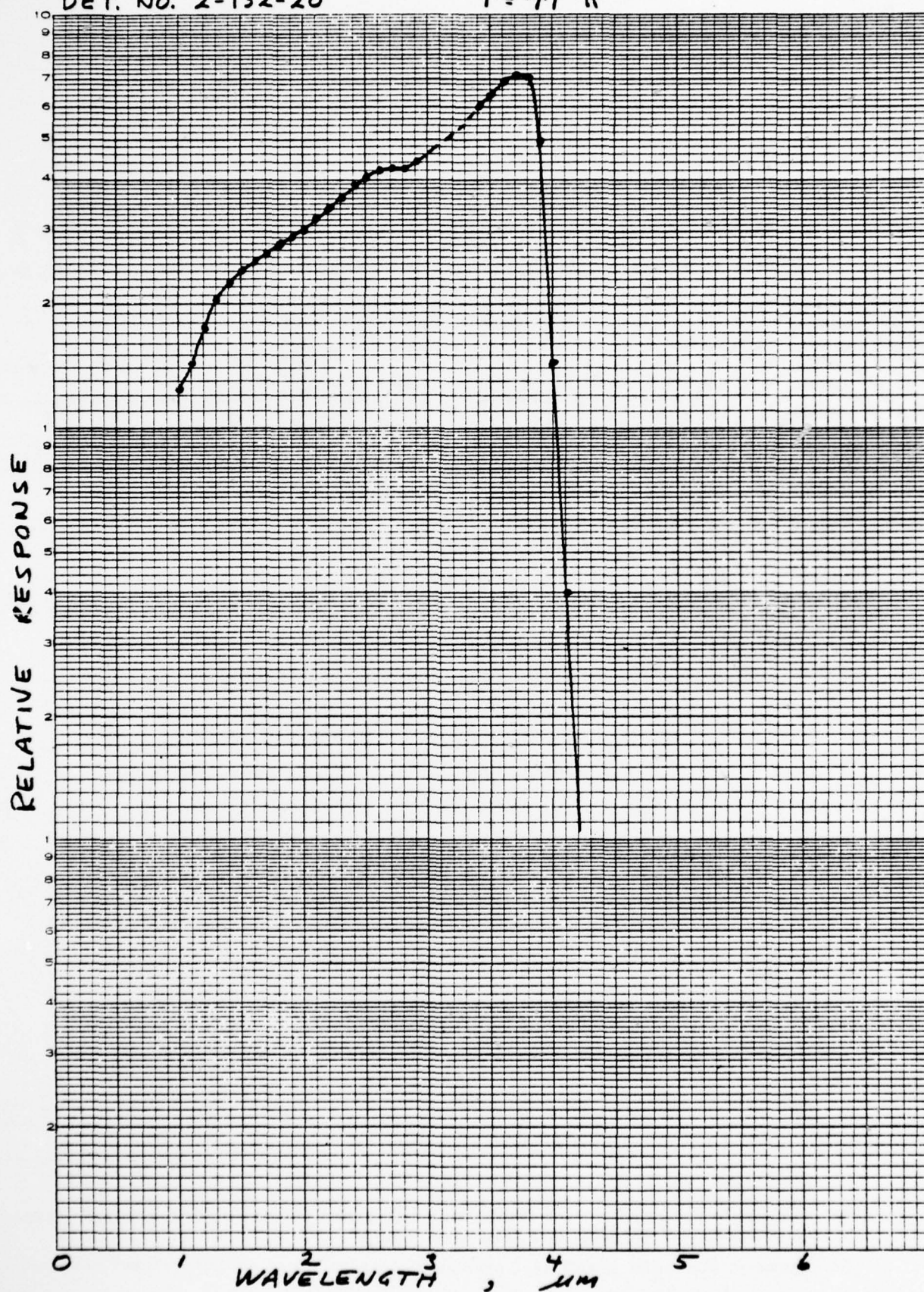
Frequency	<u>1800</u>	<u>Hertz</u>
Bandwidth	<u>6</u>	<u>Hertz</u>
BB Flux Density	<u>10</u>	<u>μw/cm²</u>
BB Temperature	<u>500</u>	<u>Deg K</u>
Detector Temp.	<u>77</u>	<u>Deg K</u>
Feedback Resistor	<u>2×10^3</u>	<u>ohms</u>
Bias Voltage	<u>0</u>	<u>volts</u>

NOTES:

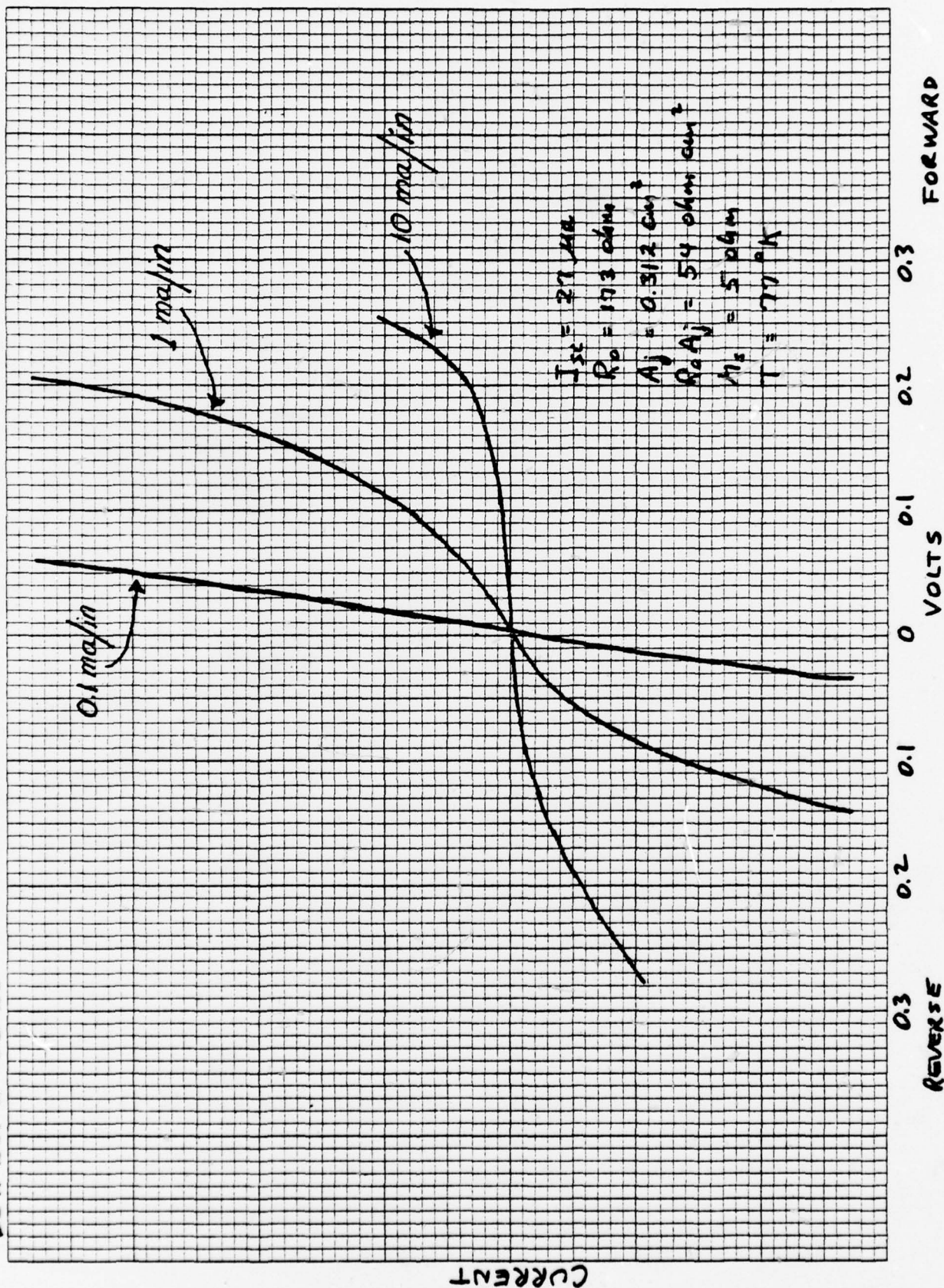
1. For all correspondence relative to this detector, please refer to SBRC W/A B214.
2. Customer U.S. Army Electronics Command, Ft. Monmouth
3. Customer's P. O. No. Contract No. DAAB07-76-C-0803
4. The BB to peak conversion factor listed is based on the relative spectral response measurements included with this data sheet.
5. Measured with SBRC Model A231 preamplifier which has a 1-kohm feedback resistor.

DET. NO. 2-132-20

$T = 77^{\circ} K$



DET. NO. 2-132-20



Santa Barbara Research Center
75 Coromar Drive
Goleta, California 93017
(805) 968-3511

DETECTOR TEST REPORT

Detector Serial Number 2-132-10-1 Test Date 10/19/76

DETECTOR CONSTRUCTION

Type PV HgCdTe
Sensitive Area 0.054 cm²
Configuration nom. 2 x 2 mm²
Field of View -- Deg
FOV Aperture: Size --
Distance from cell --

Dewar Style none S. N. --
Filter --
Window: Material --
Window: AR Coating Pk -- μm
Element to window distance --

TEST RESULTS

R (λ_p) 2.8 amp/watt
NEP (λ_p) 5.8×10^{-13} watt/Hz^{1/2}
 D^* (λ_p) 4.0×10^{11} cm Hz^{1/2}/w
 D^* (BB) 2.4×10^{10} cm Hz^{1/2}/w
Resistance 6.7×10^4 ohms
Signal 17.8 m.volt
Noise 0.80 μ volt
Time Constant 0.05 μ sec (5)
 λ_p 3.8 μm (4)
Blackbody to Peak
Conversion Factor 16.9
Quantum Efficiency (at λ_p) 91%

CONDITIONS OF MEASUREMENT

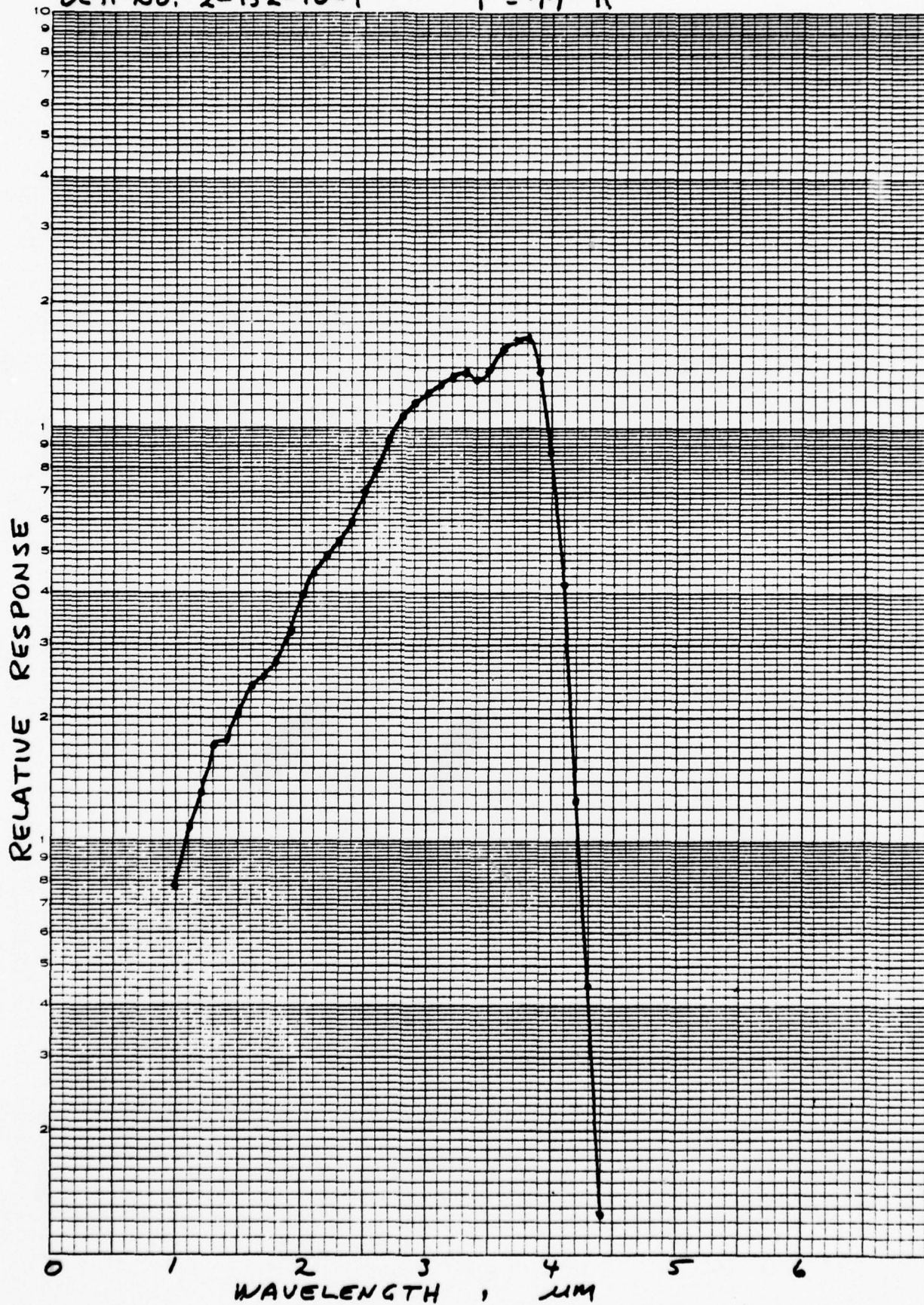
Frequency 1800 Hertz
Bandwidth 6 Hertz
BB Flux Density 10 μw/cm²
BB Temperature 500 Deg K
Detector Temp. 77 Deg K
Feedback Resistor 2×10^5 ohms
Bias Voltage 0 volts

NOTES:

1. For all correspondence relative to this detector, please refer to SBRC W/A B214.
2. Customer U.S. Army Electronics Command, Ft. Monmouth
3. Customer's P. O. No. Contract No. DAAB07-76-C-0803
4. The BB to peak conversion factor listed is based on the relative spectral response measurements included with this data sheet.
5. Measured with SBRC Model A231 preamplifier which has a 1-kohm feedback resistor.

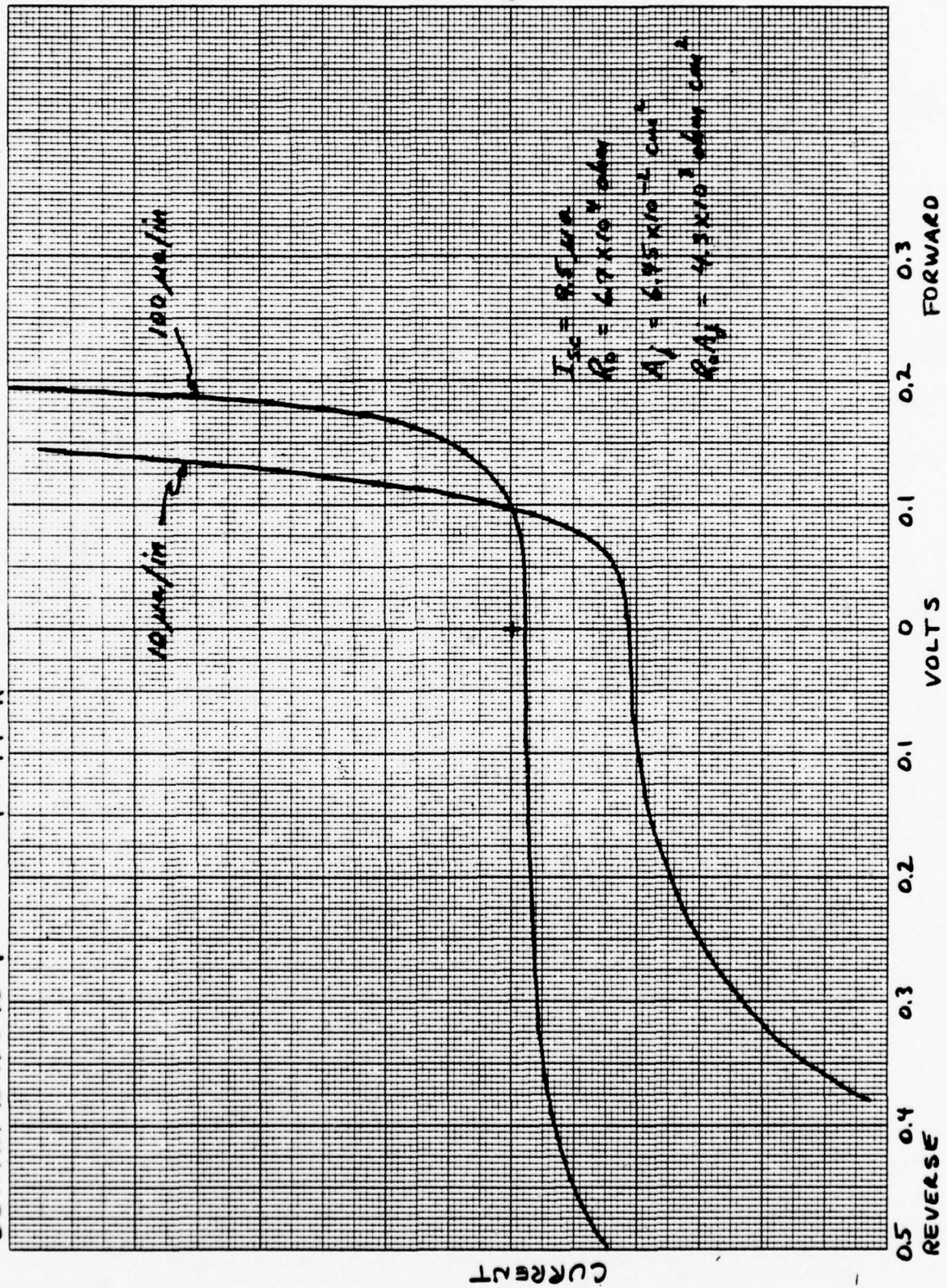
DET. NO. 2-132-10-1

$T = 77^{\circ}\text{K}$



DET. No. 2-132-10-1

T = 77°K



Santa Barbara Research Center
75 Coromar Drive
Goleta, California 93017
(805) 968-3511

DETECTOR TEST REPORT

Detector Serial Number 2-132-10-2 Test Date 10/19/76

DETECTOR CONSTRUCTION

Type	<u>PV HgCdTe</u>	Dewar Style	<u>None</u> S. N. <u>--</u>
Sensitive Area	<u>0.054</u> <u>cm²</u>	Filter	<u>--</u>
Configuration	<u>nom. 2 x 2 mm²</u>	Window: Material	<u>--</u>
Field of View	<u>--</u> <u>Deg</u>	Window: AR Coating Pk	<u>--</u> <u>μm</u>
FOV Aperture: Size	<u>--</u>	Element to window	<u>--</u>
Distance from cell	<u>--</u>	distance	<u>--</u>

TEST RESULTS

R (λ_p)	<u>3.0</u> <u>amp/watt</u>
NEP (λ_p)	<u>8.3×10^{-13}</u> <u>watt/Hz^{1/2}</u>
D* (λ_p)	<u>2.8×10^{11}</u> <u>cm Hz^{1/2}/w</u>
D* (BB)	<u>1.8×10^{10}</u> <u>cm Hz^{1/2}/w</u>
Resistance	<u>4.3×10^4</u> <u>ohms</u>
Signal	<u>20</u> <u>m volt</u>
Noise	<u>0.60</u> <u>μ volt</u>
Time Constant	<u>0.05</u> <u>μ sec (5)</u>
λ_p	<u>4.0</u> <u>μm (4)</u>
Blackbody to Peak	
Conversion Factor	<u>16.0</u>
Quantum Efficiency (at λ_p)	<u>92%</u>

CONDITIONS OF MEASUREMENT

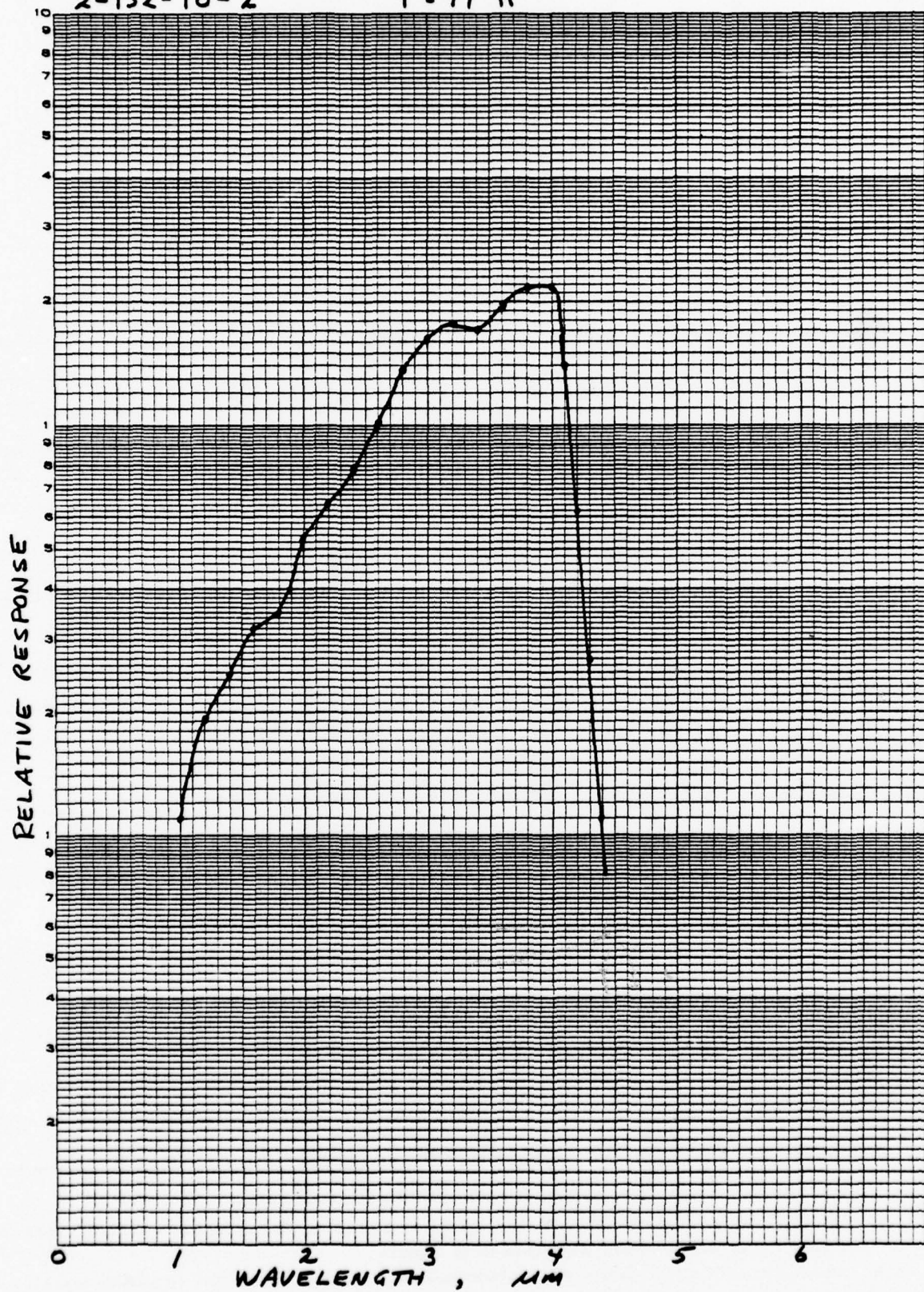
Frequency	<u>1800</u> <u>Hertz</u>
Bandwidth	<u>6</u> <u>Hertz</u>
BB Flux Density	<u>10</u> <u>μw/cm²</u>
BB Temperature	<u>500</u> <u>Deg K</u>
Detector Temp.	<u>77</u> <u>Deg K</u>
Feedback Resistor	<u>2×10^5</u> <u>ohms</u>
Bias Voltage	<u>0</u> <u>volts</u>

NOTES:

1. For all correspondence relative to this detector, please refer to SBRC W/A B214.
2. Customer U.S. Army Electronics Command; Ft. Monmouth
3. Customer's P. O. No. Contract No. DAAB07-76-C-0803
4. The BB to peak conversion factor listed is based on the relative spectral response measurements included with this data sheet.
5. Measured with SBRC Model A231 preamplifier which has a 1-kohm feedback resistor.

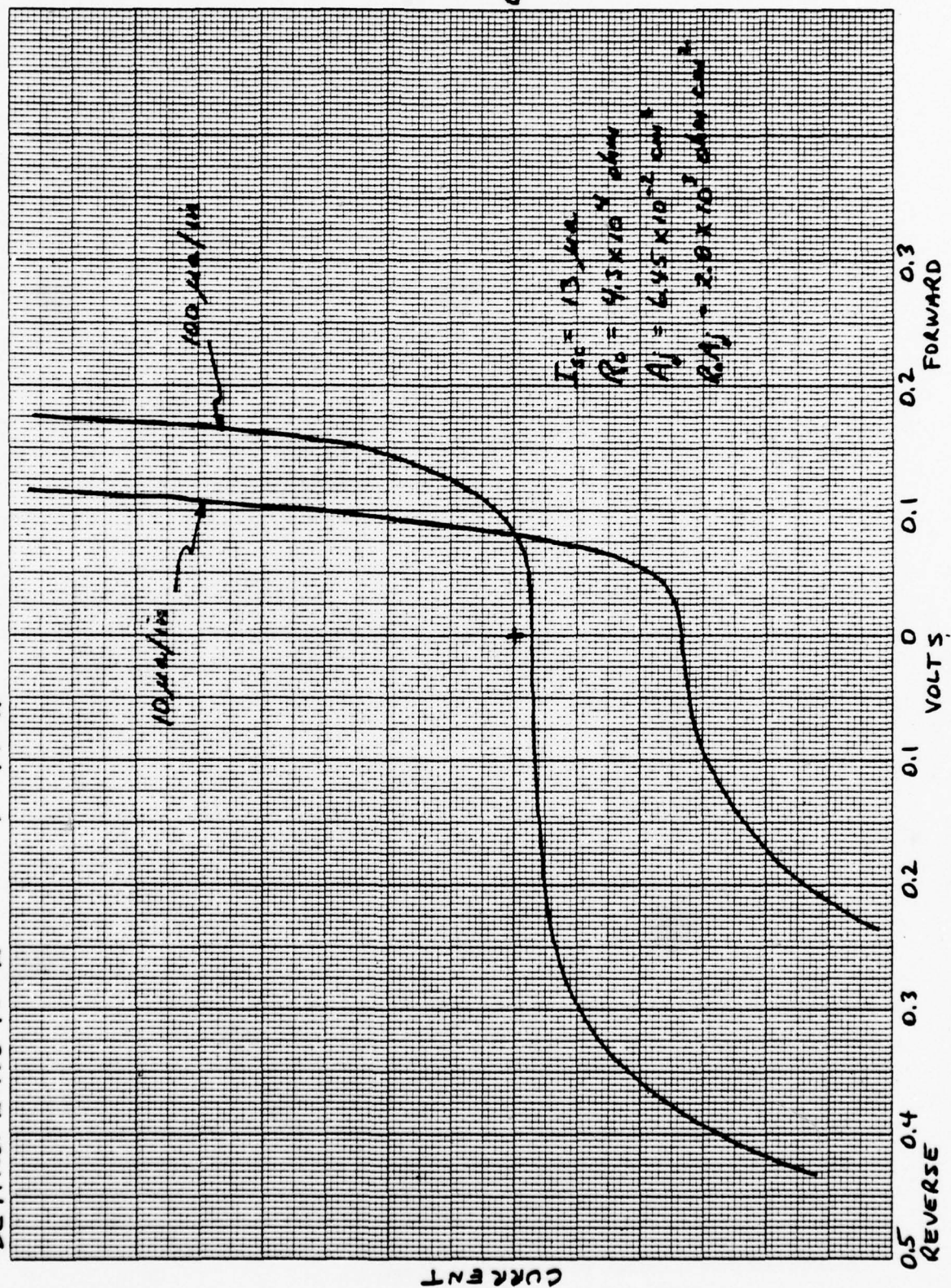
2-132-10-2

T = 77°K



T = 77°K

DET. NO. 2-132-10-2



Santa Barbara Research Center
75 Coromar Drive
Goleta, California 93017
(805) 968-3511

DETECTOR TEST REPORT

Detector Serial Number RC4-2K-L Test Date 4/25/77

DETECTOR CONSTRUCTION

Type	<u>PV HgCdTe</u>	Dewar Style	<u>—</u>	S. N.	<u>—</u>
Sensitive Area	<u>0.054</u>	cm ²	Filter	<u>—</u>	
Configuration	<u>nom. 2 x 2 mm²</u>	Window: Material	<u>—</u>		
Field of View	<u>—</u>	Deg	Window: AR Coating Pk	<u>—</u>	<u>μm</u>
FOV Aperture: Size	<u>—</u>		Element to window	<u>—</u>	
	Distance from cell		distance	<u>—</u>	
	<u>—</u>				

TEST RESULTS

R (λ_p)	<u>0.82</u>	amp/watt
NEP (λ_p)	<u>8.6×10^{-13}</u>	watt/Hz ^{$\frac{1}{2}$}
D* (λ_p)	<u>2.7×10^{11}</u>	cm Hz ^{$\frac{1}{2}$} /w
D* (BB)	<u>3.9×10^8</u>	cm Hz ^{$\frac{1}{2}$} /w
Resistance	<u>2.3×10^4</u>	ohms
Signal	<u>645</u>	μ volt
Noise	<u>1.75</u>	μ volt
Time Constant	<u>0.25</u>	μ sec (5)
λ_p	<u>2.2</u>	μm (4)
Blackbody to Peak		
Conversion Factor	<u>6.9×10^2</u>	
Quantum Efficiency (at λ_p)	<u>46%</u>	

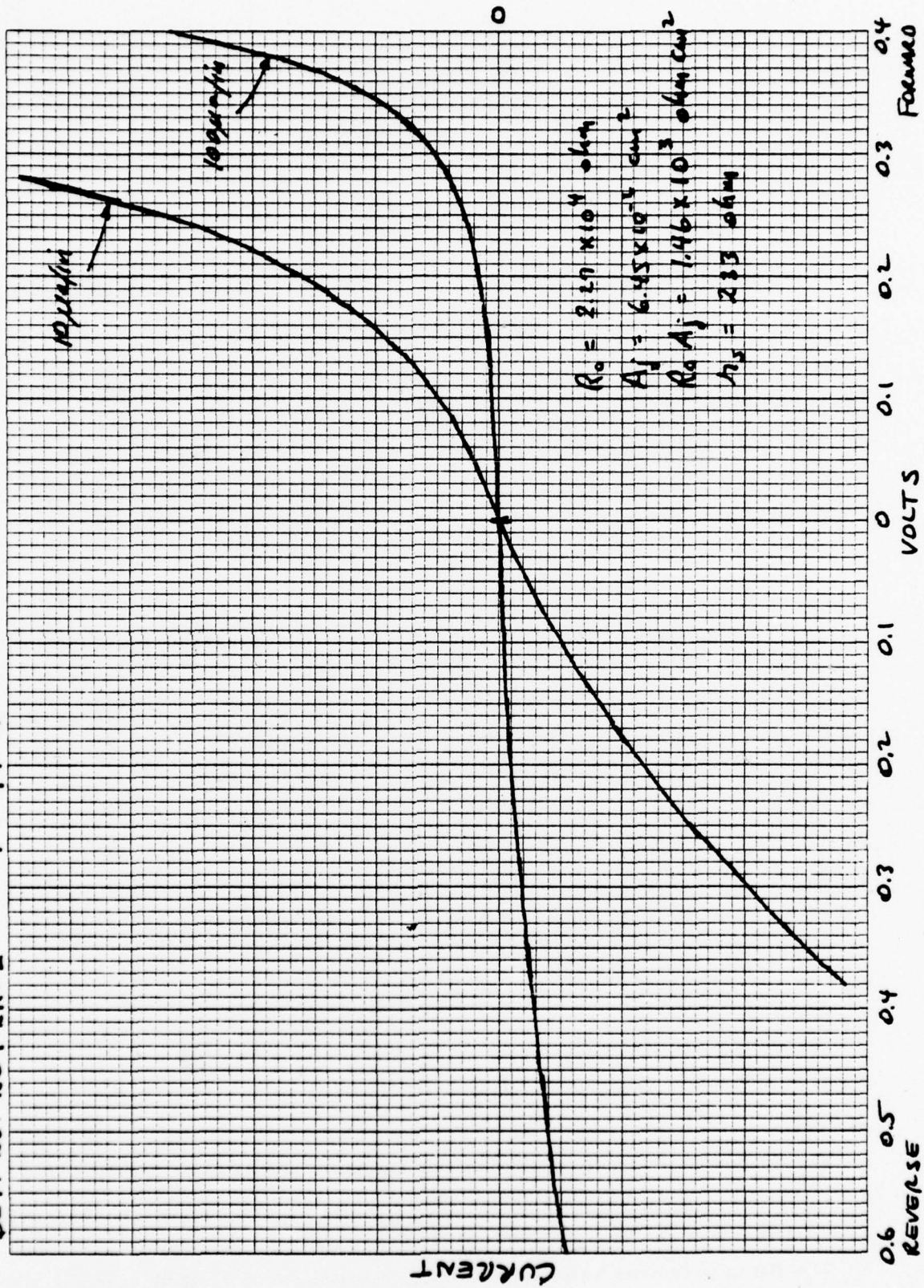
CONDITIONS OF MEASUREMENT

Frequency	<u>1800</u>	Hertz
Bandwidth	<u>6</u>	Hertz
BB Flux Density	<u>10</u>	μw/cm ²
BB Temperature	<u>500</u>	Deg K
Detector Temp.	<u>77</u>	Deg K
Feedback Resistor	<u>10^6</u>	ohms
Bias Voltage	<u>0</u>	volts

NOTES:

1. For all correspondence relative to this detector, please refer to SBRC W/A B214.
2. Customer U.S. Army Electronics Command, Ft. Monmouth, New Jersey
3. Customer's P. O. No. Contract No. DAAB07-76-C-0803
4. The BB to peak conversion factor listed is based on the relative spectral response measurements included with this data sheet.
5. Measured with SBRC Model A231 preamplifier which has a 1-kohm feedback resistor.

DET. NO. RC4-2K-L $T = 77^{\circ}K$



Santa Barbara Research Center
75 Coronar Drive
Goleta, California 93017
(805) 968-3511

DETECTOR TEST REPORT

Detector Serial Number RC4-2K-L Test Date 4/25/77

DETECTOR CONSTRUCTION

Type <u>PV HgCdTe</u>	Dewar Style <u>--</u> S. N. <u>--</u>
Sensitive Area <u>0.054</u> <u>cm²</u>	Filter <u>--</u>
Configuration <u>nom. 2 x 2 mm²</u>	Window: Material <u>--</u>
Field of View <u>--</u> <u>Deg</u>	Window: AR Coating Pk <u>--</u> <u>μm</u>
FOV Aperture: Size <u>--</u>	Element to window
Distance from cell <u>--</u>	distance <u>--</u>

TEST RESULTS

R (λ_p)	<u>1.20</u>	<u>amp/watt</u>
NEP (λ_p)	<u>1.2×10^{-12}</u>	<u>watt/Hz^{1/2}</u>
D* (λ_p)	<u>1.9×10^{11}</u>	<u>cm Hz^{1/2}/w</u>
D* (BB)	<u>2.1×10^8</u>	<u>cm Hz^{1/2}/w</u>
Resistance	<u>1.2×10^4</u>	<u>ohms</u>
Signal	<u>36</u>	<u>μ volt</u>
Noise	<u>0.185</u>	<u>μ volt</u>
Time Constant	<u>0.28</u>	<u>μ sec (5)</u>
λ_p	<u>2.2</u>	<u>μm (4)</u>
Blackbody to Peak		
Conversion Factor	<u>9.0×10^2</u>	
Quantum Efficiency (at λ_p)	<u>68%</u>	

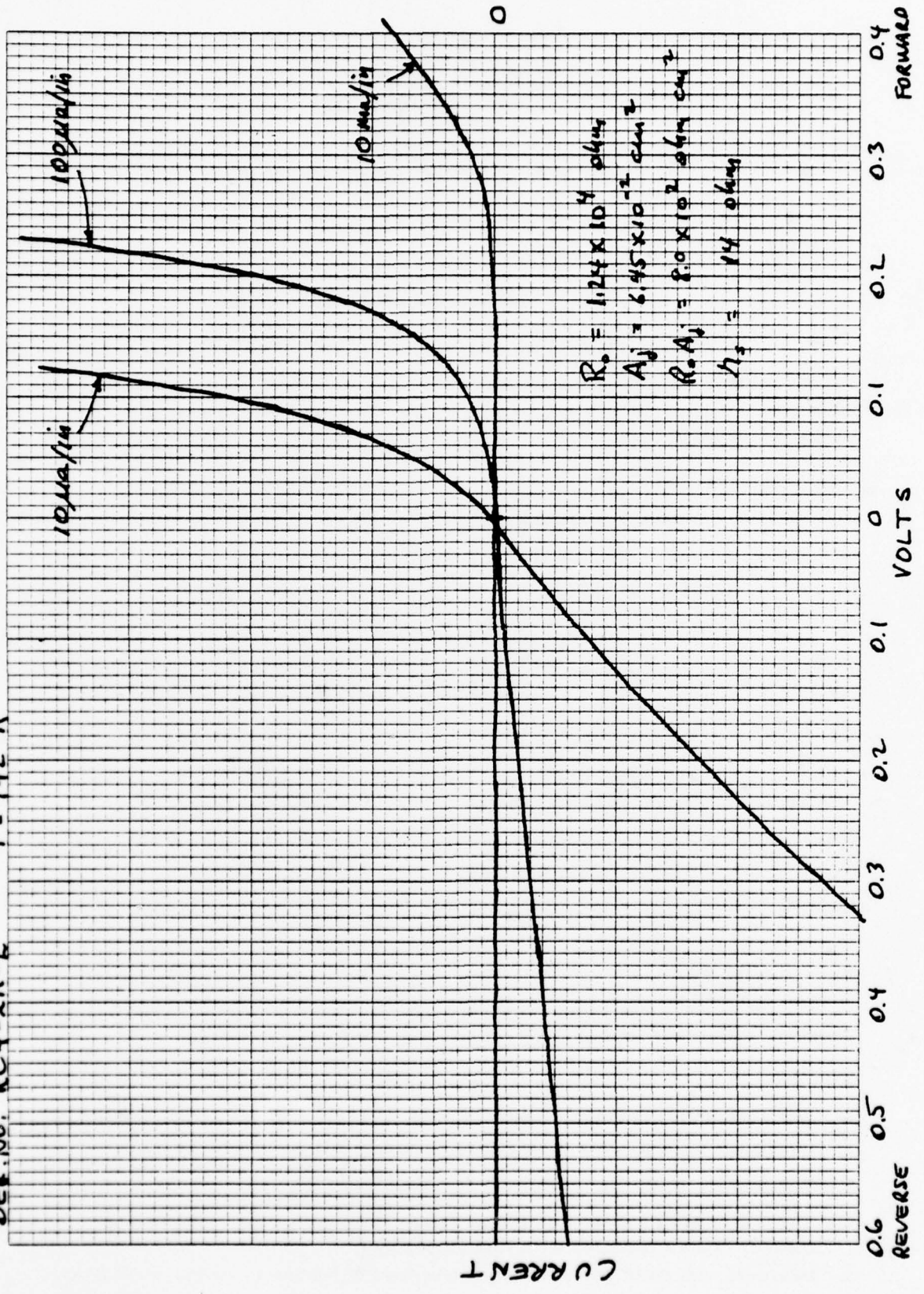
CONDITIONS OF MEASUREMENT

Frequency	<u>1800</u>	<u>Hertz</u>
Bandwidth	<u>6</u>	<u>Hertz</u>
BB Flux Density	<u>10</u>	<u>μw/cm²</u>
BB Temperature	<u>500</u>	<u>Deg K</u>
Detector Temp.	<u>192</u>	<u>Deg K</u>
Feedback Resistor	<u>5×10^4</u>	<u>ohms</u>
Bias Voltage	<u>0</u>	<u>volts</u>

NOTES:

1. For all correspondence relative to this detector, please refer to SBRC W/A B214.
2. Customer U.S. Army Electronics Command, Ft. Monmouth
3. Customer's P. O. No. Contract No.DAAB07-76-C-0803
4. The BB to peak conversion factor listed is based on the relative spectral response measurements included with this data sheet.
5. Measured with SBRC Model A231 preamplifier which has a 1-kohm feedback resistor.

DET. NO. RC4-2K-L T = 192° K



Santa Barbara Research Center
75 Coromar Drive
Goleta, California 93017
(805) 968-3511

DETECTOR TEST REPORT

Detector Serial Number RC4-2K-R Test Date 4/25/77

DETECTOR CONSTRUCTION

Type	<u>PV HgCdTe</u>	Dewar Style	<u>--</u>	S. N.	<u>--</u>
Sensitive Area	<u>0.054</u> <u>cm²</u>	Filter	<u>--</u>		
Configuration	<u>nom. 2 x 2 mm²</u>	Window: Material	<u>--</u>		
Field of View	<u>--</u> <u>Deg</u>	Window: AR Coating Pk	<u>--</u>	<u>μm</u>	
FOV Aperture: Size	<u>--</u>	Element to window	<u>--</u>		
Distance from cell	<u>--</u>	distance	<u>--</u>		

TEST RESULTS

R (λ_p)	<u>0.76</u>	<u>amp/watt</u>
NEP (λ_p)	<u>9.8×10^{-13}</u>	<u>watt/Hz^{1/2}</u>
D* (λ_p)	<u>2.4×10^{11}</u>	<u>cm Hz^{1/2}/w</u>
D* (BB)	<u>3.4×10^8</u>	<u>cm Hz^{1/2}/w</u>
Resistance	<u>2.4×10^4</u>	<u>ohms</u>
Signal	<u>595</u>	<u>μ volt</u>
Noise	<u>1.85</u>	<u>μ volt</u>
Time Constant	<u>0.27</u>	<u>μ sec (5)</u>
λ_p	<u>2.2</u>	<u>μm (4)</u>
Blackbody to Peak		
Conversion Factor	<u>6.9×10^2</u>	
Quantum Efficiency (at λ_p)	<u>43%</u>	

CONDITIONS OF MEASUREMENT

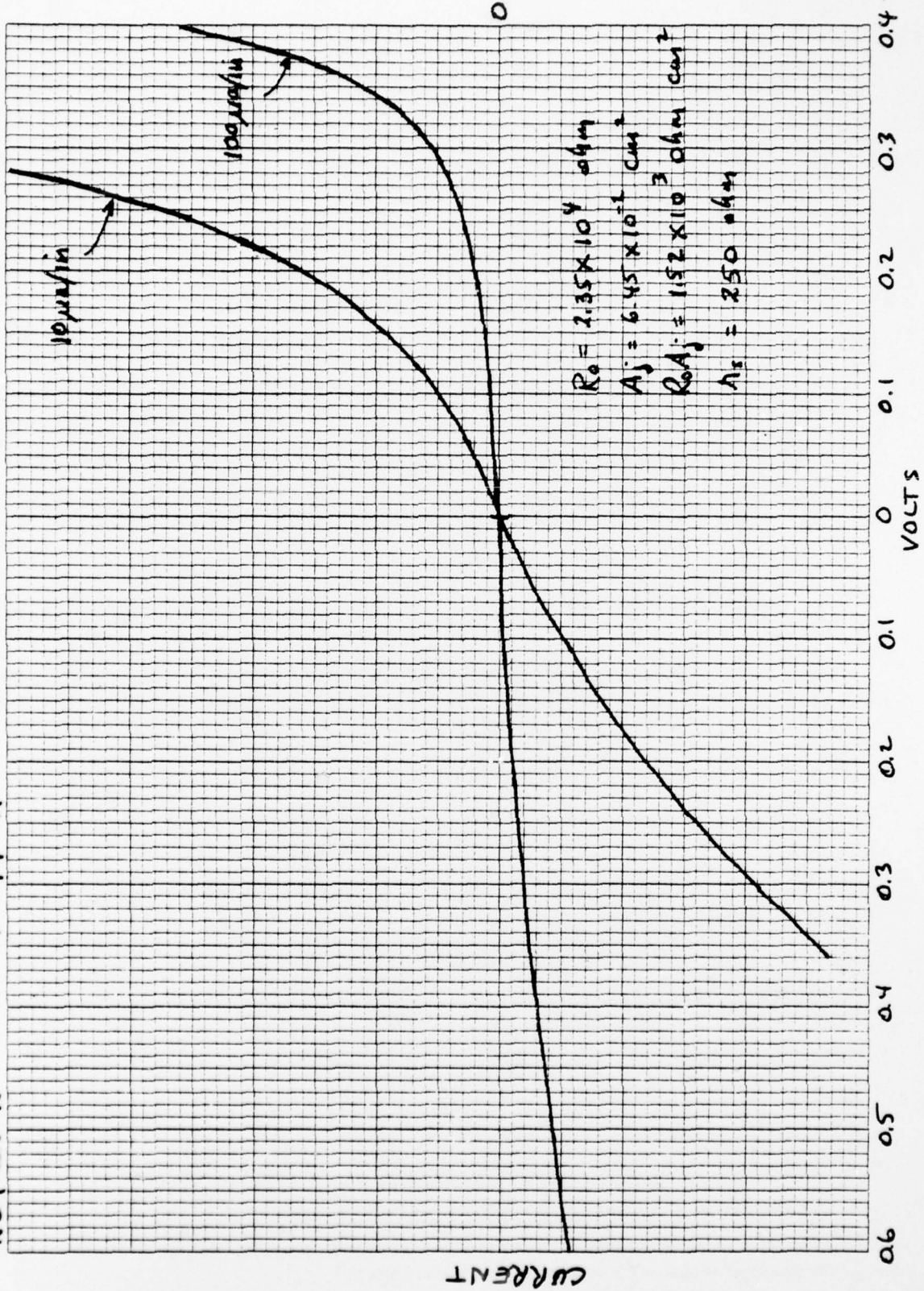
Frequency	<u>1800</u>	<u>Hertz</u>
Bandwidth	<u>6</u>	<u>Hertz</u>
BB Flux Density	<u>10</u>	<u>μw/cm²</u>
BB Temperature	<u>500</u>	<u>Deg K</u>
Detector Temp.	<u>77</u>	<u>Deg K</u>
Feedback Resistor	<u>10^6</u>	<u>ohms</u>
Bias Voltage	<u>0</u>	<u>volts</u>

NOTES:

1. For all correspondence relative to this detector, please refer to SBRC W/A B214.
2. Customer U.S. Army Electronics Command, Fort Monmouth, New Jersey
3. Customer's P. O. No. Contract No. DAAB07-76-C-0803
4. The BB to peak conversion factor listed is based on the relative spectral response measurements included with this data sheet.
5. Measured with SBRC Model A231 preamplifier which has a 1-kohm feedback resistor.

RC4-2K-R

$T = 77^{\circ}\text{K}$



Santa Barbara Research Center
75 Coromar Drive
Goleta, California 93017
(805) 968-3511

DETECTOR TEST REPORT

Detector Serial Number RC4-2K-R Test Date 4/25/77

DETECTOR CONSTRUCTION

Type	<u>PV HgCdTe</u>	Dewar Style	<u>--</u>	S. N.	<u>--</u>
Sensitive Area	<u>0.054</u> <u>cm²</u>	Filter	<u>--</u>		
Configuration	<u>nom. 2 x 2 mm²</u>	Window: Material	<u>--</u>		
Field of View	<u>--</u> <u>Deg</u>	Window: AR Coating Pk	<u>--</u>	<u>μm</u>	
FOV Aperture: Size	<u>--</u>	Element to window	<u>--</u>		
	<u>Distance from cell</u>	distance	<u>--</u>		
	<u>--</u>				

TEST RESULTS

$R(\lambda_p)$	<u>1.18</u>	<u>amp/watt</u>
NEP (λ_p)	<u>2.7×10^{-12}</u>	<u>watt/Hz^{1/2}</u>
$D^*(\lambda_p)$	<u>8.5×10^{10}</u>	<u>cm Hz^{1/2}/w</u>
$D^*(BB)$	<u>9.4×10^7</u>	<u>cm Hz^{1/2}/w</u>
Resistance	<u>3.6×10^3</u>	<u>ohms</u>
Signal	<u>35.5</u>	<u>μ volt</u>
Noise	<u>0.40</u>	<u>μ volt</u>
Time Constant	<u>0.30</u>	<u>μ sec (5)</u>
λ_p	<u>2.2</u>	<u>μm (4)</u>
Blackbody to Peak		
Conversion Factor	<u>9.0×10^2</u>	
Quantum Efficiency (at λ_p)	<u>67%</u>	

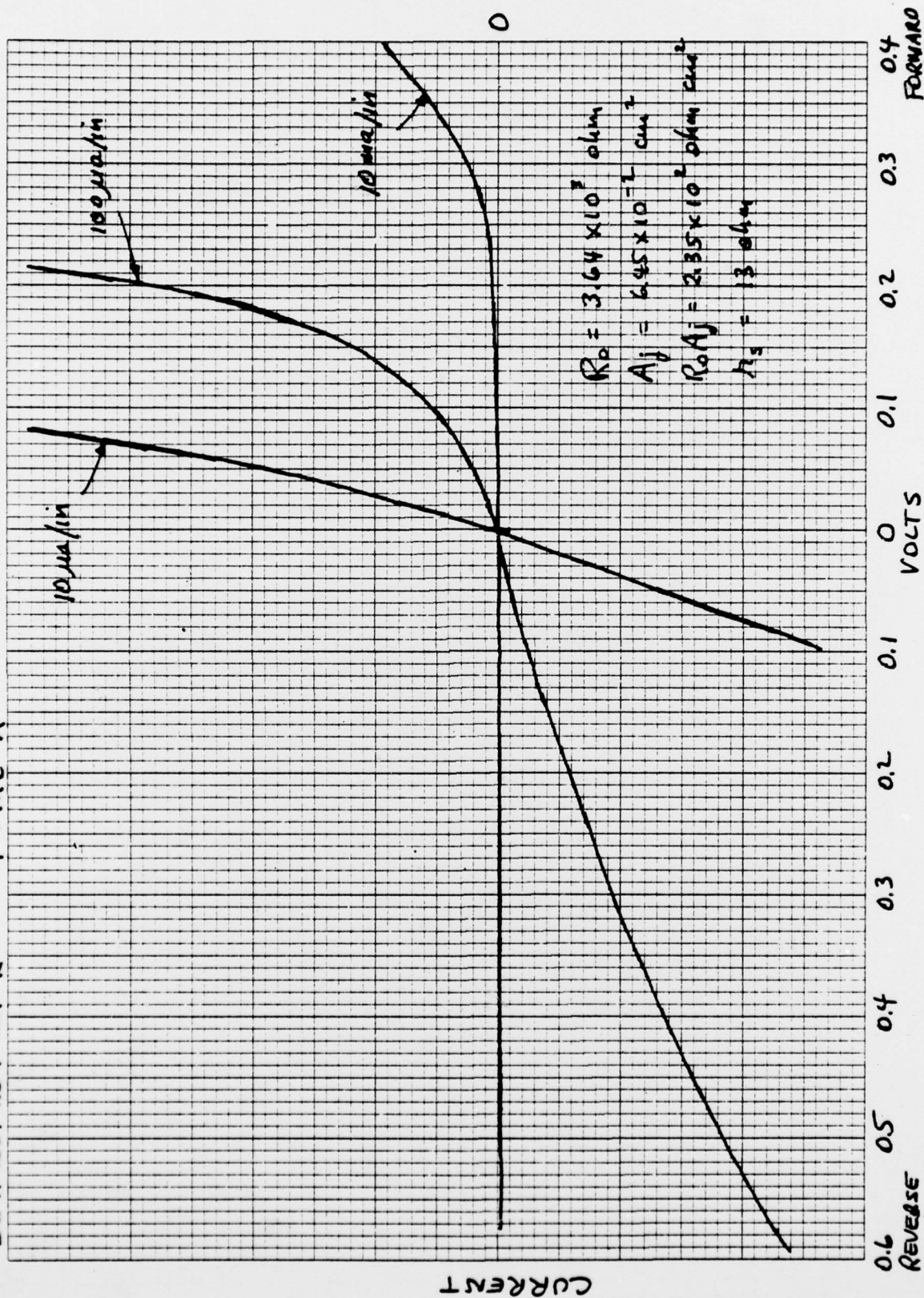
CONDITIONS OF MEASUREMENT

Frequency	<u>1800</u>	<u>Hertz</u>
Bandwidth	<u>6</u>	<u>Hertz</u>
BB Flux Density	<u>10</u>	<u>μw/cm²</u>
BB Temperature	<u>500</u>	<u>Deg K</u>
Detector Temp.	<u>192</u>	<u>Deg K</u>
Feedback Resistor	<u>5×10^4</u>	<u>ohms</u>
Bias Voltage	<u>0</u>	<u>volts</u>

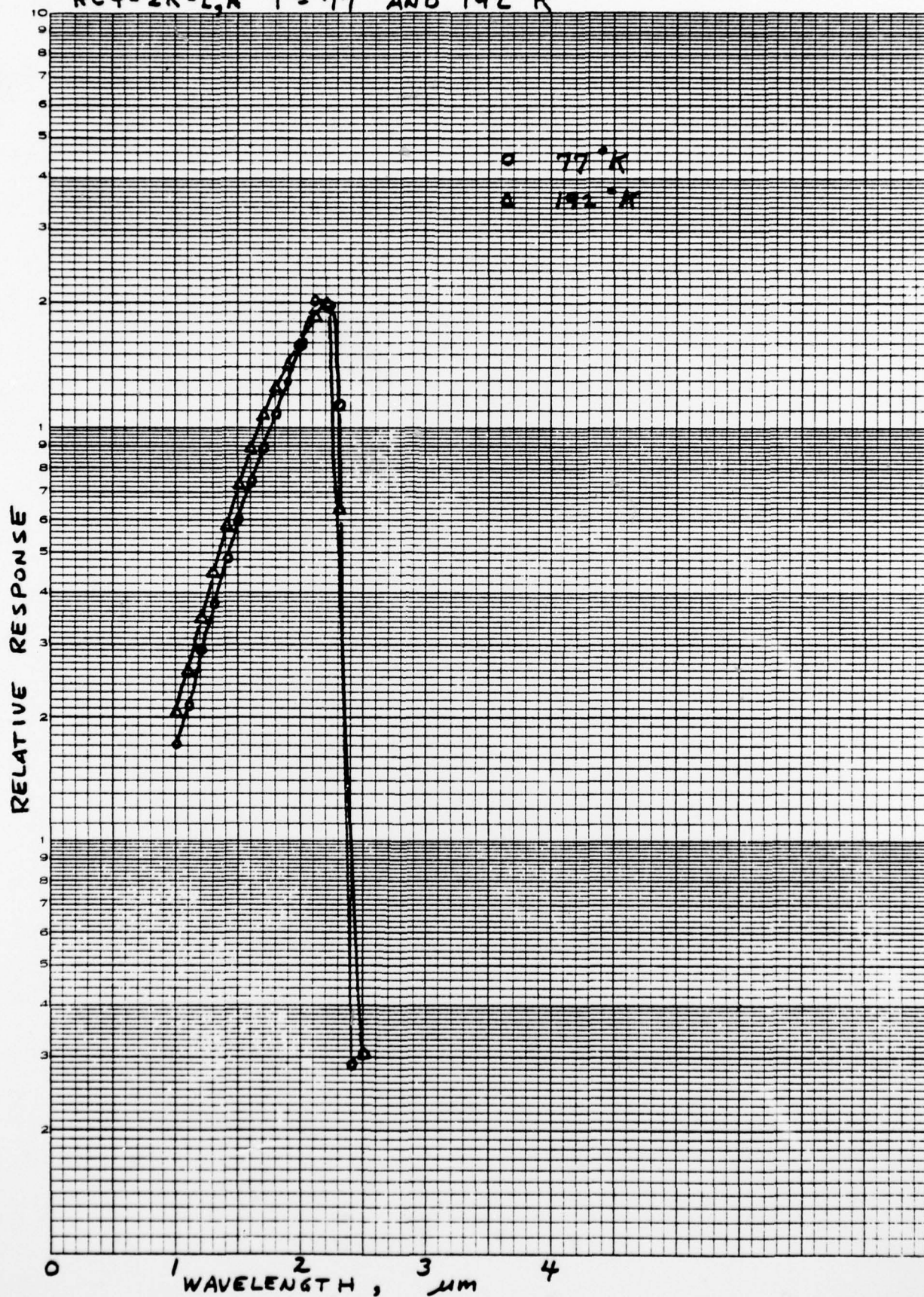
NOTES:

1. For all correspondence relative to this detector, please refer to SBRC W/A B214.
2. Customer U.S. Army Electronics Command, Ft. Monmouth, New Jersey
3. Customer's P. O. No. Contract No. DAAB07-76-C-0803
4. The BB to peak conversion factor listed is based on the relative spectral response measurements included with this data sheet.
5. Measured with SBRC Model A231 preamplifier which has a 1-kohm feedback resistor.

DET. NO. RC4-2K-R T = 192 °K



RC4-2K-L,R T = 77° AND 192° K



Section 8

CONCLUSIONS AND RECOMMENDATIONS

CONCLUSIONS

During the course of this program, a greater effort was expended in the development of the 3.85- μm large-area detectors; therefore, the results are more substantial for these devices than for the 2.06- μm detectors. However, the techniques developed for 3.85- μm detectors are also directly applicable to 2.06- μm detectors. It may be concluded that, given an appropriate additional effort, any result achieved with the 3.85- μm detectors could, therefore, be achieved with 2.06- μm detectors. One qualification of this statement should be made concerning crystal growth. The $x = 0.48$ material required for 2.06- μm detectors is undoubtedly more difficult to prepare than the $x = 0.32$ material required for 3.85- μm detectors. Therefore, the yield and perfection of $x = 0.48$ material will generally be expected to be inferior to that of $x = 0.32$ material. Nevertheless, the work done on this program has indicated that the quality of $x = 0.48$ material is adequate to fabricate 2.06- μm detectors up to $5 \times 5 \text{ mm}^2$ in sensitive area.

The major conclusions to be drawn from this program are listed below, with those applying to 3.85- μm detectors given first.

3.85- μm Detectors

1) Three crystal growth methods were evaluated for the preparation of $x = 0.32$ material. These were zone melting, solid-state recrystallization, and pressure-controlled recrystallization. It was found that the zone melting method produced the best quality material for large area detectors.

2) A junction fabrication technique was successfully developed for $n^+ - p$ one-sided step junctions. A lightly doped p-side was obtained by diffusion of Au into HgCdTe wafers; the heavy n-side was formed by B^+ ion implantation.

3) The ion-implantation technique was found to be well-suited to the formation of large area p-n junctions because 1) good junction planarity is maintained, 2) the implanted ion concentration is easily controlled, 3) the junction depth below the top surface is accurately defined, 4) shallow junctions can be achieved, and 5) no high temperature annealing is required for n-type implants.

4) Ion-implantation produces a significant amount of lattice damage which has an n-type character. The damage doping may be on the order of 10 times the chemical doping of the implanted specie. It is not necessary to anneal out the damage to achieve good diode characteristics.

5) Degenerate dopings on the n-side cause this region to be nearly transparent to photons at the wavelength of interest (3.85 μm). Photons are therefore absorbed primarily on the p-side where they create minority electrons which, because of their long diffusion length, are efficiently collected at the junction.

6) Large-area photovoltaic detectors up to $5 \times 5 \text{ mm}^2$ (nominal area) were successfully fabricated and assembled into quadrant arrays.

7) Low junction capacitance was achieved by the combination of the low p-side doping and some compensation from implanted donor centers. Capacitance-voltage measurements indicated net acceptor concentrations in the vicinity of the junction of about $3 \times 10^{14} \text{ cm}^{-3}$ and a zero bias junction capacitance of 150 pf/mm^2 .

8) Photovoltaic detectors for 3.85 μm achieved BLIP limited detectivities of about $3 \times 10^{11} \text{ cm Hz}^{\frac{1}{2}}/\text{watt}$ for low-frequency operation at 77°K with an optimum preamplifier. The measured quantum efficiencies were quite high, in the range of 70 - 90%.

9) Because of the low junction capacitance, good high-frequency performance was obtained for $5 \times 5 \text{ mm}^2$ detectors. Typical detectivity was $6 \times 10^{10} \text{ cm Hz}^{\frac{1}{2}}/\text{watt}$ at 1 MHz for 77°K operation with an optimum preamplifier. Typical detector-preamplifier response times were 100 to 200 nsec.

10) Operation of 3.85- μm detectors at TE cooler temperatures (i. e., 170°K or above) will significantly degrade the detectivity. The measured degradation was between one and two orders of magnitude.

2.06- μm Detectors

1) The same three crystal growth methods were evaluated for the preparation of $x = 0.48$ material. It was found that either the zone melt or solid-state recrystallization methods produced acceptable material. The pressure-controlled recrystallization method yielded material with undesirable compositional nonuniformities.

2) The B^+ ion implantation technique for junction formation was successfully applied to make 2.06- μm detectors.

3) The base acceptor doping concentrations achieved were higher than desired and were $\approx 2 \times 10^{16} \text{ cm}^{-3}$. Therefore, the zero bias junction capacitance was also higher than desired, being $\approx 500 \text{ pf/mm}^2$. The cause of this high base acceptor doping is known and can be corrected in further work.

4) Large area 2.06- μm detectors were fabricated up to $2 \times 2 \text{ mm}^2$ in size with good detectivity and uniformity. The material quality appears to be adequate to make $5 \times 5 \text{ mm}^2$ detectors; however, this was not actually demonstrated during the course of the program.

5) Photovoltaic detectors for 2.06 μm achieved detectivities in the $2 \text{ to } 8 \times 10^{11} \text{ cm Hz}^{\frac{1}{2}}/\text{watt}$ range for low-frequency operation at 77°K. These detectors were neither BLIP limited nor detector thermal noise limited. The dominant noise appeared to be in the amplifier used for detectivity measurements.

6) These detectors could be operated at 192°K with some loss in low-frequency detectivity, on the order of a factor of 2.

7) The high-frequency detectivity of these 2.06- μm detectors is inferior to that of the 3.85- μm detectors because of the higher junction capacitance. Means to reduce the junction capacitance are known and could be implemented in some future program.

RECOMMENDATIONS FOR FUTURE WORK

The work accomplished on this program has demonstrated the feasibility of making large area (i. e., $5 \times 5 \text{ mm}^2$) PV HgCdTe detectors for wavelengths of $3.85 \mu\text{m}$ and $2.06 \mu\text{m}$. Crystals grown by either the zone melt or the solid-state recrystallization method were shown to provide large enough single-crystal regions with adequate compositional uniformity. The B^+ ion implantation method demonstrated uniform p-n junctions over the large areas.

Being of an exploratory development nature, the present program could not properly address all the problem areas which were identified. The purpose of this concluding section is to discuss these findings and provide recommendations for possible future work. In addition, recommendations are made concerning the possibility of further improvement in high-frequency performance and suggestions for an engineering development program designed to improve the producibility of large area quadrant arrays.

High Junction Capacitance in $2.06\text{-}\mu\text{m}$ Detectors

The problem of high junction capacitance in the $2.06\text{-}\mu\text{m}$ detectors has already been mentioned and the cause has been identified with an excessive acceptor concentration in the base region. Concentrations of about $2 \times 10^{16} \text{ cm}^{-3}$ were deduced from diode C-V analysis.

It is believed that base acceptor concentrations can be reduced by about two orders of magnitude with a consequent reduction in junction capacitance of one order of magnitude. It is recommended that, instead of an Au diffusion to provide base acceptor doping, an Hg in-diffusion should be done on as-grown p-type material to reduce the Hg vacancy content down to the low 10^{14} cm^{-3} range. An n-on-p junction would then be made by the standard B^+ implantation process. A series of annealing runs would have to be made on a given HgCdTe crystal to determine the optimum anneal temperature and Hg pressure to accomplish this goal. Also, high purity zone melted HgCdTe should be used to mitigate possible complications due to compensating donor impurities.

Since this Hg in-diffusion will not penetrate very far into the base wafer, one will wind up with an $n^+ - p - p^+$ structure. This structure is actually quite desirable, since the p^+ base region serves to decrease series resistance, while the lightly p-type region provides low junction capacitance.

Anomalous Response Time

Another problem area previously mentioned is the anomalously long detector response times as measured with a GaAs laser diode compared with the calculated junction RC time. Recall that the measured response times were roughly a factor of two greater than expected from junction capacitance values. An hypothesis was offered which attributed this problem to optical excitation of charge carriers into deep states in the depletion region thereby inducing an extra amount of fixed charge. This extra fixed charge effectively decreases the width of the depletion region and, hence, increases capacitance.

Further investigations should be conducted to elucidate this particular behavior. If this hypothesis becomes reality, it could turn out that little can be done to remove the deep states and eliminate the effect. On the other hand, if deep states are created by ion-implantation damage, then it may be possible to remove them by a suitable annealing operation. Since a reduction of junction capacitance by a factor of two is at stake, it seems worthwhile to spend an additional effort on this problem.

Optimization for TE Cooler Operation

Additional work is recommended on optimizing large area detector performance at elevated temperatures, namely those which can be achieved with TE coolers. This would greatly simplify the deployment of such detectors in military systems. The use of LN_2 for detector cooling was used in the present program as an expedient for meeting program design goals, but objections to the use of LN_2 cooling for operational systems have sometimes been expressed because of logistics problems.

The primary cause for degradation of the sensitivity of a PV HgCdTe detector at elevated temperatures is an increase in the saturation current produced by diffusion of minority carriers to the p-n junction. As temperature

is increased, the minority carrier generation rate increases, leading to a higher diffusion current. This higher current flow across the p-n junction produces higher noise, thereby decreasing detector sensitivity.

Theoretical calculations indicate that most of the diffusion current originates in the p-type base region of the PV detector. In conventional detector designs, this base region is considerably thicker than necessary. Thus, a reduction in base thickness could conceivably lead to a reduction in the volume from which the minority carriers originate with a consequent reduction in diffusion current. It may be shown that the general equation for base region minority carrier diffusion current density J_d is

$$J_d = \frac{eD_n n_0}{L_n} \left[\frac{(D_n/L_n) \tanh(d/L_n) + s}{(D_n/L_n) + s \tanh(d/L_n)} \right] \quad (52)$$

where $D_n = \mu_n \frac{kT}{e}$ = electron diffusion coefficient

$L_n = (D_n \tau_n)^{\frac{1}{2}}$ = electron diffusion length

μ_n = electron mobility

τ_n = electron lifetime

n_0 = equilibrium electron concentration in base region

d = thickness of base region

s = surface recombination velocity

e = electronic charge

k = Boltzmann's constant

T = absolute temperature

A better understanding of the significance of this equation can be had by considering some special cases.

Case 1. $d \gg L_n$

In this case, $\tanh(d/L_n) \approx 1$ and

$$J_d \approx \frac{eD_n n_0}{L_n} \quad (53)$$

This is the equation for electron diffusion current for a thick base PV detector and is an expression we are more familiar with.

Case 2. $s = 0$

In this case

$$J_d = \frac{eD_n n_o}{L_n} [\tanh (d/L_n)] \quad (54)$$

Case 3. $s = \infty$

$$J_d = \frac{eD_n n_o}{L_n} [\tanh (d/L_n)]^{-1} \quad (55)$$

We see that Case 2 is the most interesting possibility. If conditions can be arranged such that $d \ll L_n$ and s is small, then the diffusion current can be substantially reduced from the thick base value. Detailed calculations show that substantial reductions in diffusion current may be realized (more than one order of magnitude) provided that d/L_n can be made less than 0.1 and $s \lesssim 100$ cm/sec. The former requirement is easy to achieve since it can be met with d values of about $10 \mu\text{m}$, well within the current processing state of the art for HgCdTe detectors. The latter requirement may not be so easy to achieve because the state of HgCdTe surface technology is still in the primitive stages. Further investigation into thin-base technology for $3.85\text{-}\mu\text{m}$ and $2.06\text{-}\mu\text{m}$ PV HgCdTe detectors is warranted and may result in significant improvement in the detectivity of such detectors at TE cooler temperatures.

Achieving Faster Response Times

Because these large area PV HgCdTe detectors have response times limited by junction capacitance, the technical approach to increasing response time has been to reduce junction capacitance by means of reducing the base acceptor concentration. Another means is to increase the reverse bias applied to the junction. The detectors made on the present program could not take very high reverse bias. This is thought to be due to surface leakage resistance. If better surface passivation coatings can be devised so that surface leakage is greatly reduced, then much larger reverse bias can be applied with a consequent further reduction in junction capacitance.

The detectors made on the present program were operated at reverse bias of 1 volt or less. With improved surface passivation treatments, it should be possible to operate with 5 to 10 volts of reverse bias. Since junction capacitance varies inversely as the square root of bias voltage, one could hope for a reduction in junction capacitance by a factor on the order of 1/3 to 1/10. This is a significant reduction and could well justify the expense of additional effort in this area.

Engineering Development Program

Following further research and development along the lines previously discussed, it would be appropriate to begin an engineering development phase to increase the producibility and reliability, and decrease the production costs of large area PV HgCdTe detectors. In this section, some specific recommendations for such a program are put forth.

To simplify fabrication of quadrant arrays, the complete array should be constructed on one chip instead of piecing four separate chips together. This not only would save in fabrication costs, it would also allow a closer spacing between individual quadrants. Such an approach would pose no problem for quadrants up to $2 \times 2 \text{ mm}^2$ per element with present day HgCdTe material. Quadrants of $5 \times 5 \text{ mm}^2$ per element would provide a greater challenge. It would be of interest to test present day HgCdTe grown by either the zone melt or solid-state recrystallization method to see if the uniformity and crystal perfection are adequate for this approach to quadrant fabrication.

HgCdTe ingots produced at SBRC are cylindrical in shape with a $\frac{1}{2}$ -inch diameter and a length of 6 to 8 inches. The single-crystal regions in these ingots often extend an inch or so along the ingot axis. If such regions are cut in slab form rather than slices, wafers may be obtained on which 2 or 3 large area quadrant arrays may be fabricated at the same time. This is illustrated in Figure 8-1.

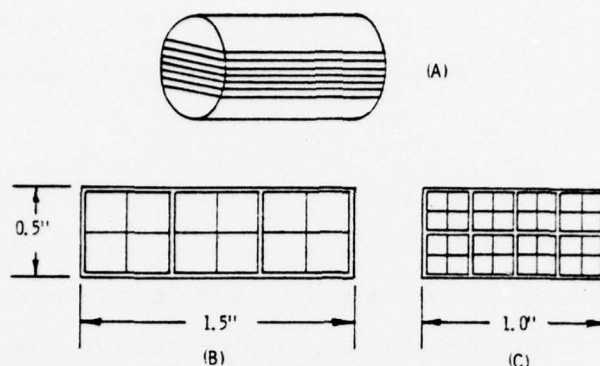


Figure 8-1. (A) Illustration of the Method of Cutting an HgCdTe Ingot into Slabs to Provide Material for Simultaneous Fabrication of; (B) Three $5 \times 5 \text{ mm}^2$ Quadrant Arrays, or (C) Eight $2 \times 2 \text{ mm}^2$ Quadrant Arrays

To obtain even larger wafers, it may be desirable to continue development of the pressure-controlled recrystallization method of crystal growth which has been shown to be capable of producing ingots up to 1 inch in diameter. Although the crystals grown on this program suffered from alloy non-uniformity and off-stoichiometry (i. e., excess Hg or Te in various regions) it is now known that these problems were caused by inadequate mixing of the melt and an improper quench technique. Improved methods for melt stirring and quenching have been devised but have yet to be put into practice.

Another possible method for HgCdTe crystal growth is to employ the epitaxial approach utilizing CdTe as the substrate material. CdTe can be grown into large single crystals on the order of 1 inch or more in diameter. Various methods of HgCdTe epitaxial growth have been demonstrated such as plasma sputtering,^{30, 31} vapor transport,³² and liquid phase epitaxy.^{33, 34}

³⁰ A. Zozime and C. Sella, *Thin Solid Films* 13 373 (1972).

³¹ R. Cornely, "HgCdTe Sputtering Research," Interim Scientific Report for AFOSR by New Jersey Institute of Technology, May 25, 1978.

³² P. Vohl and C. M. Wolfe, *J. Electronic Materials*, 7, 659 (1978).

³³ J. A. Mroczkowski, et al., Honeywell Radiation Center, Final Report - Liquid Phase Epitaxial Development of (Hg, Cd)Te, Contract No. DAAG46-76-C-0030, January 1977.

³⁴ A. H. Lockwood, unpublished results at the Santa Barbara Research Center.

However, further development work would be necessary to perfect a method which would reliably produce the layer quality necessary for large area quadrant array fabrication.

The quadrant array fabrication procedures could remain basically the same as developed on this program. However, some improvements would be desirable. Attachment of the wire leads to the top contacts should be done by standard microbonding techniques rather than by the conducting epoxy. It may also be desirable to add a guard ring or gate control electrode around the periphery of the quadrants to inhibit surface leakage current.

Finally, a suitable assembly incorporating the quadrant array and TE cooler in an evacuated package should be designed and qualified as to reliability and producibility. This is not a major task because similar packages have previously been designed and qualified for other detector types such as PbSe. Thus, the basic design principles have already been established. What needs to be done is to optimize the package design specifically for large-area quadrant detector arrays and to develop parts handling and bake-out procedures which will assure a long vacuum life without degradation of detector performance. The completed detector-cooler assembly should then be subjected to the usual environmental testing procedures to establish its reliability for field service.